Dynamics and optical manipulation of Nuclear spin in self assembled (InGa)As/GaAs quantum dots

Dissertation

Presented to the Faculty of Physics of the

TU Dortmund University, Germany,

In partial fulfillment of the requirements

for the degree of

Doktor rer. nat.

by

Karl Flisinski

technische universität dortmund

Dortmund,

Day of the oral examination: 07.03.2014

Examination board:

Prof. Dr. Dmitri R. Yakovlev

Prof. Dr. Joachim Stolze

Prof. Dr. Heinrich Päs

Dr. Bärbel Siegmann

Contents

1 Motivation

In order to understand the significance and purpose of the field of science that I have been working on I would like to provide you with a short overview over the history of nuclear magnetic resonances and of the development of their optical detection. Afterwards, I will proceed to presenting the importance and need of nanostructures, which is a technology that is included in our everyday life. The last part will give examples where research in the field of quantum mechanics leads to usable devices which are currently marketed.

1.1 A short history of nuclear magnetic resonances and their optical detection

A Nobel Prize is not only the result of a long journey through experimental and theoretical work. It's more like a beginning (of much work) for other scientists. I'm referring to the Nobel Prize in physics in 1902, when Hendrik Antoon Lorentz and Pieter Zeeman were honored "in recognition of the extraordinary service they rendered by their researches into the influence of magnetism upon radiation phenomena" [1]. Pieter Zeeman studied the spectral lines of a gaseous substance under the influence of an external magnetic field [2]. Thereby he found a splitting of one spectral line into three spectral lines under the influence of an external magnetic field. Nowadays this effect is called the "Zeeman effect". Later, Hendrik Lorentz took an interest in these measurements. Consequently, in 1896, he proposed a model of an atom containing charged vibrating particles, bound to a center. Nowadays these vibrating charged particles are called "electron". At that time (1896), however, the idea of an atom consisting of different particles was new. The proposed theory of H. Lorentz could even be used to calculate the charge- to- mass relation (e/m) of the observed particle. But the experimental results showed more than could be explained by this theory. The spectral lines of some elements split up not only three times but even more often. And as more and more elements were studied, the experiments showed that the spectral lines of most elements split up in more than three spectral lines. Therefore, there had to be a fundamental error in the existing theory. It took about thirty years to formulate the new theory, the theory of quantum mechanics, which could explain the Zeeman-effect. So physicists started to work on a new theory. In 1913 Niels Bohr could explain the spectrum of the hydrogen atom with a theory where only a discrete set of energy levels are allowed for the electrons [3]. He introduced the principal quantum number "n" which counts the orbits that an electron is allowed to occupy. His idea that an electron which is bound to a nucleus can only have a discrete energy distribution/ occupy a discrete energy level was a completely new idea. Although the later development of quantum mechanics showed that one quantum number is not enough to describe the inner structure of an atom the quantum theory by Bohr is still regarded as a pioneering work for quantum mechanics. Arnold Sommerfeld introduced two more quantum numbers the azimuthal quantum number "l"

and the magnetic quantum number "m" [4] [5]. Later in 1921 the Stern-Gerlach experiment demonstrated the so called "spin" as an intrinsic property of the electron [6]. Thereby the fourth and last quantum number was found. A set of four quantum numbers is sufficient to describe a system, like bound electrons of an atom, by quantum mechanical equations [7].

Having identified the basics to describe matter on a nanoscale, scientists established new methods in spectroscopy and further developed the theory. The results of these researches in this field of physics were honored by many Nobel Prizes.

In 1939 Isidor I. Rabi discovered the molecular-beam magnetic-resonance detection method [8]. For the first time an oscillating magnetic field was used to study the magnetic properties of atomic nuclei, nowadays this concept is a standard technique. In 1944 his work was honored with the Nobel Prize [9]. In 1952 Felix Bloch and Edward Mills Purcell where honored with the Nobel Prize for the development of the magnetic resonance method for the application on solids and liquids [10]. Following these discoveries, the method of magnetic resonance detection was introduced also in other fields of science like chemistry, where it became one of the most important methods to analyse the structure of chemical compounds [11]. Another example for the wide application of the method of magnetic resonance detection is its use in medicine, where Magnetic Resonance Imaging has become one of the most precise methods to image the human body [12]. Alfred Kastler was honored in 1966 for studying the spatial orientation and manipulation of the nuclear spin. What was striking about his experiments was that Alfred Kastler used optical methods to reach a precision that was orders of magnitude higher than the results that could be obtained without the use of an optical irradiation [13].

A method called "optical pumping" was developed to reach a high precision. Optical pumping is a process in which the angular momentum of polarized light is transferred to spin oriented particles that are split in energy due to a magnetic field. This transfer causes an inversion of population for the Zeeman split states. This means that the spin orientation of the charged particles becomes polarized in space in relation to the orientation of the incoming light and the magnetic field. The manipulation of the nuclear spin system by this process is called dynamic nuclear polarization (DNP) [14]. In Table 1-1 some of the most important achievements that are correlated with optical pumping and NMR are listed.

1968	Dynamic nuclear polarization in semiconductors	G.Lampel, Phys.Rev.Lett. **20**, 491 (1968)
1972	First optically detected NMR in $Ga_{0.7}Al_{0.3}As$ crystals	A.I.Ekimov, V.I.Safarov, Sov. Phys. JETP Lett. **15**, 179 (1972)
1982	Optically detected NMR signal in bulk GaAs	D. Paget Phys. Rev B **25**, 4444 (1982)
1986	"All-optical" NMR experiments in bulk GaAs	V.K. Kalevich, Sov. Phys. Solid State **28**, 1947 (1986)
1990	First optically detected NMR signal in GaAs quantum-well	G. P. Flinn et. al. JOL **45**, 218-220 (1990)
1997	First optically detected NMR signal in single GaAs/AlGaAs quantum dot	D.Gammon et al. Science **277**, 85 (1997)
2010	First optically detected NMR signal in (InGa)As/GaAs quantum-dot ensemble	K. Flisinski et al. Phys. Rev B **82**, 081308 (2010)

Table 1-1 Publications that give a trace about the development of optically detected and/or induced NMR

Nowadays optical pumping is still used to attain the highest sensitivity in NMR measurements, like this thesis and other latest results of research can show [15, 16] .

Having presented a short summary of the history of the discovery of nuclear magnetic resonances and of the development of their optical detection, I would like to proceed now by outlining the importance of nanostructures for the scientific and technological progress.

1.2 The importance of nanostructures

Based on the findings mentioned above the understanding of matter has developed from research on a macroscopic scale down to research on a nano-scale. But not only the knowledge but also the possibility of manipulation of matter on a nanoscale has become an everyday business. The development of the transistor gives a good example of how a process of miniaturization can enhance not only the functionality of devices and lower the cost of production and disposition. It can also enhance the quality of life for the common run of mankind. One just needs to think about a cell phone or a mp3-player. The first idea of a semiconductor transistor was published by Julius Edgar Lilienfeld in 1927 [17]. At that time, however, the industrial production of such a device was not yet possible. In 1948 Walter H. Brattain and John Bardeen published a study on the first working semiconductor transistor that was also the biggest transistor ever built [18]. But the capacities of research and manufacturing developed very fast, so that in 1954 (two years before W. Brattain, J.

Bardeen and William Bradford Shockley were awarded the Nobel prize [19]) every citizen could buy the first transistor radio which consisted of four transistors [20] and in 1955 the Bell Labs announced the first computer based on transistors [21]. As time went by, the transistors became smaller and smaller. Thereby a prediction of Gordon Moore became a law [22]. Since about 40 years the amount of transistors on an integrated circuit has doubled every two years. This development is illustrated by the fact that the processor of a personal computer consists of approximately 592 million transistors [23]. For these purposes the size of a transistor needs to be very small. The size is about 45 nm [24]. However, by the time the process of miniaturization will probably cease. This supposition is based on the fact that the smallest structure of stable matter that is so far known, the atom, was used to build a transistor [25, 26]. Two research groups have shown that a single atom is enough to build a transistor. Therefore, enhancing the capability of computer technology is not "only" done by miniaturization of the used devices. Instead, the development should proceed in many directions: both the further development of already existing technologies and the research of new technologies. In the search of new technologies one particular idea, which I will outline in the following, gave rise to a wholly new branch of research.

Up to now, only one of the characteristics of the electron has been used to transport information: the electric charge. But the electron also owns the spin as an intrinsic property [6]. Moreover, up to now the semiconducting materials used for logical operation were macroscopic, so that the effects of the spin could be ignored. In the range of several tens of nanometers, however, quantum mechanical effects start to dominate the physical conditions of the system [27]. Therefore it is possible to use not only the electric charge but also the spin of the electron for signal processing and logical operations in semiconducting electronic devices [28]. The research field occupied with this idea is called spintronic. The first commercial useful discovery (the giant magnetoresistance) was honored with a Nobel Prize in 2007 [29]. An outlook on the development and practical use of spintronic devices will be given in the following chapter. Now I would like to focus merely on the idea of spintronic and present a puristic way for observation of spin related phenomena. The interest of scientists operating in the field of spintronics is to trace the way of a spin oriented carrier, like the electron, that was induced into the material of interest [30]. The variety of materials is enormous (e.g. semiconducting, ferromagnetic, or paramagnetic materials ...), just like the amount of possible spatial confinements for the spin oriented particles. The puristic idea is to choose a nanostructure that allows the observation of quantum mechanical effects without the influence of the shape of the structure. The simplest geometric object with these attributes is a dot. The dot, as a geometric object, has no elongation in space. It is a zero dimensional object. Such objects cannot be constructed in reality. However, an approximation of a “dot shaped” structure, that can be constructed in reality is the so called "quantum dot” (QD). Quantum dots have no spatial preferences. Therefore it is equally elongated in all spatial dimensions. A typical QD has a diameter of ten to several tens of nanometers. Nanostructures with a dot shape are the primary geometrical objects in which elementary particles, like electrons, occupy discrete energy levels and obey

Hund's rules as the states are filled [31, 32]. This illustrates that although the electrons in nanostructures are not bound to one particular atom, but interact with all given atoms within the nanostructure, they behave just like electrons bound to an atom. While electrons bound to an atom interact with a single nucleus, electrons within a quantum dot interact typically with $\sim 10^6$ nuclei [33]. Under special conditions, as specified in chapter 3.2.2, a quantum dot can be occupied by one electron or one hole. This allows observing and manipulating quantum properties even for single particles. A single spin in a solid confinement can be seen as a realization of a quantum memory and is therefore one of the most promising candidates for the realization of spintronic and quantum information processing devices [34, 35]. However, some limitations for the use of the spin in quantum memory devices have been identified. One limitation is the coherence time of the electron, which has a typical T_2 time of 20 ns [36]. Due to the strong localization of a charge carrier in a quantum dot the interaction of the charge carrier with the nuclei cannot be neglected [37, 36]. One possibility to enhance the coherence time is to manipulate the nuclear spin system by the use of dynamic nuclear polarization (DNP) to assume certain configurations [38, 39, 40].

Important questions that arise in this context are: How long can the polarized nuclei stay polarized? What determines and influences the relaxation time of the depolarization of the previously polarized nuclei? How can the DNP process be manipulated?

Semiconductor materials like gallium arsenide are often used for electronic devices because of the possibility to create nanostructures that are very pure. Moreover a large variety can be obtained by tuning the electron energy by doping these semiconductor nanostructures with different atoms. Because of the discrete energy levels of the electrons and the energy of the bandgap these nanostructures provide means of optical initialization and detection of charge carriers occupying the quantum dot. In addition, polarization optics can be used to induce and detect the spin orientation of polarized charged carriers.

Having explained the idea of spintronics, I would like to proceed now to the presentation of some practical applications of the findings based on the research of spintronics.

1.3 Practical applications in Spintronics

In 1988, Albert Fert and Peter Grünberg independently discovered the Giant Magnetoresistance [41, 42]. This effect can be used to create highly sensitive magnetic field sensors [43, 44]. Since 1997 such sensors are commercially used for common hard drives to reach the highest data capability [45]. Other results in spintronics are also used nowadays in commercial applications, but are of a smaller economic importance than the hard drives mentioned above. The key word for this chapter is Magnetoresistive Random Access Memory (MRAM) [46].

MRAM is a 64 Mbit non-volatile media that uses magnetic polarization rather than electric charge for infinite reading and writing operations. Consequently, it is possible to store data for tens of years without electric power consumption. This device that is working at room temperature promises fast random writing and access speeds with low power consumption. A read out of these magnetic bits is possible by using magnetic tunnel junctions (MTJ) [47]. Superlattice structures of ferromagnetic and non-conducting oxides build a tunneling barrier for the electron. The tunneling which conserves the spin of the electron is only possible, if the spin orientation of the ferromagnetic material and the tunneling electron is the same. Depending on the structures built and materials used the superlattice structures can be used as detection heads for magnetic fields [48] or strain detection [49] with a high sensitivity and spatial resolution in the nanometer range. All these devices deal with highly spin polarized electrons. To build integrated circuits based on spin polarization is theoretically possible [50], but there is a need to control and manipulate the spin current. Integrated circuits based on electric current use transistors to attain this end. For spin current based integrated circuits it is necessary to use spin-transistors. Several research groups have succeeded in building spin-transistors that operate at room temperature by using sandwich structures of ferromagnetic and insulating materials [51] or even traditional semiconductor materials like silicon [52]. A spin transistor is a spin sensitive device that can control and switch electric current. Different research groups hold different opinions on how a spin transistor should be constructed, whether silicon [52] or a sandwich structure of MgO/FeCo should be used for its construction [53] or whether modified MOS-transistors with added magnetic layers out of $\mathrm{Co_2Fe(Al,Si)}$ on the source and drain. Compared to an ordinary MOS-transistor the modified MOS-transistor is even smaller in size (several tens of nanometers) with lower power consumption [54]. Publications about silicon quantum dots working as spin transistors at room temperature show [52] that traditional semiconductor materials are still interesting for spintronic devices.

2 Theoretical Background

2.1 Nuclear interactions

The main aspect of this thesis is the manipulation of the nuclear spin system in quantum dots and the interaction of this manipulated system with the resident electron of a quantum dot. For an analysis and interpretation of the observed effects it is sufficient to determine a Hamiltonian $\widehat{H}$ that contains three parts, namely the Zeeman interaction $\widehat{H}_Z$, the quadrupole interaction $\widehat{H}_Q$, the hyperfine interaction $\widehat{\mathrm{H}}_{\mathrm{HF}}$.

$$\widehat{H} = \widehat{H}_{\mathrm{Z}} + \widehat{H}_{\mathrm{Q}} + \widehat{H}_{\mathrm{HF}} \tag{2.1}$$

Each part represents an interaction that influences the energy levels of the nuclear spin system. The influence of each interaction is discussed in subchapters separately.

2.1.1 Zeeman interaction

The first part $\widehat{H}_Z$ appears for nuclei in a static homogenous external magnetic field B_0. $\widehat{H}_Z$ is due to an interaction of the nuclear spin and the static external magnetic field. Neglecting nuclear-nuclear and other interactions this term is expressed as

$$\widehat{H}_{\mathrm{Z}} = -\gamma_{\mathrm{N}}\, \hbar\, B_0\, \hat{I} \tag{2.2}$$

where γ_N is the gyromagnetic ratio of the proton and $\hbar$ is the Planck constant. This is the ratio of the magnetic dipole moment μ_N to the nuclear spin I, which exist for every nucleus with a non-zero nuclear spin.

$$\mu_{\mathrm{N}} = \gamma_{\mathrm{N}}\, \hbar\, I \tag{2.3}$$

Some values of γ_{N} for different nuclei are exemplarily shown in Table 2-1. According to the usual convention the z-direction is defined in the laboratory frame by the direction of the static homogenous external magnetic field B_0. $\hat{I}$ is the nuclear spin operator, where the three spatial components are denoted $\hat{I}_{\mathrm{X}}$, $\hat{I}_{\mathrm{Y}}$ and $\hat{I}_{\mathrm{Z}}$ and have the cyclic commutation relations

$$[\hat{I}_X, \hat{I}_Y] = \mathrm{i}\, \hat{I}_{\mathrm{Z}} \tag{2.4}$$

Nucleus	Natural Isotopic Abundance[%]	Spin *I*	$\gamma_N/2\pi$ [kHz/G]	Q $[10^{-24}\mathrm{cm}^2]$
^{69}Ga	60.4	3/2	1.022	+0.17
^{71}Ga	39.6	3/2	1.298	+0.10
^{75}As	100	3/2	0.729	+0.31
^{113}In	4.3	9/2	0.931	+0.8
^{115}In	95.7	9/2	0.933	+0.8
^{55}Mn	100	5/2	1.050	+0.33
^{27}Al	100	5/2	1.109	+0.14

Table 2-1 Examples of the gyromagnetic ratio and the quadrupole moment Q with the corresponding nuclear isotopes [55]. Detailed information about the quadrupole moment Q is given in chapter 2.1.2.

Under the influence of B_0 the degenerate nuclear spin states $|m\rangle$ split in different energy levels. This effect is known as the Zeeman-splitting. In respect to the direction of B_0 the nuclear spin states $|m\rangle$ are split in equidistant energy levels, which are given by

$$E_m = -m\,\hbar\,\omega_\mathrm{L} \tag{2.5}$$

$$\omega_\mathrm{L} = -\gamma_\mathrm{N} B_0 \tag{2.6}$$

Here ω_L is the Larmor frequency of a nucleus with the spin quantum number I. The operator $\hat{I}_\mathrm{Z}$ has 2*I*+1 eigenstates $|\mathrm{m}\rangle$ (resulting in 2*I*+1 energy levels separated in energy by E_m). As a convention the lower energy states correspond to higher (positive) m values [56]. The expectation values of the components perpendicular to the z-axis ($\hat{I}_\mathrm{X}$, $\hat{I}_\mathrm{Y}$) show an oscillating behavior in time with a frequency given by eq. (2.5). As shown in Table 2-1 every nucleus can be assigned its own gyromagnetic ratio γ_N . Therefore it is possible to identify the nuclei by knowing their Larmor frequency.

In contrast to the values of $\hat{I}_\mathrm{X}$ and $\hat{I}_\mathrm{Y}$ the expectation values for $\hat{I}_\mathrm{Z}$ are stationary. The classical interpretation is a precession of a magnetic dipole around the z-axis. In a static homogenous external magnetic field the population of the energy levels for an ensemble of identical nuclei is given by the Boltzmann distribution after reaching the thermal equilibrium.

For a two level system which is given by a nuclear spin *I*=1/2, for the population $N_{-1/2}$ and $N_{+1/2}$ of the eigenstates $m_I = -1/2$ and $m_I = +1/2$ results

$$\frac{N_{-1/2}}{N_{+1/2}} = \mathrm{e}^{-\hbar\omega_\mathrm{L}/k_\mathrm{B}T} \tag{2.7}$$

where T is the absolute temperature of the ensemble and k_B is the Boltzmann constant [57]. For $^1\mathrm{H}$ nuclei (protons) in a magnetic field of 5T $\hbar\omega_\mathrm{L} \approx 10^{-6}$ eV. At room temperature $k_\mathrm{B}T \approx 2.5 \cdot 10^{-2}$ eV. Equation (2.7) shows a difference in population in this case of about one part in 10^5. This example shows the intrinsically low sensitivity which is a well-known problem for experiments involving magnetic properties of nuclear populations (such as in common NMR). There are two possibilities to enhance the differences in population. The first possibility involves the increase of B_0 which in turn increases linearly the distance in energy of the Zeeman-levels. As shown in eq. (2.7), a larger $\hbar\omega_\mathrm{L}$ causes a larger difference in population. The second possibility to enhance the differences in population is to increase the quantity of the nuclei that are under the influence of B_0. Even such a small difference in population is sufficient to create a nuclear magnetization parallel to B_0. The thermal equilibrium magnetization for an ensemble of nuclei with *I*=1/2 is given by

$$M_0 = \frac{n_0\, \gamma_\mathrm{N}^2\, \hbar^2 B_0}{4k_\mathrm{B}T} \tag{2.8}$$

n_0 is the number of nuclei per unit volume.

2.1.2 Quadrupole interaction

For nuclei with spin *I* > 1/2 asymmetric charge distribution leads to a quadrupole moment Q. Nuclei with a quadrupole moment become sensitive to an electric field gradient (EFG).

Up to now the electric charge of the nuclei, which leads to an interaction with electric fields, has been neglected. The interaction energy *W* of the nucleus in this electrostatic potential $\phi(\boldsymbol{r})$ is given by the integral over the volume.

$$W = \int \rho_\mathrm{N}(\boldsymbol{r})\phi(\boldsymbol{r})d^3\boldsymbol{r} \tag{2.9}$$

$\rho_\mathrm{N}(r)$ is the nuclear charge density distribution. Expanding $\phi(\boldsymbol{r})$ at the center position of the nuclear charge distribution in a Taylor series gives

$$\phi(r) = \phi(0) + \boldsymbol{r}\cdot\nabla\phi(0) + \frac{1}{2}\sum_i x_i\ x_j \left(\frac{\partial^2\phi}{\partial x_i \partial x_j}\right) + \cdots \tag{2.10}$$

The sources of the electric field lie outside the nucleus. Therefore $\nabla \mathrm{E} = 0$ in the region of the nucleus. According to the Taylor series the interaction energy can be expressed as

$$W = q\phi(0) - p \cdot E(0) - \frac{1}{6}\sum_{ij} Q_{ij}\left(\frac{\partial E_j}{\partial x_i}\right)_0 + \cdots \qquad (2.11)$$

q is the total charge of the nucleus, p is the nuclear electric dipole (EDM) moment and Q_{ij} is the nuclear electric quadrupole moment tensor. The first term gives the total electric charge of the nucleus. It describes the electrostatic interaction of a point shape nucleus and the electric potential $\phi(\boldsymbol{r})$. For a point charge this would be the only term. The quantum mechanical expression of the EDM is

$$p = \sum_{k=1}^{Z} \int e(\boldsymbol{k})\boldsymbol{r_k}\,|\psi(\boldsymbol{r_1} \ldots \boldsymbol{r_A})|^2\, d^3\boldsymbol{r_1} \ldots d^3\boldsymbol{r_A} \qquad (2.12)$$

ψ is the normalized wave function of a stationary state of the nucleus with the atomic number Z and mass number A. The nuclear charge is carried by protons each having a charge e.

$$\rho_{\mathrm{N}}(\boldsymbol{r}) = \sum_{k=1}^{Z} e\,\delta(\boldsymbol{r} - \boldsymbol{r_k}) \qquad (2.13)$$

$\rho_{\mathrm{N}}(\boldsymbol{r})$ is, denoting the co-ordinates of the protons by $\boldsymbol{r}_k$, the charge density of the protons. Since the parity of a stationary state is defined by +1 or -1 it can be shown that the transformation $\boldsymbol{r}_k \rightarrow -\boldsymbol{r}_k$ gives p = -p or p equal to zero. So the first non zero term in the multipole expansion is the third term of the expansion corresponding to the electric quadrupole moment Q. With the quantum mechanical expression [58]

$$Q_{ij} = \sum_{k=1}^{Z} \int e(\boldsymbol{k})\left(3x_i x_j - r^2\delta_{ij}\right)_k |\psi(\boldsymbol{r}_1 \ldots \boldsymbol{r}_A)|^2 d^3\boldsymbol{r}_1 \ldots d^3\boldsymbol{r}_A \qquad (2.14)$$

The quadrupole moment tensor Q_{ij} is symmetric ($Q_{ij} = Q_{ji}$) and the trace of Q_{ij} is zero ($Q_{xx} + Q_{yy} + Q_{zz} = 0$). All the elements of Q_{ij} (i,j = 1,2,3) can be expressed in terms of the element Q_{zz}. This value is called the nuclear electric quadrupole moment and is denoted by *Q*. Moreover it can be shown that *Q* can be expressed in terms of the spin vector ***I*** of the nuclear state as

$$Q = C\frac{2}{3}I[2I - 1] \qquad (2.15)$$

It is important to note that *Q* is only non-zero for nuclear spins $I \geq 1$, as shown in eq. (2.15). Eq. (2.11) shows that the quadrupole interaction term vanishes without a quadrupole moment of the nucleus. This means that nuclear transitions of *I*=+1/2> to *I*=-1/2> are not affected in first order. In solids with cubic symmetry, like GaAs, the quadrupole interaction also vanishes. In this case, however, the vanishing of the quadrupole interaction takes place due to the vanishing of the electric field gradient tensor q_{ij}.

$$H_Q = -\frac{1}{6}\sum_{ij} Q_{ij}\left(\frac{\partial E_j}{\partial x_i}\right)_0 \tag{2.16}$$

$$= -\frac{1}{6}\sum_{ij} Q_{ij}\left(\frac{\partial^2 \phi}{\partial x_i \partial x_j}\right)_0$$

$$= -\frac{1}{6}\sum_{ij} Q_{ij} q_{ij}$$

In general the electric field gradient is a 3x3 tensor which has a diagonal form in a properly chosen co-ordinate system. These three diagonal components (q_{xx}, q_{yy}, q_{zz}) must obey Laplace's equation, so that the sum of these components becomes zero

$$\frac{\partial^2 \phi}{\partial x^2} + \frac{\partial^2 \phi}{\partial y^2} + \frac{\partial^2 \phi}{\partial z^2} = 0 \tag{2.17}$$

In the special case of a crystal with a cubic unit cell symmetry all off-diagonal elements of $\mathrm{q_{ij}}$ are zero and the three diagonal elements are equal. With regard to eq.(2.17) no quadrupolar interaction can occur in a cubic crystal. Nonetheless, due to strain in nanostructures, like quantum dots, the cubic symmetry of the unit cell is broken. The consequence of a broken symmetry is a change of the EFG. The EFG tensor is now dominated by the direction and intensity of the strain in the lattice structure. According to the Voigt notation the EFG tensor is defined by [59]

$$V_j = \sum_k S_{jk}\epsilon_k, \quad j,k = 1 \ldots 6, \tag{2.18}$$

$$1 = \mathrm{xx}, \quad 2 = \mathrm{yy}, \quad 3 = \mathrm{zz}$$

$$4 = \mathrm{yz}, \quad 5 = \mathrm{zx}, \quad 6 = \mathrm{xy}$$

The S_{ij} tensor can be extracted from nuclear acoustic resonances [60]. It relates the EFG tensor q_{ij} to the strain tensor ϵ of the lattice. Shulman et al. have shown that the *S* tensor only has two independent elements, S_{11} and S_{44} [61]. In the special case of GaAs quantum dots it is possible to use a cylindrically symmetric QD model and the transversal isotropic approximation in the continuum elasticity theory. With these approximations the strain within a quantum dot is oriented only in the growing direction (z-axis) of the quantum dot, so that the EFG tensor can be written as

$$q_{zz} = S_{11}\epsilon_{zz} \tag{2.19}$$

Nuclei with spin *I*=1 or higher can have a non-zero quadrupole moment. The classical picture is that the charge distribution of nuclei with a spin *I*>=1 is no longer spherical, like in nuclei with spin *I*=1/2. With spin *I*>=1 the charge distribution becomes spheroid like (cigar-shape). The elongation of the charge distribution leads to an electric quadrupole moment *Q* which interacts with an electric field gradient (EFG). The energy of the electric quadrupole interactions depends on the orientation of the quadrupole moment relative to the EFG. A charge distribution whose symmetry axis is parallel to the direction of the EFG will give a positive Q_{ij} (prolate shape), while a charge distribution whose symmetry axis is perpendicular to the direction of the EFG (oblate shape) will give rise to a negative Q_{ij}. The influence of the quadrupole interactions on the Zeeman splitting leads to a splitting of the nuclear spin-states that is no longer equidistant in energy, like shown in

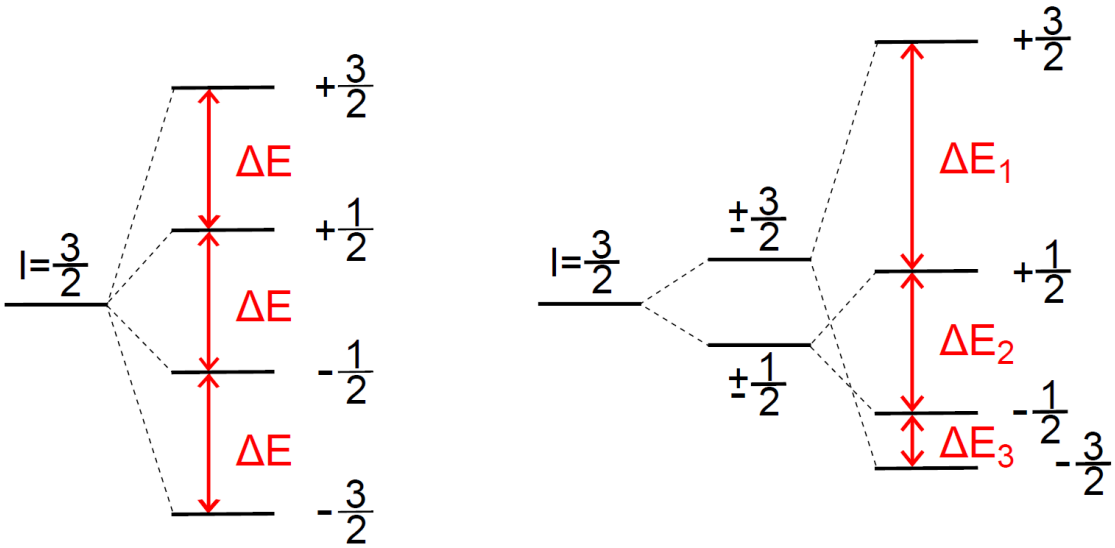

Figure 2-1 (left) Zeeman splitting without quadrupole interaction for nuclei with spin $\boldsymbol{I} = \frac{3}{2}$. Red arrows indicate the possible transitions which are equidistant in energy. (right) Zeeman splitting with quadrupole interaction for nuclei with spin $\boldsymbol{I} = \frac{3}{2}$. Each transition indicated with a red arrow got its own distance in energy ($\Delta \boldsymbol{E_1} \neq \Delta \boldsymbol{E_2} \neq \Delta \boldsymbol{E_3}$).

2.1.3 Hyperfine interaction

The third term $\widehat{H}_{HF}$ of eq.(2.1) is derived from the mutual interaction of the nuclear spin *I* and the electron spin *S*. The general form of this Hamiltonian is

$$\widehat{H}_{\mathrm{HF}} = A_{\mathrm{HF}}\hat{I}\cdot\hat{S} \tag{2.20}$$

A_{HF} has two contributions $A_{\mathrm{HF}} = A_{\mathrm{S}} + A_{\mathrm{P}}$. Electrons with a S-type wave function contribute to A_S and electrons with P-type wave function contribute to A_{P}. Although the influence of the P-type electrons is very weak, some research groups have shown that it may not be neglected completely [62]. Other research groups have even shown that holes with a P-type wave function interact with nuclei via the hyperfine interaction [63]. Because of the overlap of their S-type wave function and the nuclear spin, in this thesis only contributions of S-type electrons are taken into account. Due to this overlap the influence of S-type electrons on the nuclei is much larger than the influence of electrons with a P-type wave function. A_S can be calculated as

$$A_{\mathrm{S}} = K_{\mathrm{S}}(\gamma_{\mathrm{e}}\hbar)(\gamma_{\mathrm{N}}\hbar)|\psi(0)|^2 \tag{2.21}$$

γ_e is the gyromagnetic ratio of the electron, K_{S} is a proportionality coefficient, $|\psi(0)|^2$ is the probability of presence of an electron which is located at the position of a nucleus. For some applications later in the text it is more suitable to use ladder operators

$$\widehat{H}_{\mathrm{HF}} = A_{\mathrm{HF}}\left[\frac{1}{2}\left(\hat{I}_+\cdot\hat{S}_- + \hat{I}_-\cdot\hat{S}_+\right) + \hat{I}_Z\cdot\hat{S}_Z\right] \tag{2.22}$$

The typical timescale of the hyperfine interaction is 10^{-11}s [64] and the two major effects of the hyperfine interaction are (i) inelastic relaxation of the electron spin via the so called "flip-flop" process (ii) the Overhauser shift of the electron spin resonance frequency [65]. The mathematical formulation of these two effects can be seen in eq.(2.22). The first part of the mathematical formulation including the ladder operators ($\hat{I}_+ = \hat{I}_{\mathrm{x}}+\mathrm{i}\hat{I}_{\mathrm{y}}$ and $\hat{I}_- = \hat{I}_{\mathrm{x}}-\mathrm{i}\hat{I}_{\mathrm{y}}$) describes a dynamic process of adding or subtracting an angular momentum of the electron to the nuclear spin system. The total angular momentum is conserved in this process. This process leads to the so called "dynamic nuclear polarization" (the DNP is also known as the Overhauser effect [66]). The initialization of an angular momentum to the electron can be achieved optically by excitation with circularly polarized light. The second part of the mathematical formulation $\hat{I}_{\mathrm{Z}}\cdot\hat{S}_{\mathrm{Z}}$ is called the Zeeman interaction between nuclear and electron spin, because polarized nuclei act on the electron as an effective magnetic field, which is called the Overhauser field [67, 68, 69]. A spin polarized electron also acts on the nuclei as an effective magnetic field, which is called the Knight field [66]. The Overhauser field can be expressed by

$$B_{\mathrm{N}} = \frac{A_{HF}\langle I \rangle}{g^{*}\mu_{\mathrm{B}}} \qquad (2.23)$$

where $\langle I \rangle$ is the average nuclear spin and g^{*} is the effective g-factor of conduction electrons. In case of an Overhauser field that consists of different species of nuclei, the total Overhauser field is a sum over all species. In a single self-assembled InGaAs/GaAs QD it can reach about 3T [71].

The Knight field B_e can be expressed by

$$B_{\mathrm{e}} = K_{\mathrm{S}}\, g_{\mathrm{e}}\mu_{\mathrm{B}} \sum_{j} S_j \left|\psi(\boldsymbol{r}_j)\right|^2 \qquad (2.24)$$

where $\sum_j$ is the sum over all contributing electrons. S_j is the electron spin of each electron j and $\left|\psi(\boldsymbol{r}_j)\right|^2$ is the probability of the presence of each electron j at the location $\boldsymbol{r}$. The closer a spin polarized electron is located to a nucleus, the stronger the interaction of the Knight field on this nucleus will be. Conduction band electrons have a S-type wave function. In the center of a quantum dot their probability of presence is the highest. For nuclei at the center of a quantum dot this interaction suffices to suppress the dipole-dipole interaction of neighboring nuclei, which is the main source for nuclear depolarization. Under the influence of the Knight field a nuclear polarization is possible even without an external magnetic field [66]. Furthermore the Knight field gives a contribution to the total magnetic field, which leads to a Knight shift of the resonances for nuclei in NMR measurements [72, 73].

2.1.4 Interaction with nuclear fluctuation field

As mentioned above, the polarized nuclei can be summarized to an effective nuclear field known as the Overhauser field. In experiments a nuclear polarization of 100% was not observed up to now.

But polarizations close to 100% could be achieved, which is sufficient to observe a weakening of effects that depolarize the Overhauser field (even in the absence of a continuous electron spin polarization in the quantum dot) [74]. The spin direction of the unpolarized nuclei changes randomly. For timescales much longer than the nuclear spin correlation time, which is in the order of 10^{-4} s, the unpolarized nuclei give no contribution to the Overhauser field. At such time scales the sum of the spin vectors can be averaged to zero. But the electron spin lifetime is orders of magnitude smaller than the nuclear spin correlation time. At time scales of the electron spin lifetime the sum of unpolarized nuclear spin vectors is non zero and pointing in a constant direction. The result is an interaction of the electron and an effective magnetic field which is called the frozen fluctuation field δB_{N} [37]. Several theoretical studies show that the dominant mechanism of electron spin

polarization decay in quantum dots at low temperatures is due to the interaction with the frozen fluctuation field δB_{N} if external magnetic fields do not exceed δB_{N} [75]. It is possible to estimate the magnitude of δB_{N} for a quantum dot made of N identical nuclear spins *I*. The average amplitude of the nuclear fluctuation field is given by

$$\delta B_{\mathrm{N}} = \frac{1}{g_{\mathrm{e}}\mu_{\mathrm{B}}}\frac{2}{\sqrt{N}}\sqrt{I(I+1)} \tag{2.25}$$

The maximum Overhauser field is reached when all nuclear spins are polarized

$$B_{\mathrm{N}}^{\max} = \frac{1}{g_{\mathrm{e}}\mu_{\mathrm{B}}}2AI \tag{2.26}$$

For InAs and GaAs quantum dots the maximum Overhauser field is in the range of several Tesla. As a result $\delta B_{\mathrm{N}} \sim B_{\mathrm{N}}^{\max}/\sqrt{N}$, which corresponds to an effective field of typically several tens of mT [76]. The radiative lifetime of charge carriers in quantum dots is orders of magnitude shorter than the time that is needed to change the direction of δB_{N} ($\sim$100 µs) [77]. During this time charge carriers can coherently precess around δB_{N}. Due to fast precession only the projection of electron spin onto the field is conserved. The magnitude and the direction of the fluctuating field are randomly distributed in the QD ensemble. Therefore, in the absence of other fields, such as the external magnetic field and the field of nuclear polarization, the depolarization of the electron spin by the fluctuating field reduces the observable *z* component of spin polarization to 1/3 of its initial value [37, 78]. In a quantum dot ensemble the amplitude and the direction of δB_{N} in every quantum dot are different. Therefore the total magnetic field is different for every quantum dot. The total magnetic field for the residual electron is a sum of the frozen fluctuating field, the Overhauser field and the external magnetic field. The result is a decay of the average electron spin $\langle \boldsymbol{S}(t) \rangle$ in a quantum dot ensemble. In measurements acquired under experimental conditions the signal is typically collected over several seconds. The consequence is an integration over many different constellations of the frozen fluctuation field which gives a coherence time T_2^* of the order of 3 ns. The effect of averaging can be eliminated by using spin-echo techniques. Under such experimental conditions coherence times of the order of 1 µs at $B_0 = 100$ mT can be found [79]. Theory and experiments can show that the hyperfine interaction with δB_{N} is the main source for electron decoherence in quantum dot structures [76].

2.1.5 Spin temperature

As mentioned above, in the presence of a constant external magnetic field $\boldsymbol{B}_0$ the nuclear spin states are no longer degenerate. In order to describe the nuclear spin system under the influence of $\boldsymbol{B}_0$ as a thermodynamic system with a certain temperature, the nuclei need to interact with each other so that a thermal equilibrium is achieved. The model of a spin temperature is valid for isolated systems where the number of particles and energy is

conserved [80, 81]. The interaction that can establish a thermal equilibrium in the nuclear spin system is the dipole-dipole interaction [82]. It is given by

$$\widehat{H}_{\mathrm{DD}} = \frac{\mu_B^2}{2} \sum_{n \neq n} \frac{g_n g_{n'}}{\boldsymbol{r}_{nn'}} \left((I_n I_{n'}) - 3 \frac{(I_n \boldsymbol{r}_{nn'})(I_{n'} \boldsymbol{r}_{nn'})}{\boldsymbol{r}_{nn'}^2} \right) \qquad (2.27)$$

where $\boldsymbol{r}_{nn'}$is the translation vector between the nuclei n and n'. The influence of this interaction on the nuclear spin system can be separated in two parts [83]. One part of the interaction is spin conserving and leads to a spin diffusion that tends to make the nuclear polarization uniform in space. The total energy of the nuclear spin system does not change by the dipole-dipole interaction, but differences in population of the Zeeman levels are reduced. Problems with the application of this model appear in systems where the Zeeman levels are not equidistant since then the energy absorbed by one nucleus in a transition between the Zeeman levels is different from that released by the other. If the differences of the Zeeman levels are not too large, the energy conservation can be still fulfilled by the Heisenberg uncertainty principle. But the probability of transitions decreases with an increasing of the energy mismatch. The other part of the interaction is spin non-conserving and leads to a depolarization of nuclear spins in magnetic fields $\boldsymbol{B}_0 \leq \boldsymbol{B}_{\mathrm{L}}$, where $\boldsymbol{B}_{\mathrm{L}}$ is the "local field" which is created in the position of a nucleus by the neighbouring nuclei. For bulk GaAs, $\boldsymbol{B}_{\mathrm{L}}$ is on the order of 0.1 mT [84] and leads to a precession period of a nuclear spin on the order of 10^{-4} s. This is an intrinsic time scale for the nuclear spin system in which a thermal equilibrium is established. For a system with non-equilibrium nuclear spin polarization that is not influenced by any other interactions, this time is needed to depolarize all components of the nuclear spin system. It is called the T_2 dipole-dipole relaxation time. For $\boldsymbol{B}_0 \geq \boldsymbol{B}_{\mathrm{L}}$ the time T_2 is the transverse relaxation time, because it determines the decoherence of the spin component perpendicular to B_0 [77]. It was experimentally shown that in self-assembled quantum dots the strain induced nuclear quadrupole interaction can increase the T_2 time [85]. The nuclear spin temperature is conserved during the spin-lattice relaxation time T_1. This time denotes the isolation of the nuclear spin system to the crystal lattice. The relation between T_1 and T_2 is important for the legitimation to describe the nuclear spin system as a thermodynamic system. Therefore T_1 needs to be larger than T_2. In this case the nuclear spin system can achieve thermal equilibrium and be described by one spin temperature so that the relaxation process to the lattice can be treated as a small perturbation of the system. In theory is $T_1 \geq T_2$ [86, 87]. Experiments could prove that in bulk GaAs T_1 is on the order of minutes [88, 89]. In bulk silicon T_1 is even on the order of days [90]. The situation changes for nuclei in n-doped quantum dots (or at a donor center). In this situation the quantum dot is permanently occupied by an electron and the coupling to the lattice is effectively mediated by the electron spin. The T_1 time is much shorter in this case and becomes comparable with the T_2 time [91, 40]. However, if a changing of the nuclear spin temperature occurs, it has an influence on the population of the Zeeman levels. Thereby the magnetic quantum number I of a nucleus relative to B_0 is increased, while the magnetic quantum number of another

nucleus is decreased. No additional energy needs to be added, as it is also in the case of collisions between molecules in an ideal gas. In other words, the dipole-dipole interaction is responsible for nuclear spin diffusion. The population of the Zeeman levels is given by the Boltzmann distribution for each spin temperature.

2.2 Negative circular polarization

As mentioned in the previous section, all quantum dot samples used in this thesis are n-doped. The quantum dots of the sample used have a diameter of about 10 – 30 nm and a height of several nm. Since in an InAs-GaAs system the exciton Bohr radius is 10 – 20 nm, the size of the quantum dots is small enough for the three- dimensional quantum confinement effect [92]. Under a three-dimensional quantum confinement the allowed energy levels become discrete values for particles occupying the quantum dot. Electrons trapped in a quantum dot create shell structures that are occupied in accordance to the generalized Hund's rules, similar to electrons bound to an atom [93, 94, 95, 96]. Therefore nanostructures like quantum dots are also called "artificial atoms" [97, 98]. The band structure of a certain material is given by the periodic repetition of the unit cell. In bulk material the assumption of an infinite repetition, resulting in symmetry operations, gives a correct description of the band structure. Quantum dots have a small spatial extent and consist of a finite and countable repetition of the unit cell, which leads to a reduction of symmetry operations. As a result, the band structure of the bulk material differs from the band structure of the quantum dot. Many research groups investigate theoretically and experimentally the electronic structure and spin effects of electrons in quantum dots. A powerful tool for theoretical studies is the density functional theory (DFT) and the (extended) Hartree-fock theory [99, 100]. Experimentalists often use spectroscopic methods like the far- infrared spectroscopy. For pyramidal self-assembled InAs-GaAs quantum dot structures a model is constructed to calculate exchange and correlation terms of the many-body Hamiltonian by the use of the local spin density approximation (LSDA) [101]. In comparison with the results achieved experimentally using far-infrared spectroscopy, this theoretical model shows good agreement [102]. Besides, a Monte Carlo simulation quantifying the error introduced by LSDA justifies the use of LSDA calculations to test models of self-assembled dots against current experimental measurements [103]. Experimental and theoretical investigations have shown that the shape and deformation of quantum dots have a dramatic influence on the energy levels of holes and electrons [104, 105]. A more detailed analysis of self-assembled In(Ga)As/(Al,Ga)As quantum dots shows a correlation of the quantum dot symmetries and the possibility of an exciton state mixing. Quantum dots with a high symmetry belong to the $\mathrm{D}_{2\mathrm{d}}$ group with an in-plane rotational symmetry. This symmetry can be broken down to $\mathrm{C}_{2,\mathrm{v}}$ or C_2 by an uniaxial deformation, for example induced by strain. In the simple case of the $\mathrm{D}_{2\mathrm{d}}$ symmetry excitons with total spin $|\boldsymbol{M}_{\sum}|$ =1 and

$|\boldsymbol{M}_{\sum}|$=2 do not mix with each other. In the case of a fully broken symmetry it is no longer meaningful to distinguish between excitons with $|\boldsymbol{M}_{\sum}|$ =1 and $|\boldsymbol{M}_{\sum}|$=2 due to the strong mixing of the eigenstates. A more detailed analysis is provided in [106]. This thesis handles nuclear spin phenomena where effects of exciton state mixing are not considered. The following description of optical selection rules is given for quantum dots with a rotational symmetry $\mathrm{D}_{2\mathrm{d}}$ and is sufficient for the studied quantum dots in this thesis.

In n-doped quantum dots the absorption of a photon leads to the creation of a trion state consisting of two electrons in the conduction band and a hole in the valence band, also called a negatively charged trion T^{-}. In this case three charged particles can interact with each other. The two electrons of the trion interact by the spin-spin interaction, which leads to a fine-structure of the trion. Besides there is the electron-hole interaction [107, 108, 109, 110]. In analogy to an exciton there are also different constellations of a trion. The constellations of the trion are characterized by the population of different energy levels of a quantum dot with different spin orientations. When both electrons of the trion occupy the ground-state of the conduction band and the hole occupies the ground-state of the valence band, it is called a "cold" trion. Due to the Pauli exclusion principle, the spin orientations of the electrons are opposite to each other, so that the total spin is zero. Therefore electron-hole spin interactions can be neglected. The emission of a "cold" trion constellation, due to an electron-hole recombination, is called the ground-state emission. The resident electron, resulting from the delta-doping, always occupies the ground-state of the conduction band. However, the photoexcited electron can also occupy the first excited state of the conduction band. The exchange interaction between these electrons leads to an energy splitting of the trion states. In comparison the electron-hole exchange interaction is one order of magnitude smaller [108]. In this constellation, the energy of the trion is larger than in the "cold" trion constellation. Therefore it is called an excited trion or a "hot" trion. An overview of the different “hot” trion constellations and the corresponding energies are given in Figure 2-3 and Figure 2-2.

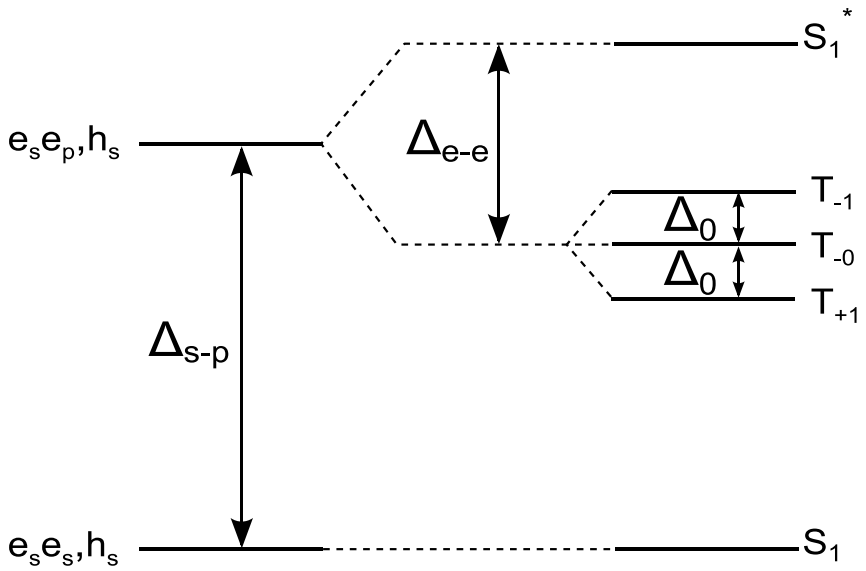

Figure 2-2 Energy levels of the "hot" trion with a hole spin $\boldsymbol{J_{hole} = +3/2}$. The energy difference Δ_{s-p} of the ground-state $\boldsymbol{S_1}$ and the excited state $\boldsymbol{S_1^*}$ is typically several tens of meV. The electron-electron exchange interaction splits the excited state of the trion into a single state $\boldsymbol{S_1^*}$ with total spin $\boldsymbol{M_\Sigma = 0}$ and a triplet state, which is shown in Figure 2-3. The energy splitting Δ_{e-e} is typically several meV. The electron-hole interaction $\Delta_{\mathbf{0}}$ is typically several hundred μeV.

Additionally, one can also control the spin orientation of the photoexcited electron by the use of circularly polarized light. Depending on the total spin M_Σ of the recombining electron-hole pair a "dark" or "bright" trion can be formed. The total spin is conserved during a recombination. It can have the value of $M_\Sigma = |1|$ or $M_\Sigma = |2|$. Photons, however, can only have a spin angular momentum of $\mp\hbar$. As a consequence only the recombination with a total spin of $M_\Sigma = |1|$ is radiative and releases a circularly polarized photon. The recombination with a $M_\Sigma = |2|$ is non-radiative, because as a boson it is only possible to have an angular momentum of $\mp\hbar$. Examples of "dark" and "bright" trions are given in Figure 2-3.

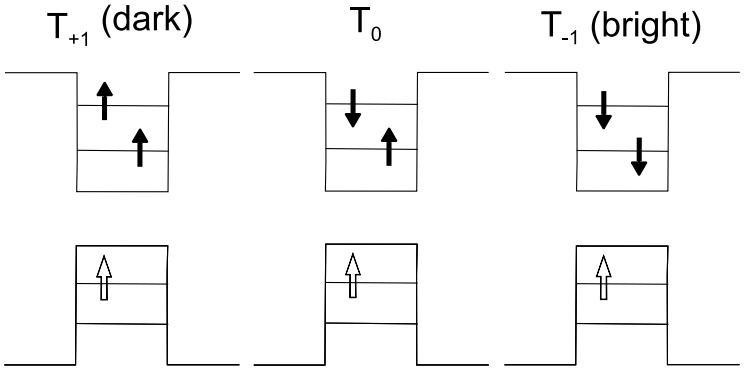

Figure 2-3 A hole spin $\boldsymbol{J_{hole} = +3/2}$ enables three constellations of the "hot trion". Depending on the total spin $\boldsymbol{M_\Sigma}$ of the "hot trion" a bright and a dark recombination is possible.

The radiative decay time of the trion state is up to 1 ns, which is comparable to that of an exciton. During this time, an optical spin manipulation [111] and an optical spin readout are possible [112, 113]. In an undoped quantum dot the possibilities of coherent electron spin manipulation are limited by the radiative lifetime of the exciton. In n-doped quantum dots the resident electrons show a possibility of coherent spin manipulation for ∼10 ns. In this case, the limiting factor is given by the hyperfine interaction of the electron with the nuclear spin fluctuation. This time is surprisingly short, because the nuclear spin fluctuation field changes on a timescale of several hundreds of nanoseconds [114, 115].

2.2.1 Effect of negative circular polarization (NCP)

The effect of negative circular polarization (NCP) is observed after excitation of a sample with circularly polarized light of one helicity, if the resulting photoluminescence that can be detected has a stronger intensity of the opposite helicity. In other words, if the sample is excited with σ^+ polarized light, then the photoluminescence of the sample has σ^- polarization light. Different models have been realized to describe the NCP-effect. Admittedly, there are differences between the models describing the NCP-effect. However, the existing models consent with regard to two aspects.

The first common aspect describes the fact that the NCP-effect has only been observed on n-doped nanostructures [109, 110, 116]. Nowadays, the observation of this effect is seen as a proof that the sample is n-doped with one electron per nanostructure. For highly n-doped nanostructures a disappearance of the NCP-effect was observed [117]. The second aspect describes the appearance of a spin flip that is followed by an electron relaxation to the ground-state of the valence band.

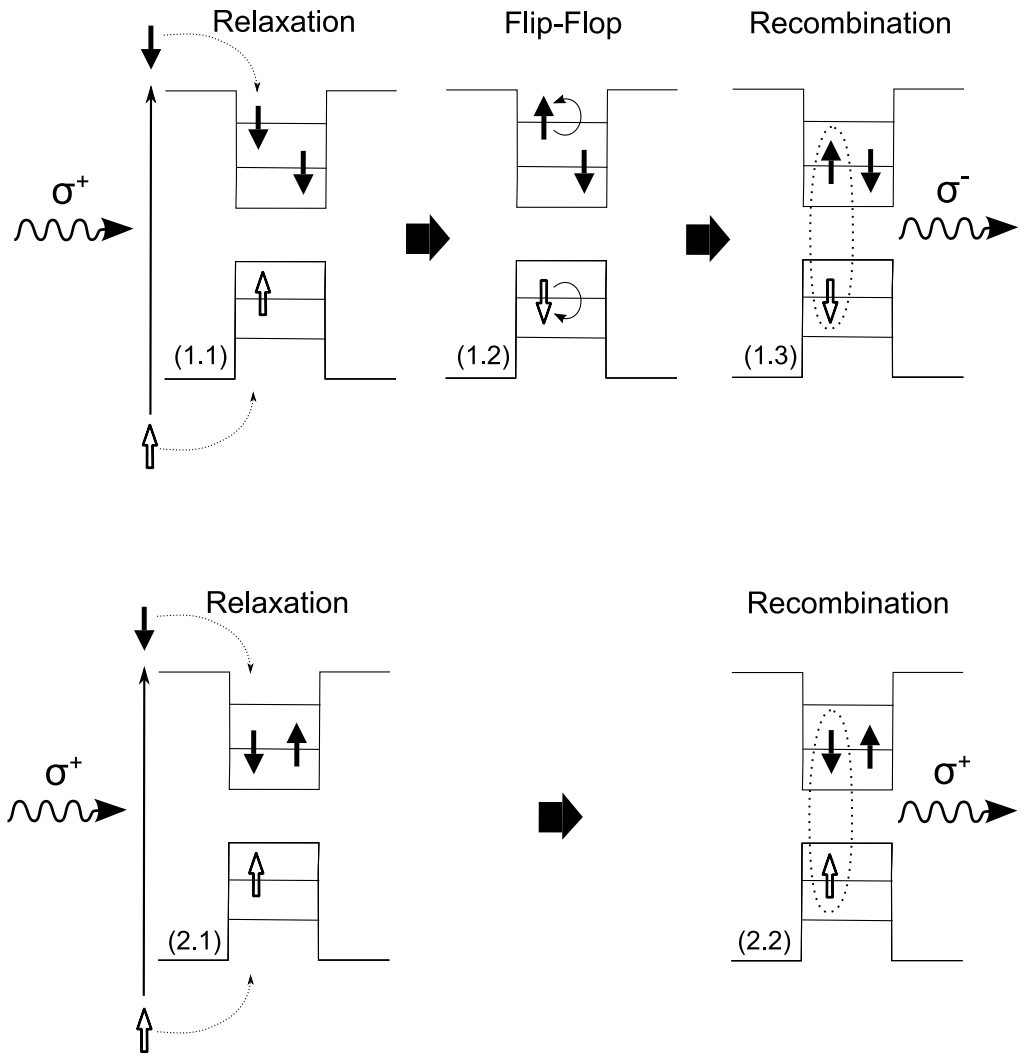

Figure 2-4 Step 1.1 shows the relaxation of an electron-hole pair that was excited into the wetting layer. The relaxation of the photoexcited electron to the ground-state of the conduction band is not possible due to the same spin orientation of the resident electron and the photoexcited electron (constellation of a "hot trion"). In step 1.2 a spin flip process is shown, which allows the photoexcited electron to relax into the ground-state. The recombination of the "cold trion" in step 1.3 leads to a negative circular polarization. Step 2.1 shows a relaxation of the photoexcited electron-hole pair to the ground-state of the quantum dot, which leads to a formation of a "cold trion". The recombination in step 2.2 leads to a positive circular polarization.

In the following chapters three models of the NCP-effect for n-doped quantum dots will be outlined to show the different basic approaches.

Model A

This model mainly fits for resonant excitation to the ground-state of the conduction band of the quantum dot, besides for structures having a shallow potential well like quantum wells with slight fluctuations of thickness [118]. At points of thickness fluctuations the potential slightly differs from the surrounding material [64]. It only considers the resonant excitation of an electron to the ground-state of the conduction band. Due to the resident electron in

the ground-state only electrons with an opposite spin direction can be excited by a photon. One of the three possible recombinations comprises a spin flip which is followed by the NCP-effect, as it is shown in Figure 2-5. All possible recombinations occur with the same probability.

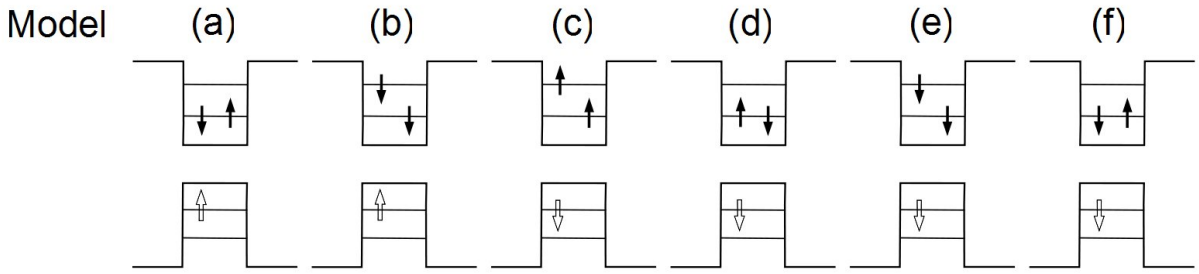

Model	(a)	(b)	(c)	(d)	(e)	(f)
A	1/3	0	0	1/3	0	1/3(-)
B	1/4	1/4(-)	0	0	1/4	1/4
C	$(1-q)n_A$	$n_P(-)$	0	0	0	qn_A

Figure 2-5 Constellations of a trion in an n-doped quantum dot. Constellation (a)-(d) gives a bright recombination, in contrast (e) and (f) lead to a dark recombination. The probability of each constellation is listed for every model separately. A minus sign (-) indicates a negative circular recombination.

Self-assembled quantum dots with an excited electron-hole pair in the wetting layer cannot be described by this model, because other formations of the trion are not considered [119].

Model B

This model is suitable for n-doped self-assembled quantum dots where a trion is formed due to an excitation in the wetting layer. It is assumed that after the relaxation of the electron to the ground-state the electron spin is still oriented while the hole spin has been randomized during the relaxation to the ground-state. As illustrated in Figure 2-5 four different trion constellations occur with equal probability. The states (a), (b) and (f) lead to radiative excitation, whereas (e) leads to a dark recombination. (a) and (b) will result in the same circular polarization as the excitation light. The state (f) shows the NCP-effect. It was experimentally shown that within the first 20 ps after the excitation the photoluminescence has the same circular polarization as the excitation light. After 20 ps the intensity drops rapidly and for times up to ~1 ns a rising of NCP is detected after which it decays [109]. The fast recombination was identified as state (b). It is an electron-hole spin flip process which allows for the excited electron to relax very quickly into the ground-state. The slower recombination of about ~1 ns was identified as state (e). For the dark state (e) the asymmetric exchange interaction is much smaller, so that the spin-flip process is due to the spin-orbit coupling. This recombination will result in NCP, so that the overall net circular polarization will be 50% and the majority of the remaining electrons will be spin-down.

Model C

This model is also suitable for n-doped self-assembled quantum dots. It is assumed that a photo-excited electron keeps its spin orientation during the relaxation from the wetting-layer to the ground-state of the quantum dot, just like in model B. The main difference to the model B concerns the dark trion state (f). In the case of two electrons with the same spin orientation, with one electron occupying the ground-state and the other electron occupying the first excited state, the exchange interaction of the hole with the two electrons completely suppresses the independent hole spin relaxation. Due to the suppressed relaxation the probability of the generation of a dark trion equals zero [120]. In the case of two electrons that both occupy the ground-state and are coupled so that the total spin is zero, the exchange interaction is almost negligible. Then the hole spin can relax with a probability q.

As shown in Figure 2-5 the only constellation in which NCP occurs is state (b). n_{p} represents all quantum dots where the resident electron has the same spin orientation as the photoexcited electron. Quantum dots with an opposite orientation of the resident electron do not contribute to the NCP-effect and are represented by n_{o}. The amplitude of the detected negative circular polarization (A_{NCP}) is proportional to $n_{\mathrm{p}} - n_{\mathrm{o}}$, because a positive circularly polarized emission will mix with a negative circularly polarized emission. During a detection such mixing of circularly polarized emission leads to a decrease of negative circularly polarized light. One should keep in mind that not all quantum dots of one sample have one resident electron, but that through the detection of the NCP-effect only those quantum dots who have a resident electron are studied.

2.2.2 Influence of the transverse magnetic field on the NCP-effect (Hanle-effect)

In the considerations presented so far, the optical axis was the quantization-axis and only two orientations of the spin were possible. The presence of a magnetic field leads to an interaction with the magnetic moment of the particles and induces the Larmor precession. The magnetic field $\boldsymbol{B}_{\mathrm{tot}}^{\mathrm{e}}$ is the total magnetic field that acts on the electron and is a sum of the Overhauser $\boldsymbol{B}_{\mathrm{N}}$, the nuclear fluctuation field $\boldsymbol{B}_{\mathrm{NF}}$ and the externally applied magnetic field $\boldsymbol{B}_0$

$$\boldsymbol{B}_{\mathrm{tot}}^{\mathrm{e}} = \boldsymbol{B}_{\mathrm{N}} + \boldsymbol{B}_{\mathrm{NF}} + \boldsymbol{B}_0 \tag{2.28}$$

and determines the quantization-axis for the Larmor precession. Interactions based on the electron spin are absent for a system of coupled electrons with the total spin equal to zero, as given in a constellation of a cold trion. After an electron-hole recombination has taken place the only remaining electron in the ground-state is the resident electron. The total spin

is given now by the resident electron which has a non-zero spin so that an interaction with $\boldsymbol{B}_{\mathrm{tot}}^{\mathrm{e}}$ occurs and the resident electron precesses with the Larmor frequency ω_{L}.

$$\omega_L = \mu_{\mathrm{B}} |g_s| \, \boldsymbol{B}_{\mathrm{tot}}^{\mathrm{e}} / \hbar \tag{2.29}$$

The Larmor precession of the resident electron is interrupted when a second electron is injected into the ground-state, e. g. a photo excited electron. The duration of the Larmor precession is given by T_{pre}. The amplitude of the negative circular polarization A_{NCP} is proportional to $\langle \boldsymbol{S}_{\mathrm{z}} \rangle$, the time-average z-component of the resident electron that precess with the Larmor frequency. It is also possible to determine the time dependent value $\boldsymbol{S}_{\mathrm{z}}(t)$ in a static magnetic field $\boldsymbol{B}_{\mathrm{tot}}^{\mathrm{e}} = \left(B_{\mathrm{x}}^{\mathrm{e}}, B_{\mathrm{y}}^{\mathrm{e}}, B_{\mathrm{z}}^{\mathrm{e}}\right)$ that has three components in space [121].

$$\boldsymbol{S}_{\mathrm{z}}(t) = \frac{\boldsymbol{S}_0}{(\boldsymbol{B}_{\mathrm{tot}}^{\mathrm{e}})^2} \left[(B_{\mathrm{z}}^{\mathrm{e}})^2 + (B_{\mathrm{x}}^{\mathrm{e}})^2 \left(B_{\mathrm{y}}^{\mathrm{e}}\right)^2 \cos \omega t \right] \tag{2.30}$$

The values of $\boldsymbol{S}_{\mathrm{z}}(t)$ depend on the absolute value of $\boldsymbol{S}_0$ and the angle α, between $\boldsymbol{B}_{\mathrm{tot}}^{\mathrm{e}}$ and the z-axis. For a better understanding of this formula one can consider the following example: given the simplified condition that $\boldsymbol{B}_{\mathrm{tot}}^{\mathrm{e}}$ only consists of one component $\boldsymbol{B}_{\mathrm{x}}$, so that the magnetic field $\boldsymbol{B}_{\mathrm{tot}}^{\mathrm{e}}$ is perpendicular to the initialized electron spin and given that the sample is excited with σ^+ polarized light, then the possible values of $S_{\mathrm{z}}(t)$ are $-S_0 \leq S_{\mathrm{z}}(t) \leq +S_0$. For α in the range of $0° \leq \alpha < 90°$ the value $S_{\mathrm{z}}(t) > 0$ can be reached, for α in the range of $90° < \alpha \leq 180°$ the value of $S_{\mathrm{z}}(t) < 0$. For α= 90° the value of $S_{\mathrm{z}}(t) = 0$. An increase of $\boldsymbol{B}_{\mathrm{tot}}^{\mathrm{e}}$ leads to an increase of the angle α, because then the time $\mathrm{T}_{\mathrm{pre}}$ is not influenced by the magnetic field, while the precession frequency increases. As a consequence of the increased magnetic field $\boldsymbol{B}_{\mathrm{tot}}^{\mathrm{e}}$, the value of $S_{\mathrm{z}}(t)$ is reduced, therefore the measured amplitude A_{NCP} is also reduced. For the first time this dependence of A_{NCP} on the magnetic field under these simplified conditions was described by W. Hanle. Therefore it is called the Hanle-effect. Measurements which detect the degree of polarization under the influence of a magnetic field perpendicular to the initialized spin are called Hanle-measurements and the resulting curves are called Hanle-curves [122]. The shape of A_{NCP} in the dependence on $\boldsymbol{B}_{\mathrm{x}}^{\mathrm{e}}$ is a Lorentzian curve, which is given by the following equation

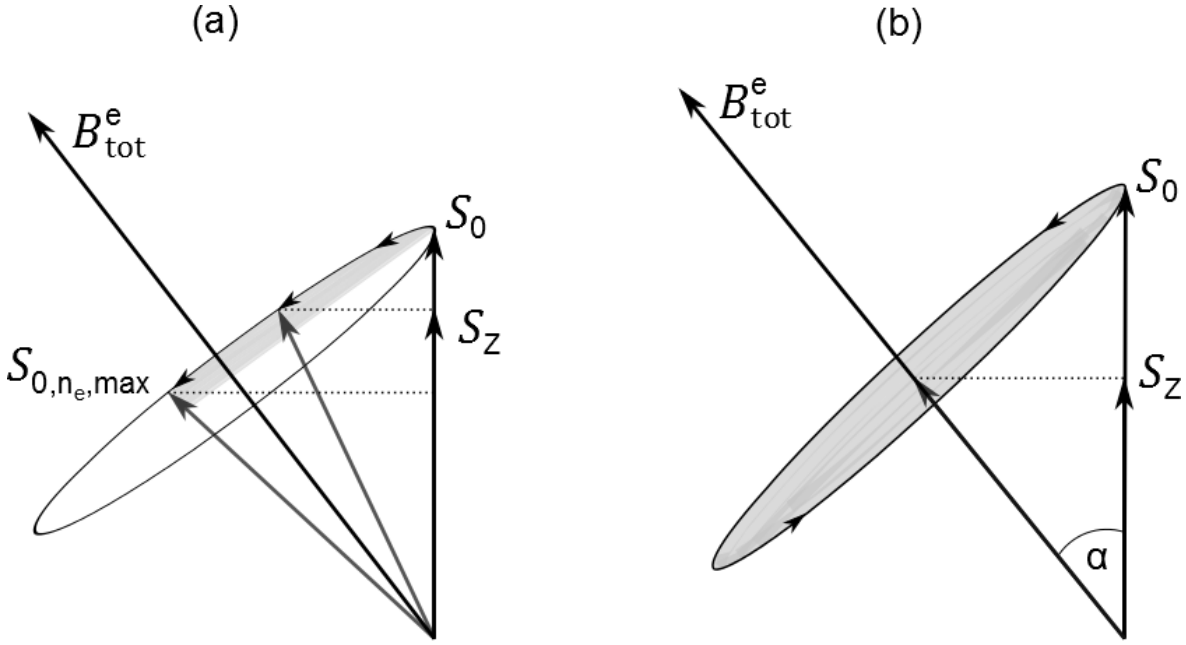

Figure 2-6 Precession of an electron spin due to the magnetic field $\boldsymbol{B^{e}_{tot}}$. The gray area indicates the extent of precession of $\boldsymbol{S_0}$ within the magnetic field $\boldsymbol{B^{e}_{tot}}$ until the precession is interrupted by the formation of a "cold trion". (a) indicates the situation with a shorter $\boldsymbol{T_{pre}}$ time than in case of (b). The vector $\boldsymbol{S_{0,n_e,max}}$ indicates the maximum position of $\boldsymbol{S_0}$ within the Larmor precession. The projection $\boldsymbol{S_z}$ indicates the average value of all electrons of the quantum dot ensemble. (b) indicates the situation with a longer $\boldsymbol{T_{pre}}$ time than in case of (a). The whole area of the precession is gray, which indicates that $\boldsymbol{S_0}$ fulfills at least one period of precession. In this case the magnitude of the projection $\boldsymbol{S_z}$ is smaller than in case of (a).

$$\boldsymbol{S}_{\mathrm{z}}(B_x) = \frac{\boldsymbol{S}_{\mathrm{z}}(0)}{\left(\frac{g\ \mu_{\mathrm{B}}\ B^{\mathrm{e}}_{\mathrm{x}}\ T_3^*}{\hbar}\right)^2 + 1} \tag{2.31}$$

T_3^* is the effective transverse spin lifetime of the electron and consists of $\frac{1}{T_3^*} = \frac{1}{\tau_{\mathrm{r}}} + \frac{1}{\tau_{\mathrm{s}}}$, where τ_{r} is the recombination lifetime and τ_{s} is the spin relaxation time [123]. If the g-factor of the precessing electron is known, then the effective transverse spin lifetime can be extracted from the measurement by determining the half width at half maximum $B_{1/2}$ of the Hanle-curve. The dependence of $B_{1/2}$ and T_3^* is given by

$$B_{1/2} = \frac{\hbar}{\mu_{\mathrm{B}}|g|} \cdot \frac{1}{\tau_{\mathrm{r}}} + \frac{1}{\tau_{\mathrm{s}}} \tag{2.32}$$

The Hanle-curves obtained in this thesis cannot be analyzed with eqs.(2.31) and (2.32) because the requirement of the magnetic field being perpendicular to the initialized electron spin is not fulfilled at every point of the Hanle-curve. In this thesis the conditions given experimentally are more complex since not only the magnitude of the different components of $\boldsymbol{B^{e}_{tot}}$ changes with the externally applied magnetic field, but also the direction of the

components of $\boldsymbol{B}_{\mathrm{tot}}^{\mathrm{e}}$ changes in time. A more detailed discussion of these circumstances is given in secs. 4.2.4 , 4.1.2 and 4.1.3.

It is important to distinguish between two types of excitation, because experiments show that the nuclear polarization depends on the type of laser used for excitation (ref. to sec. 4.5.1). For the first type of excitation (i) a continuous wave laser is used, with the spectral width being less than 1nm. In this case the electron-hole pairs are excited continuously. For the second type of excitation (ii) a pico second laser is used, where every 12.5 ns a light pulse with a spectral width of several tens of nanometers hits the sample. In this case the electron-hole pairs are excited discontinuously.

In case of excitation with a CW-laser (i), in every quantum dot the spin precession of the resident electron starts at a different time, due to the continuous excitation. This precession is a not coherent process. Consequently, the projection of $\boldsymbol{S}_0$ on the z-axis has a different length for every quantum dot. Therefore the detection of A_{NCP} will be proportional to an average value of $\boldsymbol{S}_{\mathrm{z}}(t)$. For simplicity reasons, this average value will be called $\boldsymbol{S}_{\mathrm{z}}$. The time τ_{cee} between consecutive excitation events, that create an electron-hole pair, depends on the CW-laser power density. Reducing the excitation power density reduces also the probability of an electron-hole excitation, resulting in a smaller amount of electron-hole pairs that can relax to the ground-state. For low excitation power densities τ_{cee} is larger than for high excitation power densities. The less electron-hole pairs relax to the ground-state, the smaller is the probability to find two coupled electrons occupying the ground-state. The recombination lifetime of a ground-state electron-hole pair is $\tau_{\mathrm{r}}{\sim}1\ \mathrm{ns}$ [120], so after this time only the resident electron occupies the ground-state of the QD. The larger the difference of τ_{cee} and τ_{r}, the longer is the duration of the Larmor precession T_{pre} of the resident electron. A smaller τ_{cee} leads to a smaller T_{pre} time. An estimation of τ_{cee} for an average CW-laser power density, as it is used for the studied samples, is given in sec. 4.3.2. The estimation in sec. 4.3.2 shows that an average CW-laser power density leads to a smaller τ_{cee} time than a pico second laser excitation (ii) with a repetition rate of 12.5 ns.

For an excitation with a pico second laser (ii) the time τ_{cee} is determined by the repetition rate of the laser. Due to the above mentioned relation of τ_{cee} and T_{pre} and the fact that the pulse duration of the pulsed laser is ∼125 fs, the duration of the Larmor precession is also determined by the repetition rate of the pulsed laser. Under such conditions the resident electron can precess several periods, even in magnetic fields smaller than 1 Tesla. The smallest magnetic field that acts permanently on the electron is the nuclear fluctuating field, which is several tens of millitesla. Here the precession period has a duration of several nanoseconds, so that even without an external magnetic field more than one precession is possible.

By excitation with circularly polarized light above the bandgap of the quantum dot an electron-hole pair is created. The angular momentum of the circularly polarized light is conserved by this process, which leads to an orientation of the electron and hole spin along

the excitation axis. Excitation with σ^+ polarized light leads to an angular momentum transfer of +ħ and creates an electron spin -1/2 and a hole spin +3/2. Table 2-2 shows the configurations of the electron and hole spins that result from an excitation with σ^+ or σ^- polarized light.

Photon helicity	Expression	Polarization	Rotation of **E**	S_e	S_h
$+\hbar\mathbf{k}/k$	Right circular	σ^+	Right handed	-1/2	+3/2
$-\hbar\mathbf{k}/k$	Left circular	σ^-	Left handed	+1/2	-3/2

Table 2-2 Summary of definitions concerning circular polarized light. Rotation of the **E** field vector defined for the light wave propagating towards the observer and the corresponding spin orientation of the excited electron-hole pair.

3 Experimental setup and samples

This section presents the setup that is used to obtain the experimental data that are presented in this thesis. The first part separates the used devices into optical, electronic and cryogenic devices and gives detailed information about the usage. Afterwards introductory measurements are presented, which give a first insight into the used samples and parameters that have an influence on the collected data. This section gives a standard set of conditions which are necessary to obtain a usable signal. At the end is a section about self-assembled quantum dots. A discussion about the general possibilities of growing nanostructures, which points out the growing technique for the used quantum dot structures is given as a prelude. At the end of this section is a detailed presentation about the growing conditions of the used quantum dots.

3.1 The setup

3.1.1 Optical elements

An illustration of the Hanle measurement setup is shown in Figure 3-1. The superconducting magnet inside the cryostat gives a homogeneous magnetic field parallel to the x-axis. The optical axis is parallel to the z-axis, so that all optical elements lie within the xz-plane. The sample is mounted on the height of the optical axis and the surface of the sample is oriented orthogonally to it. In this position the growing direction of the quantum dots is parallel to the optical axis and orthogonal to the magnetic field of the superconducting magnet.

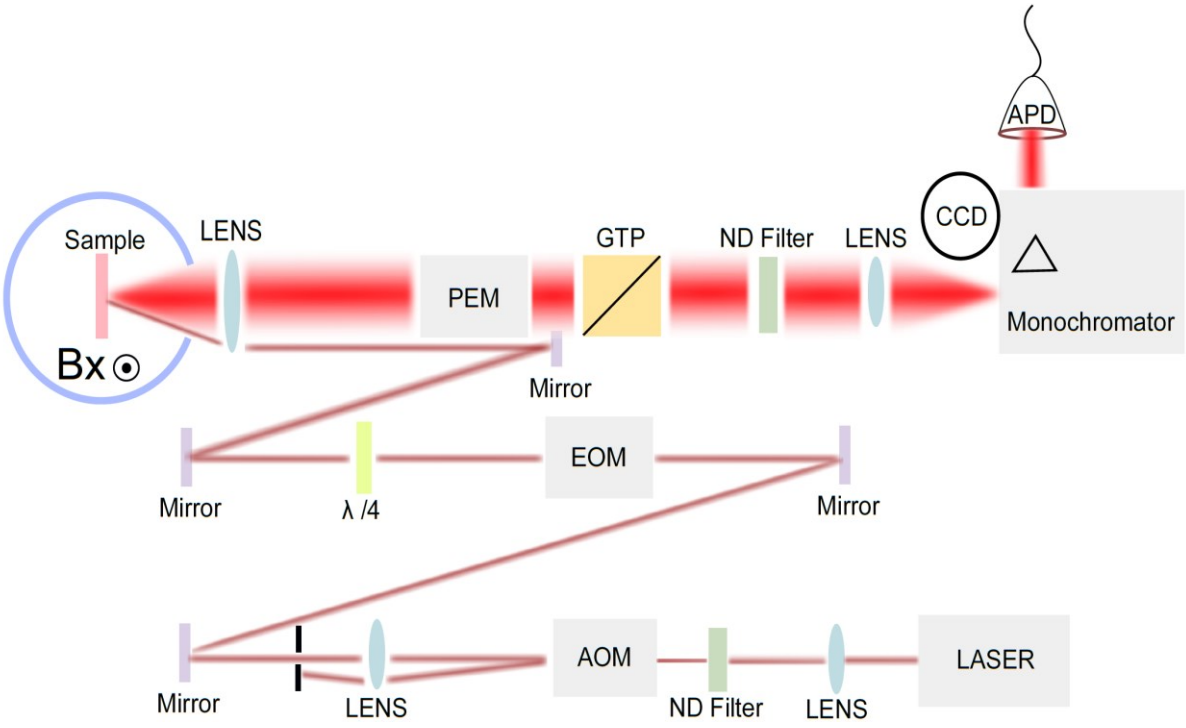

Figure 3-1 Schematic illustration of the optical elements used in the setup to obtain Hanle-curves and PL spectra. The different colors of the laser beam and the photoluminescence indicate different wave lengths. A more detailed description of the elements is given in the main text.

The optical elements can be divided into three groups: the excitation group, the manipulation of the beam group and the detection group.

The excitation group is separated into two parts, depending on whether a CW-laser excitation or a pulsed laser excitation is used. For the CW-laser excitation a pump laser and a titanium-sapphire-laser are used. As a pump laser the solid-state Nd:YAG laser (Verdi V5, Coherent) is used that operates at 532 nm and gives an output of 5W. The TiSa laser (Tekhnoscan) can be tuned in a range of 750 – 850 nm. The pulsed laser is a modelocked TiSa femtosecond laser with a pulse repetition rate of 12.5 ns (repetition frequency = 80 MHz) and a pulse duration of ∼125 fs (Coherent, Cameleon). It is tunable in the range of 720 – 950 nm.

The laser beam can be manipulated in intensity by the use of an acousto-optic modulator (AOM). The crystal of the AOM is transparent for the laser light and is periodically deformed by a piezo- element with a frequency of 80 MHz. This deformation causes fluctuations of the density of the crystal. These fluctuations of density can move in the crystal as a plane wave forwards and backwards and thereby create a stationary density wave. Thus, a periodic structure with regions of high and low density is established. In comparison to regions of a lower density, regions of a higher density have a different refraction index for an incoming light beam. The periodic structure acts on an incoming light beam like a Bragg grating so that the beam starts to interfere with the reflected light of the beam. The AOM can be connected to a function generator, so that the amplitude of the laser beam can be controlled by the function generator. The ramp up (ramp down) time to reach the highest (lowest) intensity of the outcoming beam is about 100 ns. For a good optical adjustment of the AOM, the outcoming light can completely be blocked. The angle between the incoming light and the crystal surface needs to be about 15°. The EOM can rotate the polarization plane by 90° so that horizontally polarized light becomes vertically polarized. Applying an electric field to the four crystals of the EOM causes a change of the refraction index so that the electric field component of light can be delayed in relation to the magnetic field component. A linear relation between the change of the refractive index and the applied electric field is called the Pockels-effect. A quadratic dependence between the change of the refractive index and the applied electric field is called the Kerr-effect. Both effects are present in the used EOM (LM0202, Linos), but the Pockels-effect is dominant. The naturally given but in this case unwanted birefringence effect of a crystal is compensated by four crystals in a row. The change of polarization from horizontal to vertical polarization takes less than 2 ns. The shortest modulation frequency is limited by the digital pulse amplifier (LIV20, Linos) that can apply voltage to the crystals of the EOM with a maximum frequency of 500 kHz. In combination with a $\lambda/4$ waveplate one can excite the sample with right and left handed circular polarization. The EOM can handle light in a range of 650 - 1000 nm.

To detect the degree of circular polarization from the ground state energy of the quantum dots it is needed to :

1. Separate the $\sigma^+$and σ^- components of the photoluminescence (PL).

2. Select the ground excitation of the quantum dots of the signal spectrum.

3. Detect the intensity of the ground state excitation of the quantum dots.

The operation frequency of the photoelastic modulator (PEM) is 50 kHz. During this period a piezo crystal induces strain to the fused silica plate crystal of the PEM. When the fused silica crystal is compressed it operates as a λ/4 wave plate (~5 µs after the trigger signal). When the fused silica crystal is stretched it operates as a -λ/4 plate (~15 µs after the trigger signal). After 5 µs the σ^+ polarized PL is converted to vertically polarized light and the σ^- polarized PL is converted to horizontally polarized light. Figure 3-2 shows the complete modulation process of the PEM. Because of the Glan-Thompson prism behind the PEM only vertically polarized light can pass the prism. The combination of a PEM and Glan-Thompson prism allows to separate the σ^+ and σ^- polarized light of the PL.

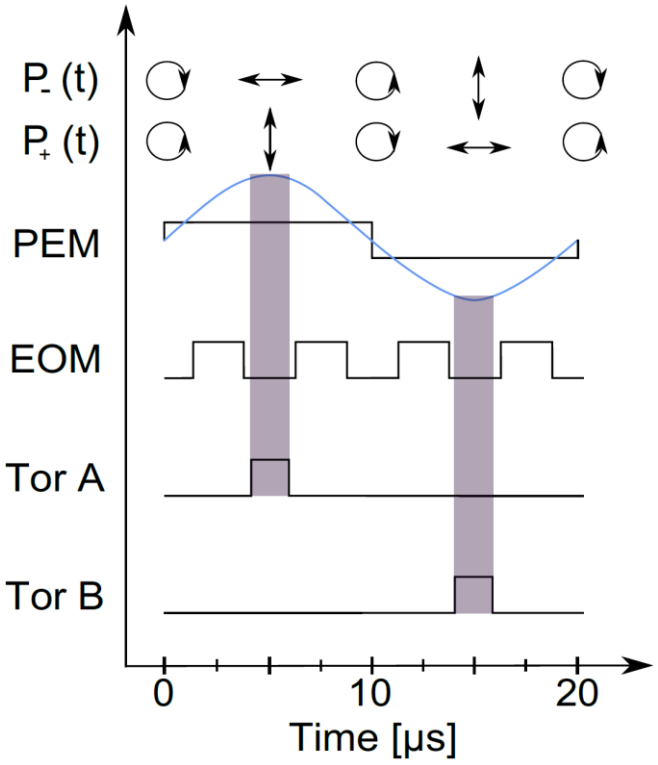

Figure 3-2 $\boldsymbol{P}_+(\boldsymbol{t})$ and $\boldsymbol{P}_-(\boldsymbol{t})$ indicate the development of the PL polarization due to the modulation of the PEM. At the beginning of the modulation (t=0) the polarization for $\boldsymbol{P}_+(\boldsymbol{t}) = \boldsymbol{\sigma}^+$ and for $\boldsymbol{P}_-(\boldsymbol{t}) = \boldsymbol{\sigma}^-$. The blue sine curve indicates the phase of the PEM. The horizontal and vertical arrows indicate that the PL polarization changes to horizontally and vertically linear polarized light at the corresponding position of the PEM. The positions of the gated detection relative to the PEM are shown at the bottom of the Figure.

For a spectral resolution of the PL a half meter spectrometer (Acton 500) with three different gratings (300 g/mm, 600 g/mm and 1200 g/mm) can be used. The higher the density of the grating, the stronger the incoming light is dispersed and the spectral resolution becomes higher. For every measurement in this thesis a grating with 600 g/mm suffices. The computer program "WinSpec/32" is used to show the spectra of the PL collected by a nitrogen cooled silicon CCD (400x1340 pixel). The grating spectrally splits the light in a horizontal direction. Therefore only the horizontal resolution of the SI-CCD is important. The signal of the vertical pixels can be integrated, so that the effective resolution of the SI-CCD is 1x1340 pixels. By the program "WinSpec/32" it is also possible to determine a central wavelength and to direct only the intensity of the central wavelength to an avalanche photodiode (SPCM-AQR-14, Perkin Elmer). The avalanche photodiode shows a linear relationship between the output voltage and counted photons up to a counting rate of 10^9 photons/second.

3.1.2 Electronic elements

The function generator (AFG 3022, Tektronix) has two channels, channel A and Channel B. Channel A is used to send the modulation signal to the EOM, while channel B is used to generate the RF signal for the RF-coil. A TTL square wave signal is sent to trigger the EOM. The maximum output in the high Z regime of channel B is 10 V peak to peak. The two signals of channel A/B always have a defined phase that can be changed depending on the measurement conditions. The output of channel A is also connected to the first input of a signal counting device (PicoHarp 300, PicoQuant), providing a total of three inputs. The second input of the PicoHarp is the trigger signal of the PEM and the third input is the signal of the avalanche photodiode. A connection with the computer is given through the output of the PicoHarp. Depending on the measurement protocol a set of different programs can be used to operate with the PicoHarp.

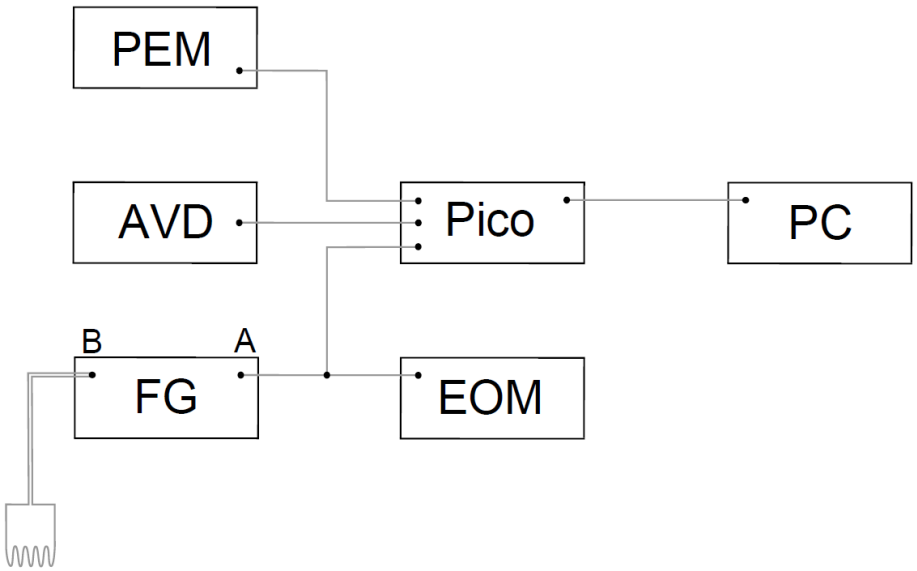

Figure 3-3 Schematic illustration of the electric elements used in the setup to obtain Hanle-curves. A more detailed description of the elements is given in the main text.

The EOM can be used in two different operation modes. In both operation modes the PicoHarp continuously collects the counts of the avalanche photodiode. The counts are weighted, depending on the phase of the PEM. The weighting oscillates with a sine function of equal frequency as the PEM modulation and with a maximal amplitude of 1. During the time when the PEM operates as a +λ/4 (or –λ/4) waveplate the weighting is 1 for σ^+ (or σ^-) polarized PL, since only then σ^+ (σ^-) polarized light can pass the Glan-Thompson prism (compare Figure 3-2). Later a self-programmed software uses the weighted counts of the σ^+ (σ^-) polarized PL to calculate the polarization degree of the PL.

$$\rho = \frac{I^+ - I^-}{I^+ + I^-} \tag{3.1}$$

In the first operation mode the EOM sustains one polarization during the measurement. In the second operation mode the function generator sends the square shaped modulation signal which is fixed in frequency to the EOM and the PicoHarp. The modulation signal of the PEM is also sent to the PicoHarp, so that the PicoHarp receives information about the phase and modulation frequency of both modulators. The signal of the function generator is not synchronized with the PEM and is different in frequency. The result is a moving in time of the region where the PEM operates as a λ/4 waveplate over the modulation of the EOM. As long as the modulation frequency of the EOM is different from the modulation frequency of the PEM, every position of the polarization modulation created by the EOM can be reached by the position where the PEM operates as a λ/4 waveplate.

The superconducting magnet within the RTI cryostat (Oxford) is oriented in a Voigt geometry and connected to a power supply (Bop 100-10MG, Kepco) with a maximum current of 10 A. With a conversion factor of 15.1 A/T magnetic fields in a range of 1 Tesla can be achieved. The RF-coils are powered by a high Z output (output B) of the function generator with a maximum output of 10 V peak to peak.

3.1.3 Cryostat

The Magneto-optical cryostat (RTI) has a 12 liter reservoir for liquid helium. A vacuum pump (Model IP54, Firma Leroy Somer) can be connected to this reservoir in order to reach the lambda point, where helium becomes superfluid. It is possible to attain temperatures down to 1.6 K when the vacuum pump operates at maximum performance. Using a Pt-100 resistor near the sample position, the temperature can be detected by four-terminal sensing. Superfluid helium nearly has a perfect thermal conductivity, thus there is no gradient of temperature within the superfluid helium. This has two advantages for magneto-optical measurements. At first, the superfluid helium serves as a very efficient cooling for the laser light excited sample and the superconducting magnets. Secondly, the superfluid helium can only evaporate on the boundary layer between the gaseous and superfluid helium. There are no bubbles due to boiling of the superfluid helium that could disturb the PL or the excitation of the sample by laser light. There are two provisions necessary to prevent the helium from vaporizing too fast. The first provision is a cylindrical nitrogen cooled copper cloak around the helium reservoir that shields the helium from thermal radiation. The second provision is a vacuum chamber with a vacuum of about 10^{-6} mbar around the helium and nitrogen reservoir. It can be achieved by a turbo vacuum pump (Model TSH-071, Pfeiffer).

3.1.4 Introductory measurements for signal maximization

All of the presented measurements in this thesis are Hanle-curves obtained by detecting the circularly polarized luminescence of self-assembled (In,Ga)As/GaAs quantum dot structures in superfluid helium at temperatures of $T \sim 1.8\ \mathrm{K}$. The two samples studied have an identical growing structure and differ only in the annealing temperature. Sample #980 is annealed at 980°C and sample #900 is annealed at 900°C (for details concerning the growing conditions refer to sec. 3.2.2). Each sample has a set of four parameters that can be optimized to obtain the maximum amplitude possible of circularly polarized photoluminescence A_{NCP}.

These four parameters are:

1. Variation of the excitation density,

2. Variation of the detected wavelength,

3. Variation of the excitation wavelength,

4. Variation of the laser spot position on the sample.

The optimal excitation wavelength for sample #980 is 838nm (1.49 eV) with a detection wavelength of 871 nm (1.42 eV). The optimal excitation wavelength for sample #900 is 846 nm (1.47 eV) with a detection wavelength of 924 nm (1.34 eV). The tuning of the excitation density and the laser spot position on the sample depend on the requirements of the measurement and influence the total polarization degree of A_{NCP} by ~5%. If not mentioned otherwise, the excitation density is tuned to a value where A_{NCP} reaches its maximum amplitude at $B_{\mathrm{x}} = 0\ \mathrm{mT}$. A further increase of the excitation density leads to a saturation of the A_{NCP} amplitude, which indicates the highest level possible of electron spin polarization. For sample #980 the maximum electron polarization is reached at a time averaged intensity of 1.5 mW, for sample #900 at 10 mW. A higher excitation power leads to a decrease of A_{NCP}.

3.2 Self-assembled quantum dots

As described in the introduction, due to their limited expansion in space, quantum dot structures act on electrons and holes like potential wells in all spatial directions. Discrete energy levels and spatial localization are two main features of charge carriers in quantum dots. There is a large variety both of construction processes of such nano structures and of the used materials. Typical compositions are InP/InGaP [124], Ge/Si [125], InSb/GaSb [126], GaSb/GaAs [127], InAlAs/AlGaAs [128] for 3-5 semiconductors and CdSe/ZnSe [129] for 2-6 semiconductors. One of the most important techniques for growing nanostructures is the molecular beam epitaxy (MBE), because it grants a very slow epitaxial growing and a large variety of possibilities of postprocessing the structures. The main part of a MBE growing machine is the vacuum chamber with a ultra-high vacuum of 10^{-11} mbar. Several effusion cells reach inside this chamber of which each contains a different element that can evaporate on the substrate. The process of evaporating can be controlled by the heater and the shutter of the effusion cell. For improvement of a homogeneous growing process the sample is mounted on a rotatable sample holder. A mass spectrometer and an electron beam source, the RHEED (reflection high energy electron diffraction), are located close to the sample for controlling the growing process. The Bragg reflection of the electron beam gives a characteristic pattern of the first monolayers of the sample depending on the

crystalline structure of the sample surface. By the intensity of the reflected beam it is possible to map the growing process, since only the flattest and most homogeneous surface gives the strongest Bragg reflection. The deposition of material on the substrate can be characterized by the relation of three parameters, namely the material γ_m and the substrate γ_s surface energies and the energy of material/substrate interface γ_{ms}. For the trivial case of homoepitaxy growing, which means deposition of the same material on the substrate as the substrate consists of, $\gamma_{ms} = 0$ and $\gamma_m = \gamma_s$. In the case of heteroepitaxial growing it is possible to distinguish between three modes of growing conditions [130].

1. Volmer-Weber ($\gamma_s < \gamma_m + \gamma_{ms}$) [131],
2. Frank-Van der Merwe ($\gamma_s > \gamma_m + \gamma_{ms}$) [132],
3. Stranski-Krastanow (mixture of Frank-Van der Merwe and Volmer-Weber mode) [133].

The Volmer-Weber mode is possible if the lattice mismatch of the deposited material and the substrate is large in comparison to the other modes. To lower the interface energy and their own surface energy the deposited atoms are bound stronger to each other than to the substrate. As a result, islands of deposited atoms on the substrate are created, preferentially on locations that lower the activation energy for nucleation like crystal defects, atomic steps or impurities. The small islands grow larger rather than coating the substrate surface.

The Frank Van der Merwe mode is possible if the lattice mismatch is weak. It is also called a layer by layer growth. It means that the deposited atoms completely cover the surface of the substrate before a second monolayer starts to grow. This process is called a "wetting" of the substrate. But with a rising number of monolayers also the strain within the deposited layers increases. Each composition of the substrate and deposited material has a critical thickness where the layer by layer growth is no longer possible. The resulting dislocation of deposited atoms leads to a fluctuating surface thickness of the deposited atoms. These fluctuations are called "natural quantum dots" [134].

3.2.1 Stranski-Krastanow mode

At the beginning of the growing process with this method [135] is the relation $\gamma_s > \gamma_m + \gamma_{ms}$, but with a rising number of monolayers strain effects start to influence γ_s. Then the left side of the inequality needs to be replaced by the total energy $E_{total} = \gamma_s + \gamma_{strain}$. By definition $\gamma_{strain} = -\kappa V$ is always negative and $\gamma_s = \beta V^{\frac{2}{3}}$ is always positive. κ and β are coefficients given by the Poisson ratio, shear modulus of the substrate and the free energy of the surface that describe the shape of the islands [136]. Due to the different evolution of γ_s and γ_{strain} with increasing volume *V* of deposited material, E_{total} changes sign at a critical

volume V^*. The inequality in the case of $V > V^*$ can be written as $\mathrm{E_{total}} < \gamma_m + \gamma_{ms}$. This indicates the appearance of a growing island. Because of the wetting process at the beginning of the Stranski-Krastanow mode the quantum dots grow on the so called wetting layer and not directly on the substrate. An example of further specifics of thin film growth modes and separation of wetting and cluster nucleation is given by H. Marcia et al [137]. With the three growing modes, several growing techniques can be realized. Because of the large number of growing techniques only a few possible techniques will be mentioned in this thesis. After growing a wetting layer on the substrate it is possible to use electron beam lithography or wet chemical etching to modulate the structure of the surface [138]. This method is time expensive and requires several working stages. However, it allows the construction of individually shaped structures.

The cleaved-edge overgrowth (CEO) process is a three step process. The first step is a common growing of a quantum well on a substrate in (001) direction. Afterwards the sample is removed from the growing chamber and thinned from the backside to about 100 µm. In the second step the sample is mounted back in the growing chamber, but this time with the (110) direction turned on top. An in situ cut exposes a new (110) surface. Finally a second growing process leads to the formation of quantum dots or a quantum well, depending on the growing parameters [139]. In contrast to the quantum dots obtained on a (001) substrate, the same growing conditions applied on a (110) substrate lead to misfit dislocations and much bigger island structures [140, 141]. The shape of quantum dots obtained on a (001) substrate is lens-shaped and more homogeneous in size than on a (110) substrate. Growing of quantum dots on a (110) substrate leads to a trapezoidal-shape. A growing of a quantum well in the third step of CEO on the (110) substrate leads to the formation of a T-shape structure where electronic states are quantum mechanically confined [142]. This quantum-wire shows nearly ideal quantum transport characteristics [143]. This growing technique is very time expensive and affords the study of electronic states in quantum wires formed by an arbitrary combination of two constituent quantum wells with different thicknesses [144].

3.2.2 Studied quantum dots

In this thesis, the self-assembled quantum dots are an example of the Stranski-Krastanow mode. The quantum dots are grown on a (001) GaAs substrate that is heated to a temperature of about 600°C during the growing process. At first, alternating layers of AlAs and GaAs quantum wells are grown. Because of the small lattice mismatch of about 0.3% between AlAs and GaAs, the growing process can be controlled well, so that the material can be deposited monolayer by monolayer on the substrate. This ensures a flat surface for the following growth of the quantum dots. Because of a lattice mismatch of 7% between InAs and GaAs the deposition of Indium and Arsenic atoms on a GaAs surface leads to quantum dot formation by the Stranski-Krastanow mode. The quantum dots of the sample used have a diameter of about 10 – 30 nm and a distance of 30 – 100 nm and are delta doped with silicon. The doping leads to a permanent occupation of one electron per quantum dot. After

the delta doping the quantum dots are covered with a GaAs capping layer. As shown in Table 3-1 the presented structure is repeated twenty times so that the average density of the quantum dots is $10^{10}/\mathrm{cm}^2$ to $10^{11}/\mathrm{cm}^2$.

Layer	T [°C]	Duration [s]	Thickness[nm]	Repetition
GaAs substrat	-	-	-	-
GaAs	660	531.9	100	
AlAs	660	20	2	Start 20x
GaAs	660	5.3	1	End 20x
AlAs	660	20	2	
GaAs	660	425.5	80	
				Start 20x
InAs	590	4	0.3	16x
GaAs	580	42.6	8	
GaAs	660	42.6	8	
Si-Delta	660	4	0	
GaAs	660	340.4	64	End 20x
AlAs	660	20	2	Start 20x
GaAs	660	5.3	1	End 20x
GaAs	660	531.9	100	
GaAs:Si	660	79.8	15	

Table 3-1 Growing conditions for quantum dots out of the series #11955.

Due to twenty layers of quantum dots, inciding light can interact with more quantum dots in comparison to a sample with one layer of quantum dots. This results in a higher intensity of photoluminescence and a stronger rotation angle in Faraday and Kerr rotation measurements.

Up to this point the conditions of sample growing are the same for every sample of the production series #11955. The differences between the samples are given by a set of various annealing temperatures in the range of 800 – 1000 °C. The results for this thesis are based on measurements with samples annealed at 900 °C and 980°C. As an example for the #11955 series several Scanning Transmission Electron Microscopy (STEM) images are presented in the appendix for the sample annealed at 820°C. Figure 0-1 and Figure 0-2 show a larger image of the sample to give an overview of the quantum dot structures. The darker regions in Figure 0-3 and Figure 0-4 are associated with strain. The darker the region, the stronger is the strain. Figure 0-3 shows a quantum dot with a symmetric strain (parallel to the growing direction), while the quantum dot in Figure 0-4 shows an asymmetric direction (not parallel to the growing direction). The analysis of images of many quantum dots shows that typically the dots are symmetric or strongly asymmetric. The annealing process is the final step of the growing process where the sample is heated for several seconds (~30 sec.) at a constant temperature without deposing any material on the sample. As a result of the heating some of the indium atoms of the dots are replaced by gallium atoms of the capping layer. In case of an equal timeframe for each heating, the amount of replaced atoms depends only on the

temperature used. The higher the temperature used, the larger is the amount of replaced atoms. These quantum dots that then consist of three isotopes are typically called $In_xGa_{1-x}As$ quantum dots. Strictly speaking the quantum dots are already impurified by gallium after the capping process. But the amount of gallium atoms is so small that the photoluminescence spectrum only becomes slightly widened. The annealing process enhances and unifies the impurity of the quantum dots caused by the gallium atoms which leads to a narrowing of the photoluminescence spectrum and shifts the light emission of the quantum dots to higher energies [121]. The probability of presence for electrons within a quantum dot also changes for samples with different annealing temperatures. Temperatures higher than 820°C increase the area of possible electron localization. With a larger area of electron localization the amount of nuclei increases which are influenced by the electrons trapped in the quantum dot. At the same time the probability of presence for a certain position is lower after the annealing process. Thus every nucleus has a smaller hyperfine interaction with the electron after the annealing process [145].

4 Results

4.1 Dynamic nuclear polarization of spin $\mathbf{I} \geq 3/2$ and $\mathbf{I} = 1/2$ ensembles

In this section the influence of the Overhauser field on the Hanle-curve excited with a CW-laser is presented.

This Overhauser field consists of two components that are perpendicular to each other. One component ($\boldsymbol{B}_{\mathrm{DNP}\parallel}$) is parallel, the other component ($\boldsymbol{B}_{\mathrm{DNP}\perp}$) is perpendicular to the externally applied magnetic field $\boldsymbol{B}_{\mathrm{x}}$. Due to the different dynamics of buildup and decay time and their different magnitude, that depends on the value of $\boldsymbol{B}_{\mathrm{x}}$, the two components can be treated as separate ensembles of polarized nuclei. In context with the experiments presented in chapter 4.4.3, the $\boldsymbol{B}_{\mathrm{DNP}\parallel}$ component can be identified as a polarization of spin $I = 1/2$ nuclei and the $\boldsymbol{B}_{\mathrm{DNP}\perp}$ component as a polarization of spin $I \geq 3/2$ nuclei [168]. In the first part of this section measurements are shown that deal with the buildup time of nuclear polarization. In the second part of this section the dependence of the Hanle-curve on the "dark time" is presented. By that it is possible to determine the decay time of nuclear polarization. The following section (sec. 4.1.1) will present a model that enables to separate the effect of $\boldsymbol{B}_{\mathrm{DNP}\parallel}$ and $\boldsymbol{B}_{\mathrm{DNP}\perp}$ on the Hanle-curve, so that the decay and buildup times can be discussed later in the text.

In order to analyze the time dependence of the Hanle- curve under continuous wave laser excitation, sample #900 is excited with σ^+ polarized light. The excitation protocol is a periodic repetition of amplitude modulation of the laser light, in which the excitation time $t_{\mathrm{exc}} = 50\ \mathrm{ms}$ is followed by a "dark time" $t_{\mathrm{d}} = 50\ \mathrm{ms}$. During the "dark time" the excitation is completely interrupted. The only function of the dark time is to erase all effects that could occur during the excitation of the sample. The signal is accumulated for 1 ms.

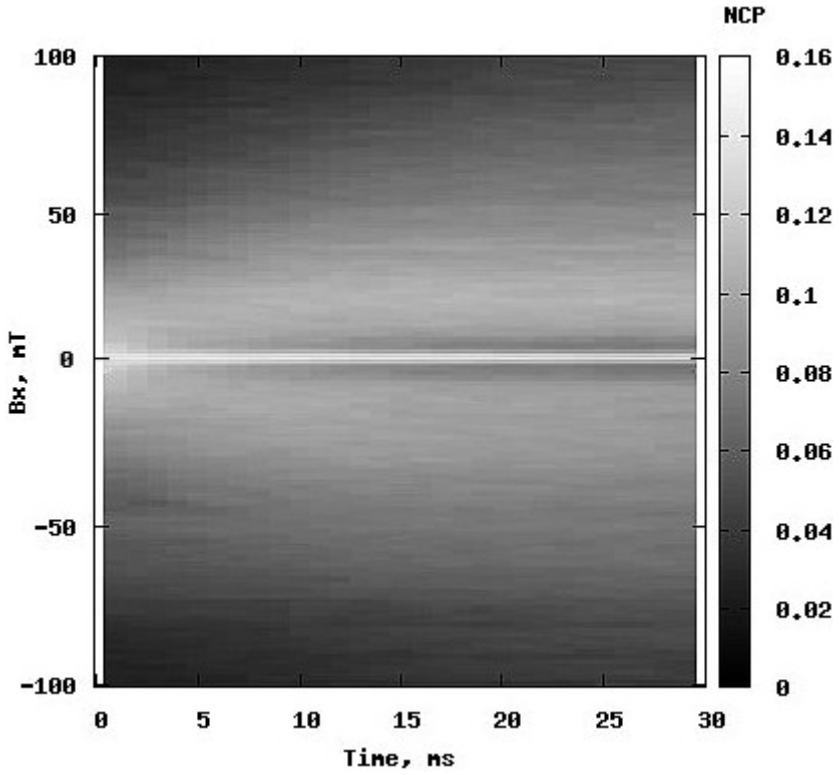

Figure 4-1 Degree of polarization measured as a function of magnetic field $\boldsymbol{B}_{\mathrm{x}}$ and time after the start of pumping. The grayscale bar on the right indicates the magnitude of A_{NCP}. The measurement is obtained with sample #900 under excitation at 1.47 eV, detected at 1.34 eV at temperature $T = 1.8\ \mathrm{K}$ [168].

The time resolution is also limited to 1 ms, so that the development of A_{NCP} can be traced fifty times during the excitation duration of 50ms. For every step on the time axis the external magnetic field $\boldsymbol{B}_{\mathrm{x}}$ is swept from -100 mT to +100 mT in steps of $\sim 0.6\ \mathrm{mT}$. The development of the Hanle-curve during the first 30ms of excitation is shown in Figure 4-1. After 30 ms no significant change of the Hanle-curve is detectable (ref. to Figure 4-3), because of that only the first 30 ms are shown in Figure 4-1. The first milliseconds after the excitation is switched on the Hanle-curve only consists of the central peak at $\boldsymbol{B}_{\mathrm{x}} = 0\ \mathrm{mT}$, which has a half width at half maximum of several mT. During the excitation, dips around the central peak appear. The formation of a second local maximum appears, so that the shape of the Hanle-curve becomes W-like. The curve becomes wider and reaches a maximum width after $\sim 30\ \mathrm{ms}$. After this time the Hanle-curve is identical to a Hanle-curve obtained under CW-laser excitation without dark time.

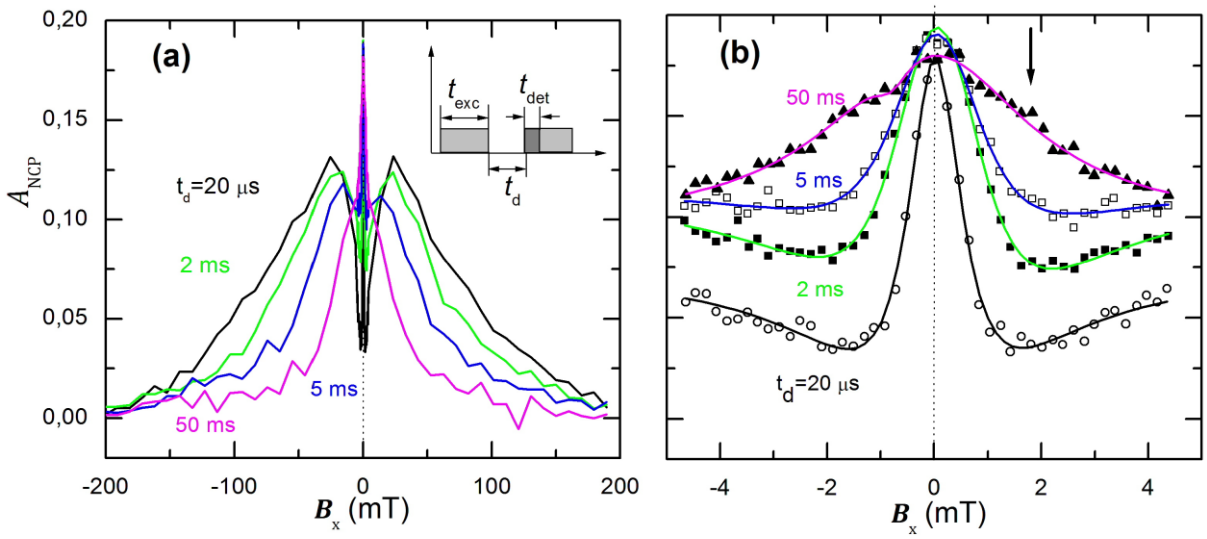

Figure 4-2 Hanle curves at constant excitation time t_{exc} = 50 ms, parameterized by dark time t_{d} (indicated at each curve): (a) complete curves; (b) central portions of curves. The arrow points to the lowest point of a dip in a Hanle curve. The solid curves are drawn for clarity. The inset in (a) shows the excitation protocol for the measured Hanle-curves. The curves were obtained with sample #900 under excitation at 1.47 eV, detected at 1.34 eV at temperature *T*=1.8 K [168].

The excitation protocol, shown in the inset of Figure 4-2(a), consists of an excitation time t_{exc}=50 ms that is interrupted by a dark time. The excitation time remains constant for every measurement, while the dark time is varied from $t_{\mathrm{d}} = 20\ \mu\mathrm{s}$ to $t_{\mathrm{d}} = 50\ \mathrm{ms}$. The degree of polarization was measured as a function of the dark time. Accumulation of the signal takes place at the first ms of the excitation. Figure 4-2(a) shows the Hanle-curves obtained applying four different dark times. The shorter the dark time, the more the curve obtained resembles the Hanle-curve under CW-laser excitation. An increase in dark time smoothes out the W-shape and reduces the width of the Hanle-curve. Dark times that exceed $\sim 50\ \mathrm{ms}$ have no further effect on the Hanle-curve. It should be noted that an increase of the dark time causes two opposite effects on the Hanle-curve depending on the position of the external magnetic field $\boldsymbol{B}_{\mathrm{x}}$. For $\boldsymbol{B}_{\mathrm{x}} > \sim 20\ \mathrm{mT}$ an increase of the dark time leads to a decrease of the polarization degree. For $\boldsymbol{B}_{\mathrm{x}} < \sim 20\ \mathrm{mT}$ an increase of the dark time leads to an increase of the polarization degree.

4.1.1 Longitudinal and transverse component of nuclear polarization

Section 4.1 has shown that the dynamics of nuclear polarization depend on the magnitude of $\boldsymbol{B}_{\mathrm{x}}$. It shows also that the effect of nuclear polarization leads to a decrease of A_{NCP} for small values of $|\boldsymbol{B}_{\mathrm{x}}| \approx 20\ \mathrm{mT}$, but for larger $|\boldsymbol{B}_{\mathrm{x}}|$ a nuclear polarization leads to an increase of A_{NCP}. Such observations give rise to the assumption that polarized nuclei could consist of two sub-ensembles. This section will present an analysis of experimental data which separates the two ensembles of nuclear polarization and identifies them as the longitudinal and transversal component of nuclear polarization (relative to the externally applied

magnetic field $\boldsymbol{B}_{\mathrm{x}}$). The following phenomenological model will include also the contributions of nuclear spin fluctuations on the Hanle effect, which is not the case in other publications [123, 84, 146].

This model is validated both by the experimental data showing that the nuclear spin fluctuation field is independent of the applied field $\boldsymbol{B}_{\mathrm{x}}$ and by good quantitative agreement with results of other studies [147, 148]. Using this model to analyze experimental results, detailed information about the rise and decay times of each component of nuclear polarization in quantum dots in a transverse magnetic field (relative to the optical axis) were obtained. The rise and decay times of the component parallel to the applied field were found to be almost equal (approximately 5 ms). However, the dynamics of the transverse component are much more complicated: the corresponding rise and decay times differ widely and have opposite dependence on magnetic field strength. Furthermore, the magnitude of the transverse component created by continuous wave (CW) pumping significantly increases with applied field strength. This unexpected behavior of nuclear polarization is attributed to nuclear spin relaxation via interaction with photo excited carriers. Information on the behavior of the transverse component $\boldsymbol{B}_{\mathrm{DNP}\perp}$ of the nuclear field can be extracted by analyzing the width of the Hanle-curve. It is clear from Figure 4-1 and Figure **4-2** that the curve width reaches a maximum under CW pumping by a beam of constant circular polarization and decreases with increasing dark time when the pump beam is modulated. Its large width has been attributed to the formation of a transverse component $\boldsymbol{B}_{\mathrm{DNP}\perp}$ of the nuclear field, stabilized by quadrupole splitting of nuclear spin states along the optical axis [149, 85]. The longitudinal component $\boldsymbol{B}_{\mathrm{DNP}\parallel}$ plays no significant role in strong applied magnetic fields [123, 150]. Therefore, the dynamics of $\boldsymbol{B}_{\mathrm{DNP}\parallel}$ and $\boldsymbol{B}_{\mathrm{DNP}\perp}$ can be inferred separately from the behavior of electron spin polarization in weak and strong fields, respectively. Accordingly, in order to analyze experimental data, expressions are required that relate the degree of electron spin polarization to the magnitudes of the corresponding DNP components. To derive expressions for nuclear spin components, it can reasonably be assumed that the only time invariant component of the electron spin is its projection on $\boldsymbol{B}_{\mathrm{tot}}^{\mathrm{e}}$ because of its high precession frequency. The measured degree of luminescence polarization scales linearly with the invariant spin projection on the viewing direction, as illustrated by the following equation:

$$\boldsymbol{S}_{\mathrm{z}} = \boldsymbol{S}_0 \cos^2\theta = \boldsymbol{S}_0 \left(\frac{B_{\mathrm{tot,z}}^{e}}{B_{\mathrm{tot}}^{e}} \right)^2 \tag{4.1}$$

In this equation, $\boldsymbol{S}_0$ quantifies the degree of optically induced spin orientation and θ is the angle between the viewing direction and the total field $\boldsymbol{B}_{\mathrm{tot}}^{\mathrm{e}} = \boldsymbol{B}_{\mathrm{x}} + \boldsymbol{B}_{\mathrm{N}} + \boldsymbol{B}_{\mathrm{NF}}$, which included also the nuclear fluctuation field [37]. In the absence of regular fields $\boldsymbol{B}_{\mathrm{x}}$ and $\boldsymbol{B}_{\mathrm{N}}$, electron spin dynamics are completely determined by nuclear spin fluctuations. A magnetic field applied perpendicular to the optical axis (along the *x*-axis) substantially changes the

time averaged electron spin polarization. The calculated field dependence of $\boldsymbol{S}_{\mathrm{z}}$ can be described by a bellshaped curve accurately fitted by eq.(4.1) with

$$\left(B^{\mathrm{e}}_{\mathrm{tot,z}}\right)^2 = \langle B^2_{\mathrm{NF,z}}\rangle \tag{4.2}$$

where $\langle \boldsymbol{B}_{\mathrm{NF,z}}\rangle$ is the ensemble average of the nuclear spin fluctuation field *z* component squared and

$$(B^{\mathrm{e}}_{\mathrm{tot}})^2 = B^2_{\mathrm{x}} + \langle B^2_{\mathrm{NF}}\rangle \tag{4.3}$$

with $\langle \boldsymbol{B}^2_{\mathrm{NF}}\rangle = \langle \boldsymbol{B}^2_{\mathrm{NF,x}}\rangle + \langle \boldsymbol{B}^2_{\mathrm{NF,y}}\rangle + \langle \boldsymbol{B}^2_{\mathrm{NF,z}}\rangle$. Thus, the mean ratio approximated by the ratio of means in (4.1),

$$\langle S_{\mathrm{z}}\rangle \approx S_0 \frac{\langle \left(B^{\mathrm{e}}_{\mathrm{tot,z}}\right)^2\rangle}{\langle (B^{\mathrm{e}}_{\mathrm{tot}})^2\rangle} \tag{4.4}$$

yields a satisfactory result under conditions specified in the above. Approximation (4.4) holds in the presence of a regular field $\boldsymbol{B}_{\mathrm{N}}$, with a periodically time- varying numerator:

$$B_{\mathrm{tot,z}} = B_{\mathrm{N}\perp}\cos\omega t \tag{4.5}$$

where $B_{\mathrm{N}\perp}$ is the component of the total nuclear field perpendicular to the applied field and ω_N is the frequency of nuclear spin precession induced by the applied field. The electron pumping rate was higher than the nuclear precession frequency in the entire range of applied magnetic field magnitudes used in the experiments described here. Therefore, the numerator in eq.(4.4) can be represented as

$$\langle \left(B^{\mathrm{e}}_{\mathrm{tot,z}}\right)^2\rangle = \left(B^2_{\mathrm{DNP}\perp} + \langle B^2_{\mathrm{NF}\perp}\rangle\right)\langle \cos^2\omega t\rangle \tag{4.6}$$

$$= 0.5(B^2_{DNP\perp} + \langle B^2_{NF\perp}\rangle)$$

where the nuclear fluctuation field is assumed to be statistically isotropic.

$$\langle B^2_{\mathrm{NF}}\rangle = \langle B^2_{\mathrm{NF}\parallel}\rangle + \langle B^2_{\mathrm{NF}\perp}\rangle = 3\langle B^2_{\mathrm{NF}\parallel}\rangle \tag{4.7}$$

Analogously, the ensemble average of the total field squared, expressed by the denominator in (4.4), can be expressed as

$$\langle (B^{\mathrm{e}}_{\mathrm{tot}})^2\rangle = (B_{\mathrm{x}} + B_{\mathrm{DNP}\parallel})^2 + \langle B^2_{\mathrm{NF}\parallel}\rangle + B^2_{\mathrm{DNP}\perp} + \langle B^2_{\mathrm{NF}\perp}\rangle \tag{4.8}$$

In summary, the degree of electron spin polarization can be represented by the general expression

$$\rho = \frac{\langle S_z \rangle}{S_0} = \frac{0.5(B_{DNP\perp}^2 + \langle B_{NF\perp}^2 \rangle)}{(B_x + B_{DNP\parallel})^2 + B_{DNP\perp}^2 + \langle B_{NF}^2 \rangle} \tag{4.9}$$

Experimental data can be analyzed by simplifying expression (4.9) in two special cases depending on the magnitude of $\boldsymbol{B}_x$. According to [123], the longitudinal component $\boldsymbol{B}_{DNP\parallel}$ of the nuclear field only appears in the W-profile region of the Hanle-curve, where the applied field is negligible compared to the nuclear spin fluctuation field [37]. Then, it holds for this region that

$$\rho \approx \frac{0.5(B_{DNP\perp}^2 + \langle B_{NF\perp}^2 \rangle)}{B_{DNP\parallel}^2 + B_{DNP\perp}^2 + 3\langle B_{NF\parallel}^2 \rangle}. \tag{4.10}$$

In strong applied magnetic fields (where $B_{DNP\parallel} \to 0$), the degree of polarization becomes

$$\rho \approx \frac{0.5(B_{DNP\perp}^2 + \langle B_{NF\perp}^2 \rangle)}{B_x^2 + B_{DNP\perp}^2 + 3\langle B_{NF\parallel}^2 \rangle}. \tag{4.11}$$

Thus, the time dependence of ρ in strong and weak magnetic fields is examined to determine the respective kinetics of the longitudinal and transverse components of nuclear polarization. The analysis of time dependent nuclear polarization is based on the assumption that the increase in each component of nuclear polarization after the start of pumping and its decay during the dark time can be described by the expressions

$$y = B_{DNP\perp,(\parallel)}[1 - \exp(-t/\tau_b)] \tag{4.12}$$

$$y = B_{DNP\perp,(\parallel)}\exp(-t/\tau_d) \tag{4.13}$$

where τ_b and τ_d is the corresponding characteristic buildup and decay time, respectively. In the case of a weak magnetic field, the numerator and denominator in (4.10) are divided by $\langle B_{NF\parallel}^2 \rangle$. Then the following parameters are introduced:

$$a^2 = \frac{B_{DNP\perp}^2}{\langle B_{NF\parallel}^2 \rangle} \tag{4.14}$$

$$c^2 = \frac{B_{DNP\parallel}^2}{\langle B_{NF\parallel}^2 \rangle}. \tag{4.15}$$

These equations serve to find respective expressions describing the rise and decay of the longitudinal component of nuclear polarization as follows:

$$\rho \approx \frac{0.5a^2 + 1}{c^2(1 - \mathrm{e}^{-t/\tau_\mathrm{b}})^2 + a^2 + 3} \tag{4.16}$$

$$\rho \approx \frac{0.5a^2 + 1}{c^2\mathrm{e}^{-2t/\tau_\mathrm{d}} + a^2 + 3}\,. \tag{4.17}$$

The transverse component of nuclear polarization almost vanishes in weak magnetic fields, so that the parameter *a* can be neglected in analysis of experimental data. For this reason the time dependence of this parameter is omitted in the formulas above. Expression (4.11), valid for strong applied magnetic fields, can be rewritten analogously by introducing

$$\rho \approx \frac{0.5\left(1 - \mathrm{e}^{-t/\tau_\mathrm{b}}\right)^2 + c'^2}{a'^2 + (1 - \mathrm{e}^{-t/\tau_\mathrm{b}})^2 + 3c'^2} \tag{4.18}$$

$$\rho \approx \frac{0.5e^{-2t/\tau_\mathrm{d}} + \mathrm{c}'^2}{a'^2 + e^{-2t/\tau_\mathrm{d}} + 3\mathrm{c}'^2} \tag{4.19}$$

to describe the rise and decay of the transverse component of nuclear polarization, respectively. Thereby is $a'^2 = B_\mathrm{x}^2/B_{\mathrm{DNP}\perp}^2$ and $c'^2 = \langle B_{\mathrm{NF}\parallel}^2\rangle/B_{\mathrm{DNP}\perp}^2$. In summary, using the expressions derived above, it is possible to fit the measured time- dependent degrees of polarization to evaluate nuclear spin relaxation times τ, as well as effective nuclear spin fluctuation fields and dynamic nuclear polarization.

4.1.2 Build up dynamics of nuclear polarization

Figure 4-3 and Figure 4-4 show the results of an analysis of the time-dependent Hanle-curves in Figure 4-1, measured after the start of optical pumping. The values of ρ are refined by taking into account luminescence depolarization due to contributions from neutral quantum dots.

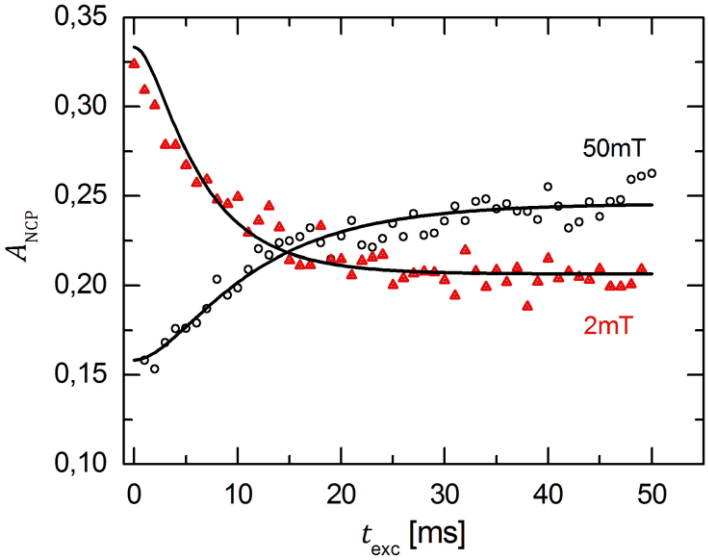

Figure 4-3 Time dependence of A_{NCP} during an excitation pulse of 50 ms duration that is interrupted by a dark time of $t_{\mathrm{d}} = 50$ ms. The excitation protocol is given in Figure 4-2. Symbols represent experimental results for $\boldsymbol{B}_{\mathrm{x}}$ = 2 mT and 50 mT; the solid curves are approximations given by eqs. (4.16) and (4.18). The curves were obtained with sample #900 under excitation at 1.47 eV, detected at 1.34 eV at temperature $T = 1.8$ K [168].

The time-dependent degree of polarization determined from experimental data can be fitted by eq. (4.16) only if the transverse component of the nuclear field is sufficiently weak, $B^2_{\mathrm{DNP}\perp} \ll \langle B^2_{\mathrm{NF}} \rangle$. This is the case for a low field condition, $B_{\mathrm{x}} < 20$ mT. Using the resulting approximation, the characteristic rise time for $B^2_{\mathrm{DNP}\parallel}$ is estimated to be $|\tau_{\parallel}| = 6$ ms, and the parameter $c \approx 1.5$ (ref. to eq.. (4.15)). The behavior of longitudinal polarization is relatively simple. After the start of optical pumping, this component increases with a characteristic time of approximately 6 ms to a limit magnitude corresponding to an effective nuclear field of 30 mT to 40 mT. After the end of pumping, the longitudinal component decays over a similar time scale. Under high field conditions ($B_{\mathrm{x}} \geq 20$ mT), where the transverse component of nuclear polarization plays the dominant role, the measured data can be fitted by function (4.18). As an example for the low and high field regime, Figure 4-3 shows the dynamics of A_{NCP} at 2 mT and 50 mT. The parameters a' and c' calculated by fitting the polarization history for each applied magnetic field strength were then used to determine the limit magnitude of the transverse component of nuclear polarization,

$$B_{\mathrm{DNP}\perp,\mathrm{L}} = B_{\mathrm{x}}/a' \tag{4.20}$$

the RMS effective nuclear spin fluctuation field,

$$B_{\mathrm{NF}\parallel,\mathrm{L}} \equiv \sqrt{\langle B^2_{\mathrm{NF}\parallel} \rangle} = \frac{c'}{a'} B_{\mathrm{x}} \tag{4.21}$$

and their dependence on the magnetic field. Figure 4-4(a) shows $B_{\mathrm{DNP}\perp,\mathrm{L}}$ and $B_{\mathrm{NF}\parallel,\mathrm{L}}$ as functions of the applied magnetic field. It is clear that the limit magnitude $B_{\mathrm{DNP}\perp,\mathrm{L}}$ of the transverse component of nuclear polarization increases approximately from 10 mT to 50 mT with an applied field between 20 mT and 100 mT, whereas the effective nuclear spin

fluctuation field $B_{\mathrm{NF}\parallel,\mathrm{L}}$ remains almost constant at around 25 mT irrespective of the applied field strength. This value is in good agreement with data reported in [147],

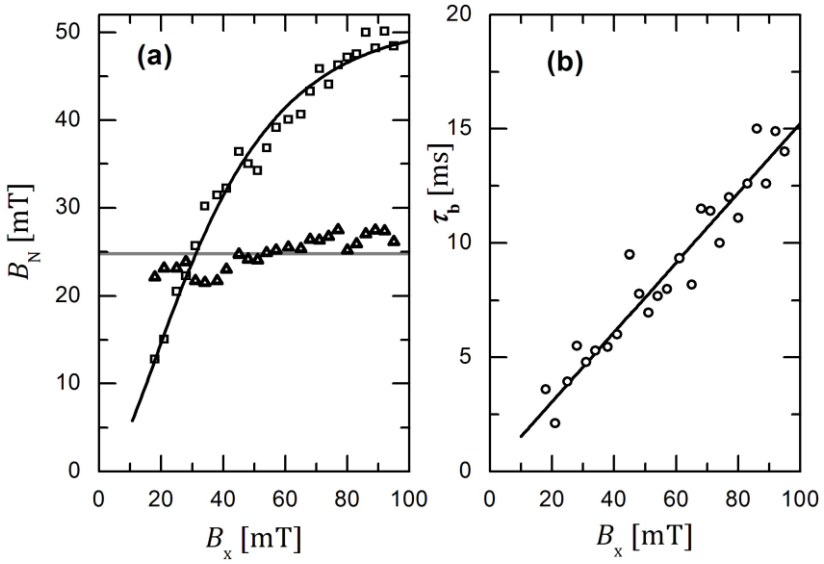

Figure 4-4 (a) Limit magnitudes of the transverse nuclear field component $B_{\mathrm{DNP}\perp,\mathrm{L}}$ (rectangles) and the nuclear spin fluctuation field $B_{\mathrm{NF}\parallel,\mathrm{L}}$ (triangles) vs. applied field, obtained by analyzing kinetics of spin polarization after the start of pumping (ref. to Figure 4-1). (b) Field dependence of the buildup time τ_{b} of the transverse nuclear field $B_{\mathrm{DNP}\perp}$ (circles) component. The solid curves are drawn for clarity. The curves were obtained with sample #900 under excitation at 1.47 eV, detected at 1.34 eV at temperature *T*=1.8 K [168].

where the RMS nuclear spin fluctuation field was estimated at approximately 20 mT for quantum dots of a similar type. Using this value and *c* ≈ 1.5 as obtained above, the maximum parallel nuclear field can be calculated as follows: $B_{\mathrm{DNP}\parallel,\mathrm{L}} \approx 40\ \mathrm{mT}$. Figure 4-4(b) shows the buildup time τ_{b} of the transverse component of nuclear polarization. It demonstrates that the buildup time increases linearly from approximately 2.5 ms to 15 ms with an applied field between 20 mT and 100 mT. The transverse nuclear field component $B_{\mathrm{DNP}\perp}$ is identified as a polarization of nuclear spin states $I \geq 3/2$ (detailed discussion in sec. 4.1.3). Such nuclear spin states are more strongly influenced by an electric field gradient than spin states $I = 1/2$. As a consequence, the Zeeman splitting is like in Figure 4-43 and nuclear spin states $I \geq 3/2$ do not split in small external magnetic fields. Without a splitting in energy of these nuclear states a difference in occupation of the Zeeman levels is not possible, which also disables a polarization of these nuclear states. This behavior is illustrated in Figure 4-4(a). An extension of the solid line in Figure 4-4(a) shows that $B_{\mathrm{DNP}\perp,\mathrm{L}} = 0\ \mathrm{mT}$ is reached at $B_{\mathrm{x}} \approx 5\ \mathrm{mT}$. This means that such small fields of B_{x} have a negligibly small influence on nuclear spin states $I \geq 3/2$ in comparison to the interaction of the quadrupole moment of these states and the electric field gradient. In Figure 4-4(b) an extrapolation of the solid line leads to a buildup time $\tau_{\mathrm{b}} = 0\ \mathrm{s}$ at $B_{\mathrm{x}} = 0\ \mathrm{mT}$. The correct interpretation is that at $B_{\mathrm{x}} = 0\ \mathrm{mT}$ the only magnetic field that could enable a Zeeman splitting of the nuclear spin states is the Knight field $\boldsymbol{B}_{\mathrm{e}}$. But the Knight field is only $\boldsymbol{B}_{\mathrm{e}} \approx 1\ \mathrm{mT}$, so it is not large enough to split nuclear spin states $I \geq 3/2$. The buildup time $\tau_{\mathrm{b}} = 0\ \mathrm{s}$ means that a buildup of nuclear polarization is not possible. The solid lines in Figure 4-4(a), (b) are not drawn in the

range of small B_x because an experimental proof of the behavior of $B_{DNP\perp,L}$ and $B_{DNP\perp}$ is not possible due to the fact that in such small B_x the magnitude of $B_{NF\parallel}$ and $B_{DNP\parallel}$ is larger than $B_{DNP\perp,L}$ and overlays the effect of $B_{DNP\perp,L}$.

4.1.3 Decay of nuclear polarization

An analogous procedure was used to analyze the shape of the Hanle-curve as a function of dark time. Experimental data was converted into spin polarization kinetics for several values of the applied magnetic field strength (as in Figure 4-3), and the resulting curves were fitted by eqs.(4.17) and (4.19). The curves in Figure 4-5 are examples of such fits.

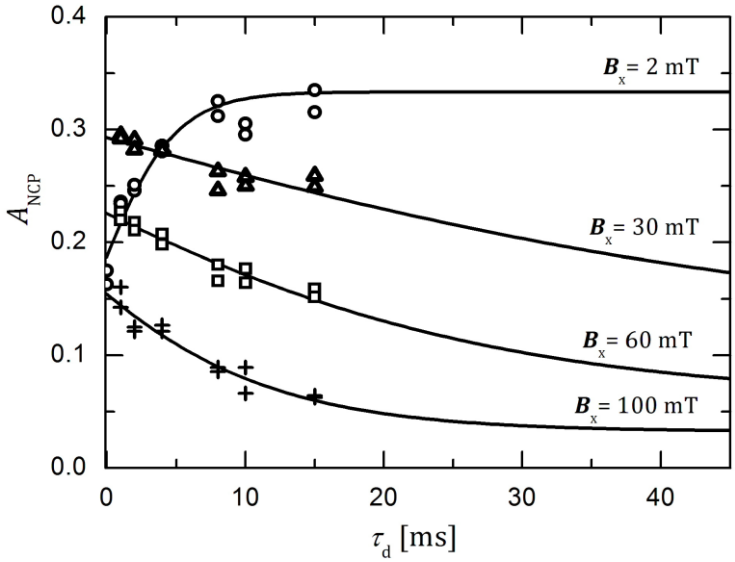

Figure 4-5 Time evolution of A_{NCP} in dependence of the dark time. The different symbols represent experimental data at several values of B_x. The corresponding value of B_x is written at each curve (solid line) which is an approximation given by eq. (4.17) and (4.19). The curves were obtained with sample #900 under excitation at 1.47 eV, detected at 1.34 eV at temperature $T = 1.8$ K [168].

The fitting parameters were used to evaluate the initial longitudinal and transverse nuclear fields, as well as the corresponding decay times. The decay time of the longitudinal component calculated by using the data for $B_x = 2$ mT was found to be $\tau_d \approx 5.5$ ms , which is close to the corresponding rise time reported above. However, the decay time of the transverse component of nuclear polarization differs significantly from its rise time. Moreover, its time variation in an applied magnetic field exhibits an opposite trend: whereas the rise time increases with field strength (ref. to Figure 4-4(b)), the decay time rapidly decreases (ref. to Figure 4-6(b)). Accordingly, these times are approximately equal in strong magnetic fields but differ by a factor of several tenths at B_x= 20 mT.

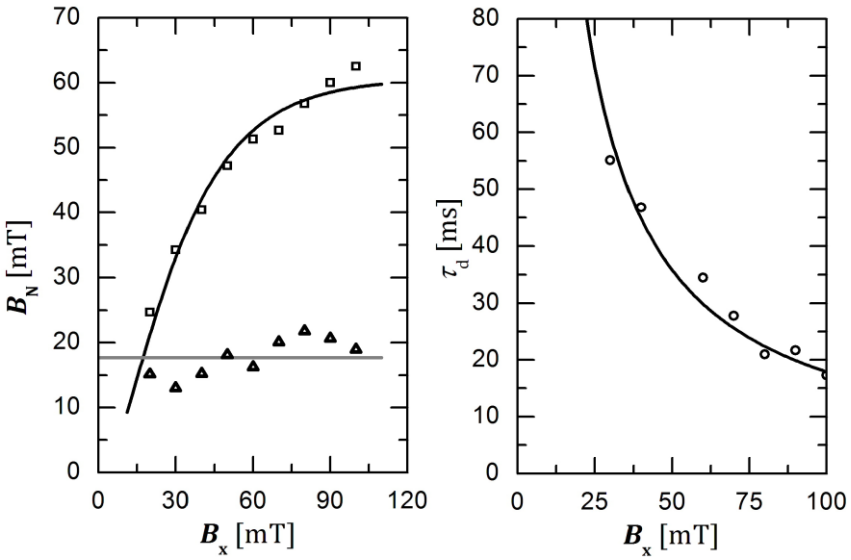

Figure 4-6 (a) Field dependence of the initial magnitude $B_{\mathrm{DNP}\perp}$ (rectangles) of the transverse nuclear field and the nuclear spin fluctuation field $\boldsymbol{B}_{\mathrm{NF}}$ (triangles), obtained by analyzing kinetics of spin polarization after the end of pumping. (b) Field dependence of the $B_{\mathrm{DNP}\perp}$ (circles) decay time. The solid curves are drawn for clarity. The curves were obtained with sample #900 under excitation at 1.47 eV, detected at 1.34 eV at temperature $T = 1.8$ K [168].

The origin of this behavior is unclear up to now. But the reader should be reminded about a relaxation mechanism already given in the literature [40], where the presence of a single electron in a quantum dot is shown to increase the rate of nuclear spin relaxation by more than two orders of magnitude. In this case, the single electron is the resident electron of the used quantum dot structures. During the dark time the single resident electron is exposed to the nuclear spin system, which is in a different situation than during the excitation. It is possible that this mechanism depends on the precession frequency of the nuclei, therefore on the external field B_{x}.

Remarkably, despite the difference in behavior between decay times, both the limit magnitudes of the DNP components and their variation with magnetic field strength in experiments on nuclear polarization decay are in good agreement with those determined by measuring nuclear polarization buildup (compare Figure 4-4(a) and Figure 4-6(a)). A slight difference between nuclear field magnitudes measured in experiments on polarization buildup and decay should rather be attributed to a minor difference in optical excitation intensity (which was not intended) between experiments of these two types. Standard models of nuclear polarization buildup are generally based on the classical model of angular momentum precession in isotropic space [123]. The condition of spatial isotropy is violated in the quantum dots examined in this study because nuclei are affected by the field gradient due to the strain resulting from a mismatch between the lattice constants of the quantum dots and barrier layers and the exchange of nuclei due to the annealing process. Up to date theoretical approaches of optically induced nuclear spin polarization try to involve the quadrupole interactions, but there are still many unresolved problems [151]. In the experiments considered in this thesis all nuclei of the sample have a quadrupole moment

due to a nuclear spin of $I = 3/2$ or higher. The electric field gradient (ref. to sec. 2.1.2) splits nuclei, which have nonzero quadrupole moments, into Kramers doublets $|\pm 1/2\rangle$, $|\pm 3/2\rangle$… etc. In an applied magnetic field, the Zeeman splitting in the doublets strongly depends on the relative orientation of the gradient axis and the magnetic field vector. This dependence can be described phenomenologically by introducing an anisotropic *g*-factor [152]. The anisotropy associated with the doublets $|\pm 1/2\rangle$ is relatively weak: the difference between the *g*-factor components parallel and perpendicular to the gradient axis is not greater than a factor of 2 [82, 153]. Dynamics of these states should not be too different from the nuclear spin dynamics invoked to explain the W-profile of the Hanle-curve [84]. In the present study, one is naturally led to hypothesize that orientation of these particular states is responsible for the buildup of the component of nuclear polarization parallel to the applied field manifesting itself by the development of a W-profile. This hypothesis is consistent with the relatively simple dynamical pattern of the longitudinal component of nuclear polarization observed in our experiments. The *g*-factor anisotropy associated with the states, $|\pm 3/2\rangle$, $|\pm 5/2\rangle$...etc., is much stronger than with the doublets $|\pm 1/2\rangle$, as demonstrated in relatively weak magnetic fields. In a magnetic field parallel to the gradient axis, the splitting of these states linearly increases with field strength and the corresponding g-factor is similar to that in the absence of a gradient. This is not the case in the presented measurements, because the structure growth direction is perpendicular to the external magnetic field B_{x}, while the strain, which is the main reason for the electric field gradient, is directed along the growth direction. In this case the magnetic field is perpendicular to the electric field gradient, which results in a highly nonlinear function of the g-factor depending on the external magnetic field B_{x}. This means that the splitting of the $|\pm 3/2\rangle$, $|\pm 5/2\rangle$...etc. nuclear spin states almost vanishes in fields on the order of a few millitesla [82, 153]. In terms of the classical model, this means almost no precession of angular momenta associated with these states in a field of this kind. Suppression of precession impedes nuclear spin relaxation, which is generally attributed to local magnetic field effects (e.g., ref. to [154]). In effect, the transverse component of polarization of the nuclear states split off by quadrupole interactions can be stabilized to some degree in weak magnetic fields [149, 85]. A superlinear increase in splitting of these states with field strength enhances the probability of spin relaxation. The ensuing higher relaxation rate may be responsible for the shorter $B_{\mathrm{DNP}\perp}$ decay times observed with increasing magnetic field strength in our experiments (ref. to Figure 4-6(b)).

4.2 Effect of nuclear fluctuation field $\mathbf{B_{NF}}$ on the Hanle-curve

The aim of the experiments presented in the following chapter is to analyze the behavior of the W-shape of the Hanle-curve after excitation with a CW-laser for different constant magnetic fields B_{z} directed along the optical axis (z-axis).

B_z is applied by a pair of Helmholtz coils that can be tuned in the range of $-3\ \mathrm{mT} \leq B_z \leq +3\ \mathrm{mT}$. Sample #980 is studied in the range of $-20\ \mathrm{mT} \leq B_x \leq +20\ \mathrm{mT}$. Figure 4-7 shows an overview of the effect of B_z on a larger scale of B_x. Each curve shows the pronounced W-structure consisting of the narrow central peak and two maxima positioned symmetrically in relation to the peak. The HWHM of the central peak without the additional magnetic field B_z is less than 1 mT. In comparison to a Hanle-curve obtained without B_z, a negative value $B_z = -3\ \mathrm{mT}$ leads to an increase of A_{NCP} all over the curve. In contrast, a positive value $B_z = +3\ \mathrm{mT}$ leads to a decrease of A_{NCP}.

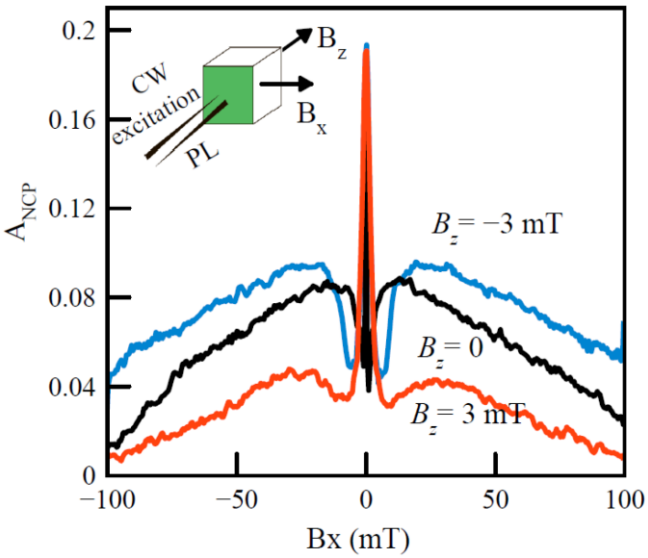

Figure 4-7 Overall shape of Hanle curves measured at different longitudinal magnetic fields B_z indicated at each curve. The inset shows the configuration of the experiment. The curves were obtained with sample #980 under excitation at 1.49 eV, detected at 1.42 eV at temperature $T = 1.8\ \mathrm{K}$ [155].

With focus on the W-structure of the Hanle-curve, an increase of B_z leads to an increase of the width of the central-peak to approximately 4 mT, irrespective of the sign of B_z. The experiment shows that application of a positive B_z is accompanied by a monotonous increase of the width of the central peak and of the dips near the peak. The depth of the dips remains almost unchanged. At negative B_z, the behavior of the dips is not monotonous. The change of B_z from $0\ \mathrm{mT}$ to $-1\ \mathrm{mT}$ results in almost total disappearance of the dips without noticeable change of their width. A further increase of the B_z value to $-2\ \mathrm{mT}$ leads to the increase of both depth and width of the dips.

4.2.1 Introduction to standard cooling model

The analysis of experimental data has confirmed the prediction of ref. [37] about the significant influence of nuclear spin fluctuations on the electron spin orientation due to strong localization of the electron in QDs. The observed behavior is considerably different

from that in extended semiconductor alloys studied in many works (ref. [123]). In extended semiconductor alloys the electron density is spread out over a huge number of nuclei and the effect of the nuclear spin fluctuations (NSF), as a rule, is negligibly small. The experimental Hanle-curves are compared with the results of calculations using two models, one including NSF and the other one taking into account only mean Overhauser fields. In both theories, the mean Overhauser field has been calculated within the spin temperature approach.

The concept of a spin temperature is used since the late 1940's [156] and has been adapted to many different systems [157, 80, 158, 159, 160, 161, 162, 163]. Lowering the spin temperature corresponds to a considerable magnetization along the magnetic field or opposite to it (depending on the sign of the spin temperature), which gives rise to the Overhauser field acting on the electron spin. The Overhauser field is parallel or antiparallel to the nuclear spin, depending on the sign of the electron g-factor. In particular, it is antiparallel for the negative sign of g_e, as in our case. The total magnetic field $\boldsymbol{B}_{\mathrm{tot}}^{\mathrm{N}}$ that acts on the nuclei is the sum of the external field $\boldsymbol{B}_0$ and the Knight field $\boldsymbol{B}_{\mathrm{e}}$. If $\boldsymbol{B}_0$ is strictly perpendicular to the optical axis (like in the Voigt-geometry used in this experiments), then the nuclear spin cooling occurs only due to the Knight field. Besides, the electron spin dynamics is determined by the total magnetic field $\boldsymbol{B}_{\mathrm{tot}}^{\mathrm{e}}$ that acts on the electron, which is the sum of $\boldsymbol{B}_0$ and $\boldsymbol{B}_{\mathrm{N}}$. Such an interdependency of the system leads to coupled equations [123].

$$\boldsymbol{S} - \boldsymbol{S}_0 = (\boldsymbol{B}_{\mathrm{tot}}^{\mathrm{e}} \cdot \boldsymbol{S})/B_{1/2} \tag{4.22}$$

$$\boldsymbol{B}_{\mathrm{N}} = \boldsymbol{B}_{\mathrm{tot}}^{\mathrm{N}} \eta b_{\mathrm{N}} \frac{(I+1)\mu_{\mathrm{B}}}{3} = \boldsymbol{B}_{\mathrm{tot}}^{\mathrm{N}} \frac{b_N\left(\boldsymbol{B}_{\mathrm{tot}}^{\mathrm{N}} \cdot S_{\parallel}\right)}{\left(B_{\mathrm{tot}}^{\mathrm{N}}\right)^2 + \xi B_{\mathrm{L}}^2} \frac{4I(I+1)}{3} \tag{4.23}$$

Here, $B_{1/2}$ is the half width at half maximum (HWHM) of the Hanle-curve in the absence of the nuclear field. g_e, μ_{B} and T_{e} are the electron g-factor, the Bohr magneton, and the electron spin lifetime, respectively. η is the reciprocal temperature of the nuclear spin system, and parameter b_{N} is the effective field of totally polarized nuclei affecting the electron spin. The magnitude of b_{N} is determined by the properties of the particular electron-nuclear spin system and should not depend on external conditions. The term ξB_{L}^2 describes the interaction between nuclear spins causing the relaxation of nuclear polarization, where $\boldsymbol{B}_{\mathrm{L}}$ is the local field, resulting from the next neighbouring nuclei acting on other nuclei. The solution of these equations yields a cubic equation for the average projection of the electron spin onto the direction of observation. The equation that applies in case the magnetic field B_{x} is perpendicular to the optical axis is given in ref. [123]. A simple generalization of the equation is possible in case an additional magnetic field B_{z} directed along the optical axis:

$$S_z\left(1+\frac{K^2}{B_{1/2}^2}B_x^2\right)-S_0\left(1+\frac{K^2}{B_{1/2}^2}B_z^2\right)=0 \qquad (4.24)$$

$$K=1+\frac{S_0B_z+b_eS_0S_z}{B_x^2+2b_eS_0B_z+b_e^2S_0S_z+\xi B_L^2} \qquad (4.25)$$

S_0 is the initial electron spin orientation created by excitation, and S_z is the projection of the electron spin on the z-axis averaged over time.

4.2.2 Standard cooling model

To model the experimentally measured Hanle-curve, the eq. (4.22) is solved numerically and S_z is obtained as a function of the transverse magnetic field B_x for different values of the longitudinal magnetic field in the range from $3\ \mathrm{mT} \le B_z \le +3\ \mathrm{mT}$. The following values of the other parameters were used in the calculations: $S_0 = 1/2$, $B_{1/2} = 60\ \mathrm{mT}$, $B_L = 0.3\ \mathrm{mT}$, and $b_e = 2\ \mathrm{mT}$. The value of $B_{1/2}$ extracted from the measurement corresponds to the electron spin life time T_e of the order of 10^{-10} s, which is several orders of magnitude smaller than the real value in the structures of this type (ref. to [164]). The difference of the $B_{1/2}$ to similar structures appears due to a build up of the Overhauser field (ref. to sec. 2.1.3) and is a sign of nuclear polarization. Examples of the calculated dependences are shown in Figure 4-8.

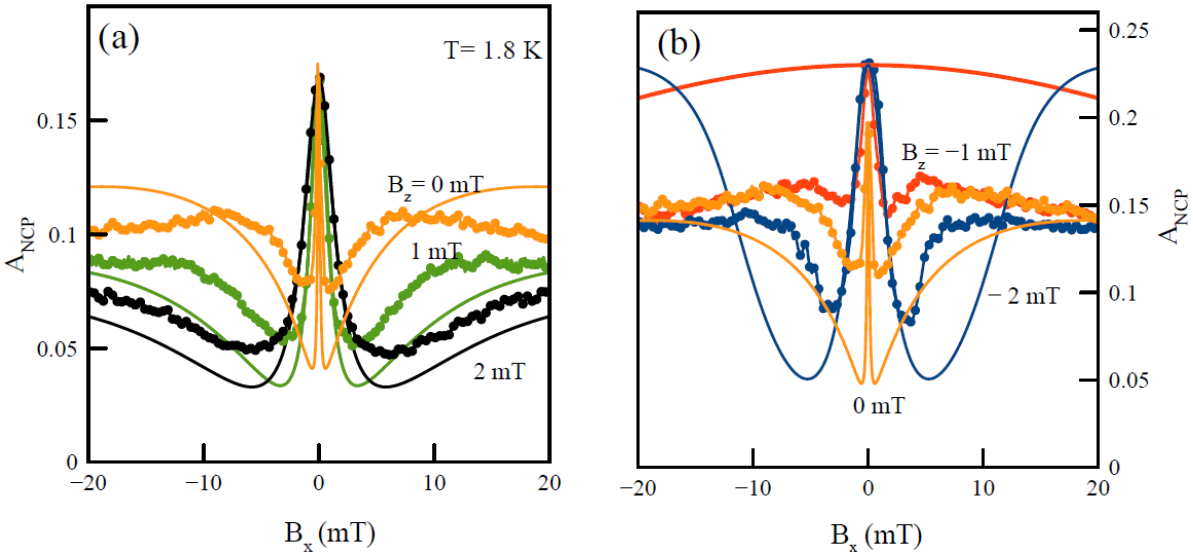

Figure 4-8 Comparison of the calculated curves according to the standard cooling model (solid lines) with the measured data for (a) positive and (b) negative longitudinal external field B_z. The corresponding values of B_z are given for each curve. The curves were obtained with sample #980 under excitation at 1.49 eV, detected at 1.42 eV at temperature $T = 1.8$ K [155].

However, they only partially reproduce the behavior of the measured Hanle-curves. For positive B_z (ref. to Figure 4-8(a)) the calculated curve roughly follows the measured Hanle-curve and for negative B_z the calculated curve is completely different from the measured Hanle-curve. To find a reason for the discrepancy between the calculated and the measured curves it is necessary to pay attention to the directions of the magnetic fields present. B_z is codirected to the Knight field due to the helicity of excitation used in our experiments, which determines the spin direction of the excited electron. The analysis also shows that in this case the nuclear field B_N is codirected to the external magnetic field and thus "amplifies" it. This amplification results in a gradual decrease of spin polarization and, correspondingly, of PL polarization beyond the central peak with rising $|B_z|$, as seen both from the calculations and from the measured curves. When B_z is negative, the total field $\boldsymbol{B}^e_{tot}$ has a component that is antiparallel ($B^e_{tot,-z}$) to the Knight field. When this antiparallel component reaches the magnitude of the Knight field it compensates it (according to ref. [123, 84]) and nuclear spin cooling is not possible in this case. This should result in the disappearance of the W-structure, as it is indeed seen in Figure 4-8(b) for the Hanle-curve calculated for $B_z = 1$ mT. At more negative B_z, the W-structure reappears, but the additional maxima run away from the central peak with increasing amplitude of B_z, maintaining the same amplitude as the central peak. This behavior of the calculated Hanle-curves is explained by the fact that in this case the nuclear field $\boldsymbol{B}_N$ is directed against the total effective magnetic field $\boldsymbol{B}^N_{tot}$ affecting the nuclei. The x component of the nuclear field $B_{N,x}$ is compensated by the external transverse magnetic field B_x at some magnitude of B_x, giving rise to the additional maxima. The efficiency of the nuclear-spin pumping increases with the increase of $|B_z|$. As a result, $B_{N,x}$ increases, and the positions of the compensation points where $B_{N,x} + B_x = 0$ are shifted to larger $|B_x|$.

These numerical results, however, are in strong contradiction to our experimental observations (ref. to Figure 4-8). The central peak of the measured Hanle-curves is higher than the other parts of the Hanle-curve at any negative B_z. At this point it is important to stress that the disagreement between the theory and the experiment cannot be eliminated for any set of values of the adjustable parameters. Therefore this contradiction is of principal importance and indicates that the model of mean nuclear field ignores some mechanism causing depolarization of the electron spin at a non-zero transverse magnetic field, including points where it is totally compensated by the nuclear field. The discrepancy is evident also from the unrealistically large value of $B_{1/2}$ needed to fit, at least partly, the experimental Hanle-curves within the mean-field model.

4.2.3 Extended cooling model considering nuclear fluctuating field $\mathbf{B_{NF}}$

In contrast to the model presented in sec. 4.2.2 $\boldsymbol{B}_{\mathrm{tot}}^{\mathrm{e}}$ is enhanced by the nuclear fluctuation field $\boldsymbol{B}_{\mathrm{NF}}$ and given by $\boldsymbol{B}_{\mathrm{tot}}^{\mathrm{e}} = \boldsymbol{B}_{\mathrm{N}} + \boldsymbol{B}_{\mathrm{x}} + \boldsymbol{B}_{\mathrm{NF}}$. The origin of the fluctuation field $\boldsymbol{B}_{\mathrm{NF}}$ is the random change of orientation of the unpolarized nuclei. In bulk materials the amount of unpolarized nuclei that interact with the electron is so large that the effect is averaged to zero. But for nanostructures like quantum dots the amount of unpolarized nuclei is so small that on the one hand the effect of each unpolarized nucleus is not compensated by another unpolarized nucleus. On the other hand the magnetic field that appears due to the uncompensated nuclei is so large that the effect on the electron is not negligible (for more details ref. to sec. 2.1.4). The estimates given in refs. [165, 78] for similar QDs show that the average magnitude of the fluctuating nuclear field is in the order of tenths of millitesla. The frequency of the electron spin precession about the field is orders of magnitude larger than the time of relaxation τ_s of the electron spin. Therefore the width of the Hanle-curve is determined by the fluctuating nuclear field rather than by the electron spin relaxation. This allows to fit the experimental curves without using nonrealistic values of τ_s as was done in the previous chapter for the standard cooling model. An effective optical pumping can create a dynamic nuclear polarization, whose magnitude can considerably exceed the nuclear spin fluctuations. If the transverse magnetic field is zero, the effective field of nuclear polarization is directed along the optical axis and is able to suppress the effect of nuclear spin fluctuation (NSF). This results in the increased amplitude of the central peak of the Hanle-curve. In particular, the electron spin polarization at the point of mutual compensation of the external field and the field of nuclear polarization is smaller than the polarization at zero B_x. This qualitative consideration explains the small amplitudes of the additional maxima of the Hanle-curves, which cannot be explained by the standard cooling model. In order to include NSF in the theory, the following facts are used. The buildup time of the nuclear polarization is much longer than the correlation time of the nuclear spin fluctuation, which is, in turn, orders of magnitude longer than the electron spin lifetime. For this reason, the nuclear spin temperature can be calculated using the value of the electron mean spin averaged over possible realizations of the NSF, while each NSF realization can be

considered “frozen” (i.e., the evolution of nuclear spin during the electron spin lifetime can be neglected) [37]. The dependence of the average electron spin polarization on the transverse external magnetic field within this approximation is a bell-like curve, which can be well fitted by a Lorentzian:

$$\rho(B_{\mathrm{x}}) \approx \frac{\langle B_{\mathrm{NF.z}}^2 \rangle}{B^2 + \langle B_{\mathrm{NF}}^2 \rangle} \tag{4.26}$$

Here is $\langle B_{\mathrm{NF}}^2 \rangle = \langle B_{\mathrm{NF,x}}^2 \rangle + \langle B_{\mathrm{NF,y}}^2 \rangle + \langle B_{\mathrm{NF,z}}^2 \rangle$ where $\langle B_{\mathrm{NF},\alpha'}^2 \rangle$ is the squared α’ component (α’ = *x,y,z*) of the NSF averaged over the QD ensemble. Equation ((4.26) has a simple geometrical interpretation. In each QD with realization of a particular fluctuating field $\boldsymbol{B}_{\mathrm{NF}}$, only the projection of the electron spin onto the total field $\boldsymbol{B}_{\mathrm{tot}}^{\mathrm{e}} = \boldsymbol{B}_{\mathrm{x}} + \mathbf{B}_{\mathrm{NF}}$ survives: $S_{\parallel} = S_0 \cos\varphi$, where φ is the angle between the vector $\mathrm{B}_{\mathrm{tot}}^{\mathrm{e}}$ and the z-direction. Some generalization of eq.(4.26) is required to describe the electron spin polarization under the used experimental conditions. We need to take into account the regular nuclear field B_{N} with non-zero components $B_{\mathrm{N,x}}$ and $B_{\mathrm{N,z}}$ created by the dynamic polarization of nuclei. Similar to the standard mean-field model it is assumed for simplicity reasons that the electron density is homogeneously distributed over the nuclei (the so-called box model approximation [166]), which allows to neglect the spatial variation of the Knight field. As another generalization it is assumed that all nuclear species are described with a single spin temperature. In contrast to the NSF field, this nuclear field B_{N} has a certain direction. Its components are either added to or subtracted from the respective components of the external magnetic field, depending on the experimental conditions. The constant magnetic field B_{z} that is applied by a pair of Helmholtz-coils and varied in a range of $-3\ \mathrm{mT} \leq B_{\mathrm{z}} \leq 3\ \mathrm{mT}$ is also included in this model.

$$S_{\mathrm{z}} = S_0 \frac{\left(B_{\mathrm{z}} + B_{\mathrm{N,z}}\right)^2 + \langle B_{\mathrm{NF,z}}^2 \rangle}{\left(B_{\mathrm{x}} + B_{\mathrm{N,x}}\right)^2 + \left(B_{\mathrm{z}} + B_{\mathrm{N,z}}\right)^2 + \langle B_{\mathrm{NF}}^2 \rangle} \tag{4.27}$$

$$S_{\mathrm{x}} = S_0 \frac{\left(B_{\mathrm{z}} + B_{\mathrm{N,z}}\right) + \left(B_{\mathrm{x}} + B_{\mathrm{N,x}}\right)}{\left(B_{\mathrm{x}} + B_{\mathrm{N,x}}\right)^2 + \left(B_{\mathrm{z}} + B_{\mathrm{N,z}}\right)^2 + \langle B_{\mathrm{NF}}^2 \rangle} \tag{4.28}$$

As for the standard cooling model the regular nuclear field $\boldsymbol{B}_{\mathrm{N}}$, which is determined by eq.(4.23), is assumed to be directed along the total effective field $\boldsymbol{B}_{\mathrm{tot}}^{\mathrm{N}}$ acting on the nuclei, which consists of $\boldsymbol{B}_{\mathrm{tot}}^{\mathrm{N}} = \boldsymbol{B}_{\mathrm{x}} + \boldsymbol{B}_{\mathrm{z}} + \boldsymbol{B}_{\mathrm{e}}$. In this case the Knight field is given by $\boldsymbol{B}_{\mathrm{e}} = b_{\mathrm{e}} \boldsymbol{S}_{\parallel}$.

The equation above allows to obtain the following expressions for the x and z components of the nuclear field:

$$B_{\mathrm{N,x}} = (B_{\mathrm{x}} + b_{\mathrm{e}}S_{\mathrm{x}}) \times \frac{b_{\mathrm{N}}(B_{\mathrm{z}}S_{\mathrm{z}} + B_{\mathrm{x}}S_{\mathrm{x}} + b_{\mathrm{e}}S_{\mathrm{x}}^2 + b_{\mathrm{e}}S_{\mathrm{z}}^2)}{(B_{\mathrm{x}} + b_{\mathrm{e}}S_{\mathrm{x}})^2 + (B_{\mathrm{z}} + b_{\mathrm{e}}S_{\mathrm{z}})^2 + \xi B_{\mathrm{L}}^2} \frac{4(I+1)}{3} \qquad (4.29)$$

$$B_{\mathrm{N,z}} = (B_{\mathrm{z}} + b_{\mathrm{e}}S_{\mathrm{z}}) \times \frac{b_{\mathrm{N}}(B_{\mathrm{z}}S_{\mathrm{z}} + B_{\mathrm{x}}S_{\mathrm{x}} + b_{\mathrm{e}}S_{\mathrm{x}}^2 + b_{\mathrm{e}}S_{\mathrm{z}}^2)}{(B_{\mathrm{x}} + b_{\mathrm{e}}S_{\mathrm{x}})^2 + (B_{\mathrm{z}} + b_{\mathrm{e}}S_{\mathrm{z}})^2 + \xi B_{\mathrm{L}}^2} \frac{4(I+1)}{3} \qquad (4.30)$$

b_{N}, $B_{\mathrm{NF,z}}$, and ζB_{L}^2 were considered fitting parameters and varied to get the best correspondence with the experimentally obtained Hanle-curves. The coefficient b_{e} is given, in principle, by $b_{\mathrm{e}} = -(16\pi/3)\mu_{\mathrm{B}}\zeta^2$, where ζ is the electron density on a nuclear site [123]. The negative sign means that the direction of the Knight field is opposite to that of the electron spin. Since the electron density depends on the QD size, which can vary from dot to dot, the value of ζ is unknown a priori. Equations (4.27),(4.28), (4.29) and (4.30) contain the Cartesian components of the electron spin and of the dynamic nuclear polarization as unknown quantities. The Cartesian components of the electron spin and of the dynamic nuclear polarization are found by numerical solution of equations (4.27),(4.28), (4.29) and (4.30) for transverse magnetic fields in the range from $-20\ \mathrm{mT} \leq B_{\mathrm{x}} \leq +20\ \mathrm{mT}$ and for several values of the longitudinal magnetic field used in experiment.

In the calculations, the coefficient b_{e} has been chosen such that the Knight field compensates the z component of the magnetic field at the point where the dips near the central peak of the Hanle-curve disappear (ref. to Figure 4-9).

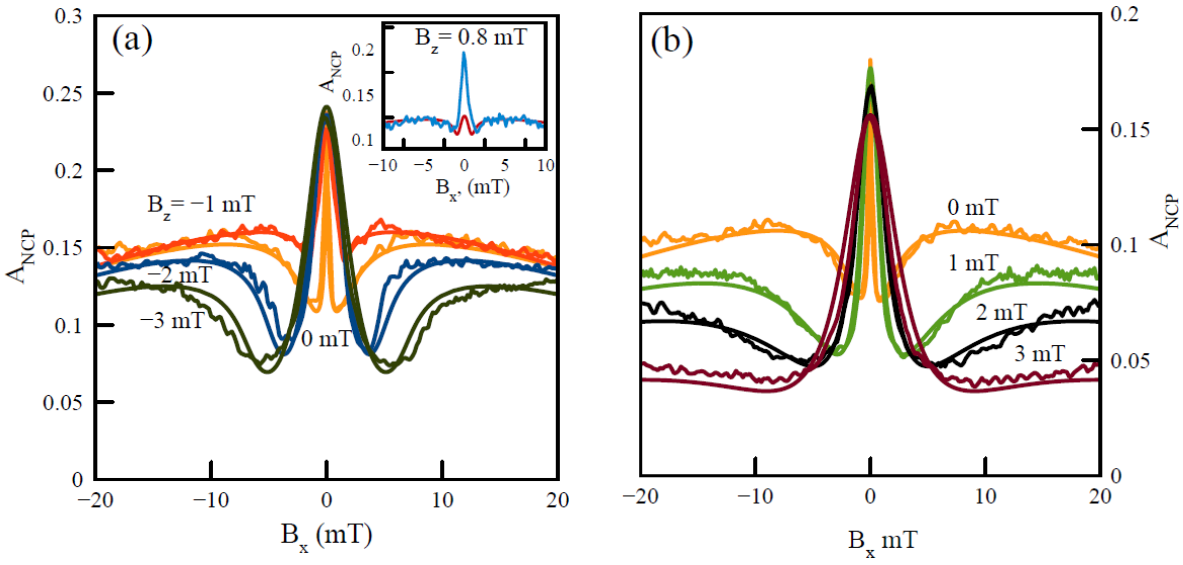

Figure 4-9 Comparison of the calculated curves according to the extended cooling model which included the NSF (solid lines) with the measured data for (a) negative and (b) positive longitudinal external field $\boldsymbol{B_z}$. The corresponding values of $\boldsymbol{B_z}$ are given for each curve. The inset shows the central part of experimental and calculated Hanle-curves in the case of mutual compensation of $\boldsymbol{B_z}$ and $\boldsymbol{B_e}$. The fitting parameters are $b_N = 400$ mT, $\sqrt{\langle B_{NF}^2 \rangle} = 25$ mT, $b_e = 2$ mT. The curves were obtained with sample #980 under excitation at 1.49 eV, detected at 1.42 eV at temperature $T = 1.8$ K [155].

For comparison of the calculated results with the experimental data the calculated values of S_z are multiplied by a factor α'', which takes into account the reduced magnitude of PL polarization.This reduction is presumably due to the fact that some QDs are charged neutrally and that their PL is non polarized. α''= 0.2 ± 0.02 for curves measured at negative B_z and α''= 0.16 ± 0.01 for positive values of B_z. The latter curves were measured at a slightly lower power of excitation. The possible reason for the pump-power dependence of α'' is the creation of photoinduced electrons, which slightly change the fraction of charged QDs.

The Equations (4.27), (4.28), (4.29)and (4.30) are interconnected cubic equations. Their solution is unstable in the most general case, complicating the determination of fitting parameters. For simplicity reasons, the calculations are performed in two steps. In the first step, the x component of the electron spin is excluded from the equations because it weakly affects the nuclear polarization. In addition, the small difference in orientation of effective fields $\boldsymbol{B}_{tot}^{e}$ and $\boldsymbol{B}_{tot}^{N}$ is neglected. Besides, a fitting parameter is introduced which characterizes the real nuclear field acting on the electron spin:

$$b_N^{'} = \frac{b_N \left(B_{tot}^{N}\right)^2}{\left(B_{tot}^{N}\right)^2 + \zeta B_L^2} \tag{4.31}$$

This reduces the system of equations to one equation of fifth order for S_z.

$$\rho = \frac{S_z}{S_0} = \frac{2B_{e,z}}{b_e} \tag{4.32}$$

$$= \frac{\left[B_z B_x^2 + (B_z - S_0 b'_N)\left(B_{e,z} + B_z\right)^2\right]^2 + \langle B_{NF,z}^2\rangle\left[B_x^2 + \left(B_{e,z} + B_z\right)^2\right]}{B_x^2\left[B_x^2 + \left(B_{e,z} + B_z\right)^2 - S_0 b'_N\left(B_{e,z} + B_z\right)\right]^2 + \left[B_z B_x^2 + (B_z - S_0 b'_N)\left(B_{e,z} B_z\right)^2\right]^2 + \langle B_{NF}^2\rangle\left[B_x^2 + \left(B_{e,z} + B_z\right)^2\right]}$$

Equation (4.32) is numerically solved, which allows to determine the range of possible values for quantities b_N and $B_{NF,z}$. In the second step, the whole system of equations (4.27), (4.28), (4.29) and (4.30) is solved and their real roots are used for modeling the Hanle-curves, slightly varying the fitting parameters determined in the first step. The best coincidence with the experimental data is achieved with virtually the same values of b_N and $B_{NF,z}$ as in the first step of the fitting.

4.2.4 Conclusions: Comparison of experimental data and the extended cooling model

As demonstrated in the examples of the calculated Hanle-curves shown in Figure 4-9, reasonable agreement between calculated and measured curves is observed for positive as well as for negative B_z. Some deviations from experiment occur for magnetic fields $0.5\ \mathrm{mT} \leq B_z \leq 1\ \mathrm{mT}$, where the theoretically calculated amplitude of the central peak is considerably smaller than the central peak observed experimentally (see inset in Figure 4-9a). The strong decrease of the peak amplitude obtained in the calculations is due to the depolarization of the electron spin by the nuclear spin fluctuations, when the longitudinal component of the total field disappears and the nuclear field does not build up. Experiments also show a decrease of the central peak of about 20%, which is, however, significantly smaller than the one predicted theoretically. A possible reason for this discrepancy between the theory and the experiment could be related to the spread of Knight fields in the QD ensemble, which is ignored in theory. Another possible reason is the polarization of quadrupole-split nuclear spin states, which can stabilize the electron spin polarization [85]. Further study is needed to clarify this problem. The good overall correspondence of the simulated and measured Hanle-curves confirms the validity of the extended cooling model developed. The NSF amplitude $\sqrt{B_{NF}^2}$ extracted from the fitting is close to 25 mT for all the measured Hanle-curves fitted for different B_z. This value is somewhat larger than the one obtained in another experiment with similar quantum dots [167]. A possible reason for this overestimation of the NSF amplitude is the increase of the wings of the Hanle-curves due to polarization of quadrupole–split nuclear spin states, which becomes noticeable at magnetic fields $|B_x| \approx 20\ \mathrm{mT}$ and larger and leads to an enhancement of A_{NCP} in this range [168]. The validity of the assumption of an isotropic distribution of NSF is verified by replacing

$\langle B^2_{\mathrm{NF,z}}\rangle \rightarrow \beta\langle B^2_{\mathrm{NF,z}}\rangle$ in the numerator of eq.(4.32) and optimizing the factor β. The optimal value of β was found to be in the range from 1.2 to 1.4. It can be supposed that some asymmetry in space of the distribution of NSF can also be due to the quadrupole stabilization of nuclear spins. The quadrupole stabilization of nuclear spins is mainly directed along the growing direction (z-axis) of the sample, since the strain which is one of the main reasons for the quadrupole stabilization is directed along this direction. There are traces of effects that can be interpreted as quadrupole effects of the nuclei, but the small range B_{x}, that is used for the fitting, still justifies a negligence of the quadrupole effects in the model used. In this range of B_{x} the effects of quadrupole stabilization on the measurement are negligibly small in comparison to the NSF, as shown by the comparison of the fitted curves. Furthermore it is possible to get a clear idea about the vector representation of the time-averaged electron spin and nuclear polarization in the system under study. Figure 4-10 schematically shows the evolution of the respective vectors under variation of the transverse magnetic field B_{x} and for zero longitudinal field. For uniformity, the electron spin and the nuclear polarization are presented as effective fields, $\boldsymbol{B}_{\mathrm{e}}$ and $\boldsymbol{B}_{\mathrm{N}}$, respectively.

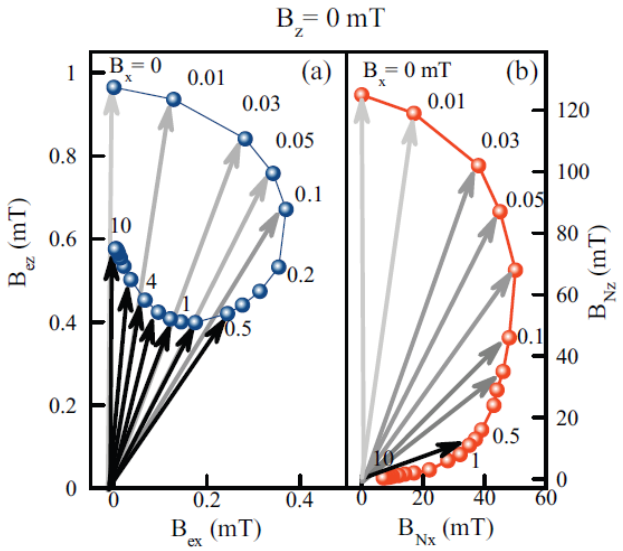

Figure 4-10 (Color online) Evolution (a) of Knight field $\boldsymbol{B}_{\mathrm{e}}$ and (b) of nuclear field $\boldsymbol{B}_{\mathrm{N}}$ at $B_{\mathrm{z}} = 0$ under changing external magnetic field B_{x}. Values of B_{x} (in mT) are given for some positions of the evolution curves. The step between points is not constant. Arrows show respective $\boldsymbol{B}_{\mathrm{e}}$ and $\boldsymbol{B}_{\mathrm{N}}$ vectors. The curves were obtained with sample #980 under excitation at 1.49 eV, detected at 1.42 eV at temperature $T = 1.8$ K [155].

The nuclear field at zero B_{x} is controlled only by the Knight field, which is directed along the z axis. When a small transverse magnetic field, $B_{\mathrm{x}} \ll B_{\mathrm{e}}$ is applied, the nuclear field deviates from the z axis, so that its x component becomes orders of magnitude larger than the magnetic field B_{x} . For example, $B_{\mathrm{Nx}} \approx 50$ mT at $B_{\mathrm{x}} = 0.1$ mT; see Figure 4-10(b). This is a clear illustration of the "amplification" of the external magnetic field by the nuclear field. The electron spin polarization follows the nuclear field, which becomes quickly tilted with the magnetic field and depolarizes the electron spin. This behavior of the electron spin explains the small width of the central peak of the Hanle-curve. For a further increase of the

magnetic field, the magnitude of the nuclear field rapidly drops so that $|B_N| \leq |B_x|$ at $B_x \geq 10$ mT.

Application of B_z with a magnitude larger than that of the Knight field significantly changes the behavior of the electron and nuclear polarizations, as demonstrated in Figure 4-11 for $|B_z| = 2$ mT.

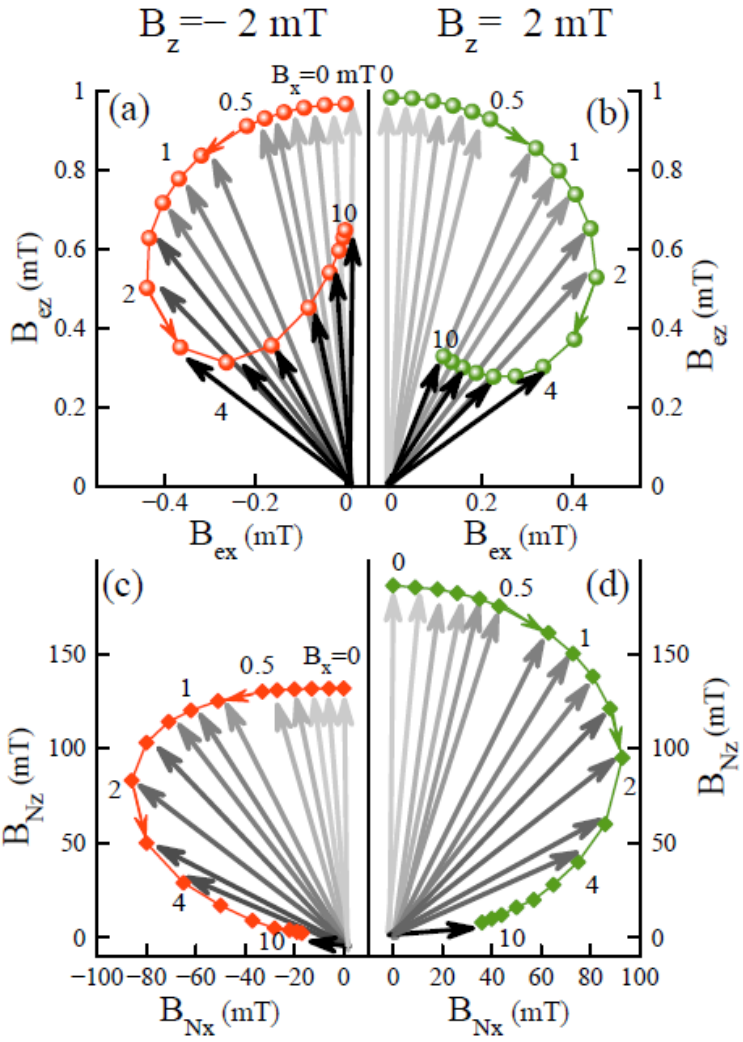

Figure 4-11 (Color online) Evolution of (a) and (b) the electron and (c) and (d) nuclear fields for application of negative [(a) and (c)] and positive [(b) and (d)] longitudinal magnetic fields with relatively large magnitudes. Like in Figure 4-10 the diagrams are shown only for positive B_x . The curves were obtained with sample #980 under excitation at 1.49 eV, detected at 1.42 eV at temperature $T = 1.8$ K [155].

An increase of the transverse magnetic field B_x is accompanied by inclination and reduction of the Knight field; however, the reduction is not as fast as at $B_z = 0$. The direction of the Knight field inclination depends on the sign of the longitudinal magnetic field; see Figure 4-11(a) and Figure 4-11(b). The nuclear field $\boldsymbol{B}_N$ is directed along the z-axis at zero transverse magnetic field and has the maximal value $\boldsymbol{B}_N = b_N \boldsymbol{S}_0 = 200$ mT at positive B_z when the Knight field and the longitudinal magnetic field add up (ref. to Figure 4-11d). At opposite (negative) sign of B_z, when the fields are subtracted from each other, the

total effective field acting on the nuclei is smaller, which results in some reduction of the nuclear polarization (ref. to Figure 4-11c). The direction of inclination of the nuclear field is also dependent on the sign of B_z. In particular, the x component of the nuclear field is negative at negative B_z, so that compensation of the external magnetic field B_x occurs at $B_x \approx 10$ mT. This compensation results in partial restoration of the electron spin polarization and its reorientation along the z-axis; (ref. to Figure 4-11a). The decrease of the magnitude of the Knight field relative of its initial value at $B_x = 0$ mT is the effect of the nuclear spin fluctuations, as discussed above.

4.3 Suppression of nuclear pumping

The idea of the experiment presented in the following section is to create short excitation pulses with a CW-laser and to find a setting where the time of excitation τ_{AM} is too short for nuclear polarization. Such a setting depends on the relation of the modulation frequency f_{AM} and τ_{AM}. This situation where no nuclear polarization occurs is given for $f_{AM} = 100$ kHz and $\tau_{AM} = 0.5$ µs. Such timescale of modulation is reasonable as the typical timescale of nuclear spin dynamics is in the order of hundreds of µs (ref. to sec. 2.1.5). The experiments are performed on sample #980.

4.3.1 Experimental observations

It is also possible to combine the amplitude modulation with the polarization modulation, so that one pulse of excitation is σ^+polarized and the next following pulse is σ^- polarized. In contrast to sec. 4.1, the timescale for the modulation period f_{AM+PM} is in the range of µs.

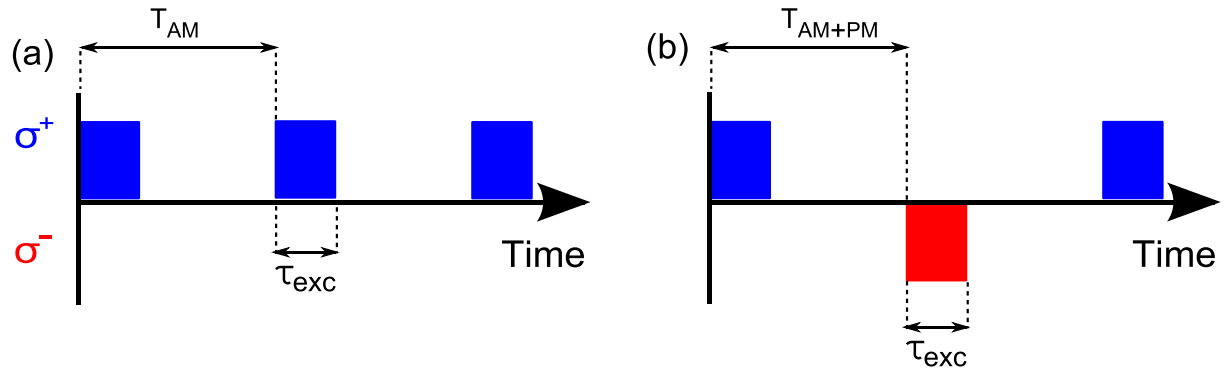

Figure 4-12 (a) Excitation protocol for measurement with pure amplitude modulation (AM). (b) with amplitude modulation combined with polarization modulation (AM+PM). Blue and red rectangles indicate $\sigma^+$and σ^- polarized light excitation with equal intensity and equal duration.

As an introduction to the new regime measurements with pure AM in this timescale are presented first. Then two types of measurements in which the same modulation frequency was used are compared with each other. For the one of these measurements a pure AM was applied, while for the other measurement a combination of PM+AM was used. The

excitation protocol in Figure 4-13 shows the repetition time of polarized light pulses T_{AM} and the duration τ_{exc} can be varied. With a constant modulation time T_{AM} and an increasing of the excitation time τ_{exc}, the excitation becomes similar to the excitation described in sec. 4.4.

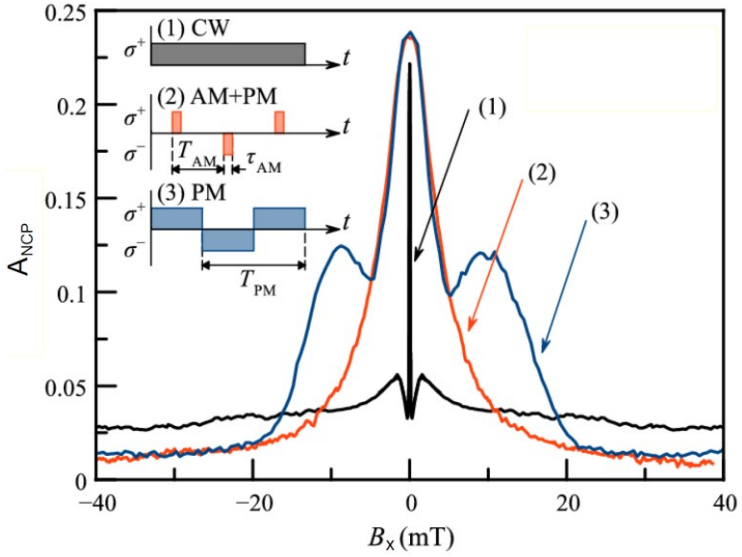

Figure 4-13 (Color line) Hanle-curves measured in CW regime (black curve), polarization modulation of excitation (T_{PM} = 40 µs, blue curve), and polarization and amplitude modulation of excitation (T_{AM} = 20 µs, τ_{AM} = 5 µs, red curve). The curves were obtained with sample #980 under excitation at 1.49 eV, detected at 1.42 eV at temperature $T = 1.8$ K [167].

The blending of the excitation protocol can be also traced by the shape of the Hanle-curve. This process of blending can be characterized in two steps. Increasing τ_{exc} in a range up to ~70% of the modulation period leads to an formation of a W-structure at the center position of the Hanle-curve (around $B_{\mathrm{x}} = 0$ mT). The width of the Hanle-curve is not influenced in this regime (short pulse regime). If the excitation time τ_{exc} exceeds ~70% of the modulation period T_{AM}, a second regime starts (long pulse regime). In this regime the W-structure is nearly completely developed, but there is still a difference to the W-structure of a Hanle-curve obtained under pure PM. The main effect that can be observed in the long pulse regime is the widening of the Hanle-curve. It is remarkable that a dark time of 250 ns leads to a significant difference to the Hanle-curve obtained under CW excitation (ref. to Figure 4-14). Each curve is measured during 0.5 µs of excitation, so that for the long excitation regime it is possible to measure at the beginning and at the end of the excitation pulse. The comparison shows that there is no measurable development of the Hanle-curve during an excitation pulse, but that the Hanle-curve is built up at the very beginning of the excitation pulse. This indicates that the system reaches a state of equilibrium under the special excitation protocol (ref. to Figure 4-14).

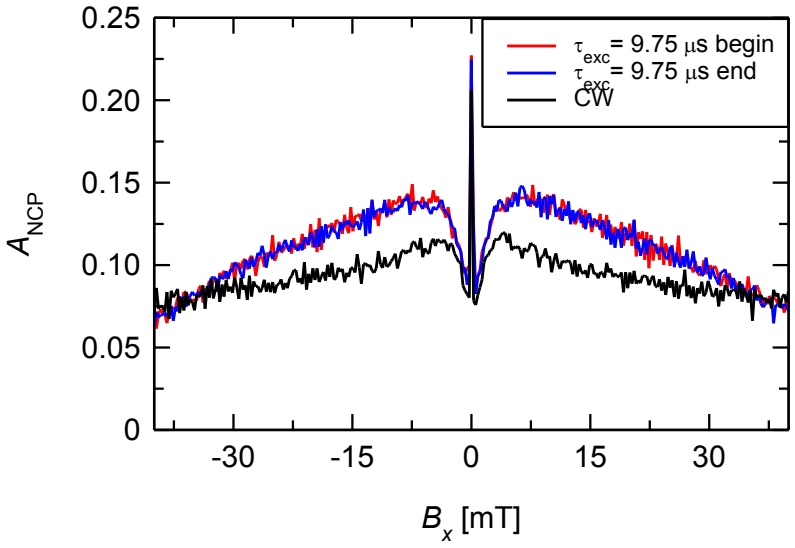

Figure 4-14 Hanle-curves obtained with $T_{\mathrm{AM}} = 10\ \mu s$. Red curve is detected during the first 0.5 µs of the excitation pulse. Blue curve is detected during the last 0.5 µs of the excitation pulse. The curves were obtained with sample #980 under excitation at 1.49 eV, detected at 1.42 eV at temperature $T = 1.8\ \mathrm{K}$.

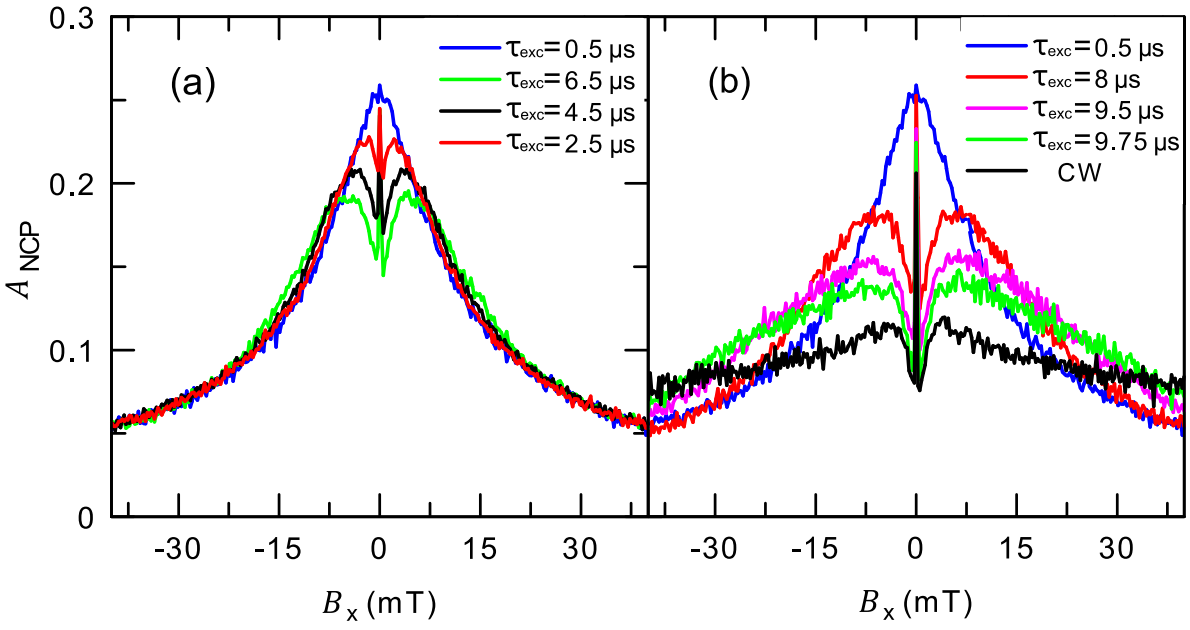

Figure 4-15 Hanle-curves obtained with $T_{\mathrm{AM}} = 10\ \mu s$. The different durations τ_{exc} of the excitation pulse are labeled for each curve within the figure. Part (a) presents the short pulse regime, while part (b) presents the long pulse regime and a Hanle-curve obtained under CW excitation. The curves were obtained with sample #980 under excitation at 1.49 eV, detected at 1.42 eV at temperature $T = 1.8\ \mathrm{K}$.

Another parameter that influences the width and the amplitude A_{NCP} of the Hanle-curve is the excitation power P_{exc}. As shown for the short pulse regime in Figure 4-16 an increase of P_{exc} leads to a widening of the Hanle-curve and simultaneously to an increase of A_{NCP}.

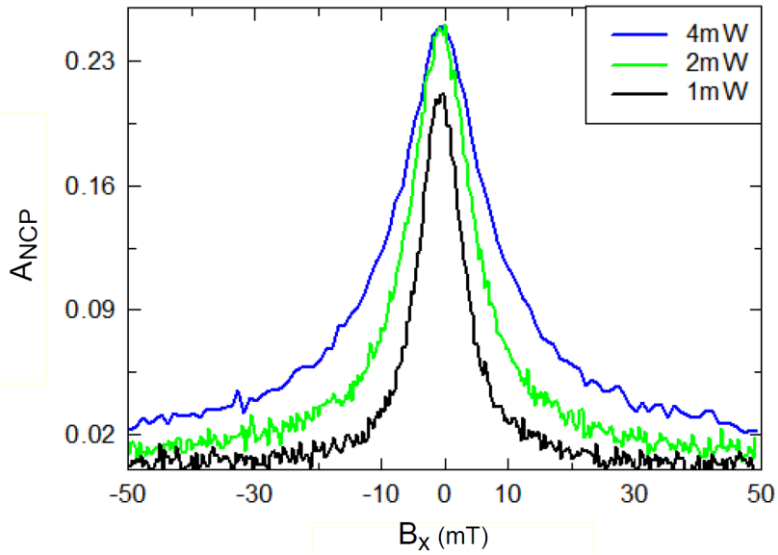

Figure 4-16 (color lines) Hanle-curves obtained under AM with $T_{\mathrm{AM}} = 10\mu\mathrm{s}$ and $\tau_{\mathrm{exc}} = 0.3\mu\mathrm{s}$ for different excitation power. The curves were obtained with sample #980 under excitation at 1.49 eV, detected at 1.42 eV at temperature $T = 1.8$ K.

At approximately $P_{\mathrm{exc}} = 2$ mW the amplitude of A_{NCP} is saturated, so that a further increase of P_{exc} results in a widening of the Hanle-curve. The curve can be fitted by a Lorentzian curve $S_{\mathrm{z}}(B_{\mathrm{x}}) = \frac{S_0}{1+\left(\frac{B_{\mathrm{x}}}{B_{1/2}}\right)^2}$. Here S_0 is the initialized electron spin and $B_{1/2}$ is the half width at half maximum (HWHM) which is varying from 2 mT to 10 mT for $P_{\mathrm{exc}} = 0.5 - 10$ mW. Figure 4-17 shows that, in the regime of short excitation pulses, an additional modulation of polarization has no influence on the shape of the Hanle-curve.

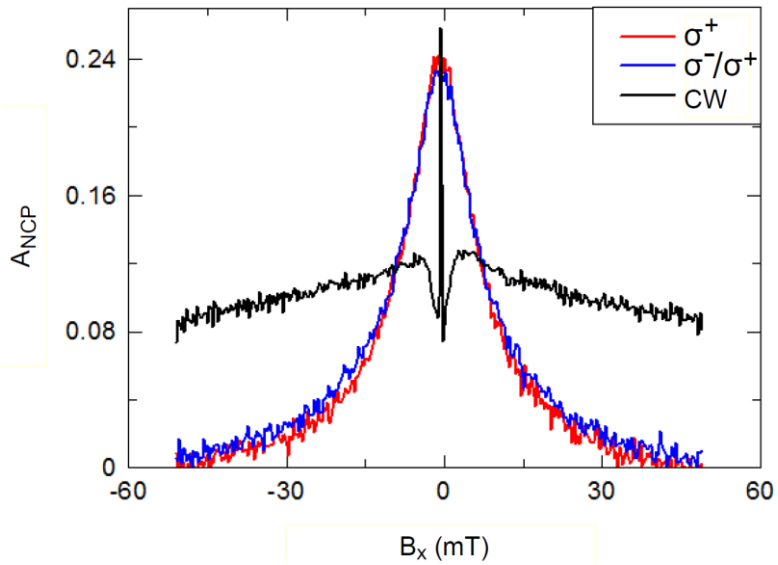

Figure 4-17 Blue and red Hanle-curve are obtained for with $T_{\mathrm{AM}} = 10\mu\mathrm{s}$ and $\tau_{\mathrm{exc}} = 0.3\mu\mathrm{s}$. The excitation pulses for the red curve are always σ^+ polarized, while the excitation pulses for the blue curve alternate in polarization, so that a σ^+ pulse is followed by a σ^- pulse. In comparison to the modulated Hanle-curves is Hanle-curve shown obtained under CW excitation (black curve). The curves were obtained with sample #980 under excitation at 1.49 eV, detected at 1.42 eV at temperature $T = 1.8$ K.

4.3.2 Conclusions

The introductory measurements with pure AM give an useful overview over nuclear spin dynamics and show that the nuclear spin dynamics depend on the magnitude of B_x. Within a range of about $-10\ \mathrm{mT} \leq B_x \leq +10\ \mathrm{mT}$, the nuclear spin responds faster to the circularly polarized light via the hyperfine interaction than in larger fields of B_x. In this range of about $-10\ \mathrm{mT} \leq B_x \leq +10\ \mathrm{mT}$, an increase of τ_{exc} leads to a decrease of A_{NCP}. As already mentioned in ref. [84] and shown in sec. 4.2.4, the appearance of a W-structure is regarded as a reliable evidence for nuclear polarization. This leads to the interpretation that a buildup of nuclear polarization leads to a decrease of A_{NCP}. This is in agreement to ref. [153], where for the same sample the use of RF-fields under CW-laser excitation leads to a depolarization of the nuclear spin system in approximately the same range of B_x. This depolarization of the nuclear spin system causes an increase of A_{NCP}. In the range of $B_x > 10\ \mathrm{mT}$ a longer excitation time τ_{exc} is required to observe an effect. In contrast to the smaller values of B_x, an increase of τ_{exc} leads to an increase of A_{NCP}. The different dynamics and opposite influences on A_{NCP} due to nuclear polarization lead to the assumption of two different sub ensembles of nuclei that interact with the electron in different ways, depending on the magnitude of B_x. This assumption has been validated by measurements and calculations performed for this thesis [168] [167]. In the smaller range of B_x nuclear spin states $|\pm 1/2\rangle$ are responsible for the influence on A_{NCP}, while for larger values of B_x A_{NCP} is dominated by $I_z \geq |\pm 3/2\rangle$ states (ref. to sec. 4.1.1).

The detection at the beginning and at the end of the excitation pulse results in the same shape of the Hanle-curve. For a correct interpretation of the Hanle-curve one should keep in mind that for each point of the Hanle-curve the sample is continuously excited according to the excitation protocol and the luminescence is accumulated for 7 sec. The dynamic process of nuclear polarization takes place within the first second of excitation, when the modulated laser light hits the sample for the first time. But at the point of time when the measurements presented in this chapter are taken the nuclear polarization is already saturated. However, different relations of the dark time and the excitation time result in different shapes of the Hanle-curve. The longer the excitation time within the modulation period, the closer the curve resembles a Hanle-curve obtained under CW-laser excitation without any modulation. This means that even for $\tau_{exc} = 2.5$ µs, with a dark time of 7.5 µs, some nuclear polarization is restored during the dark time. This accumulated nuclear polarization gives rise to the W-structure. The only exception is the curve with $\tau_{exc} = 0.5$ µs, which has a Lorentzian shape. At such conditions every nuclear polarization that could appear during the 0.5 µs of excitation is depolarized during the 9.5 µs of dark time. Even alternation of polarization, so that one pulse is σ^+ polarized and the next following pulse is σ^- polarized, has no influence on the shape of the Hanle-curve. If there was a nuclear polarization that remained longer than one excitation period, the alternating polarization would lead to a different shape of the Hanle-curve, because an alternating polarization influences the nuclear polarization in a different way than an excitation with one polarization (ref. to sec. 4.4). In the following text, such Hanle-curves, which show no sign of nuclear polarization, will be called “electron-peak”

or in short form “e-peak”. From the fitting of the Hanle-curve obtained with $\tau_{\mathrm{exc}} = 0.5\,\mu\mathrm{s}$ and $t_{\mathrm{AM}} = 100\,\mathrm{kHz}$ it is assumed that the width of the Hanle-curve is not determined by nuclear polarization but by the dephasing time T_2 of the electron spin. From the fitting with $S=S_0/(1+(B/B_{1/2})^2)$ and the electron g-factor $|g_{\mathrm{e}}| = 0.6$ the time $T_2 = 1.9\,\mathrm{ns}$ can be calculated. This value is reasonable, because in such small external fields the dephasing of the electron spin is mainly caused by the electron spin precession about the frozen magnetic field of the nuclei [37]. The time of 1.9 ns can be also interpreted as the average time between the excitation events.

4.4 Resonant pumping of nuclear spins

In this section a possibility to manipulate the component of the nuclear spin that is transverse to the external field B_{x} by optical excitation is presented. The optical manipulation leads to a coherent precession of the transverse component for every nucleus whose Larmor precession frequency is equal to the modulation frequency. This effect is called resonant pumping of nuclear spin. In sec. 4.4.2 an RF-field is added to the optical modulation which leads to an amplification of the resonant pumping effect but the principle of the observed effect is still the same.

In all experiments where the modulation of polarization (PM) is used the polarization changes between the two circular polarizations, σ^+ and σ^-. The relation between the two polarizations always remains the same, so that the sample is excited for an equal amount of time with both polarizations. The only parameter that is varied from measurement to measurement is the period of modulation.

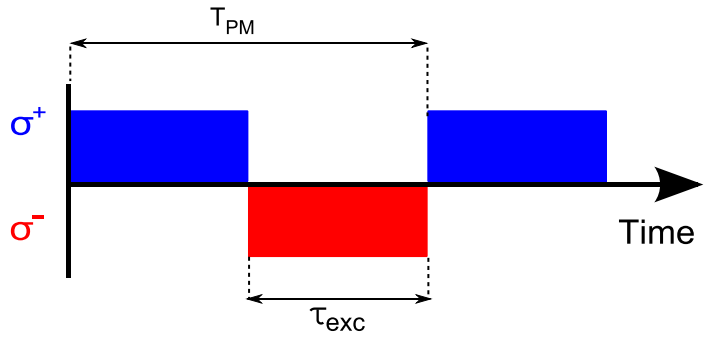

Figure 4-18 Excitation protocol for measurement with polarization modulation (PM). Blue and red rectangles indicate $\sigma^+$and σ^- polarized light excitation with equal intensity and equal duration.

The alternating excitation with σ^+ and σ^- polarized light is realized in the range of 2.5 kHz to 200 kHz. To calculate A_{NCP} it is needed to measure the intensity of right- and left-handed polarized photoluminescence. In this setup it is not possible to measure these two components at the same time. Therefore one component is measured during the whole excitation with σ^+ polarized light and the other component is measured during the whole

excitation with σ^- polarized light. The Hanle-curves thereby obtained are average curves. Dynamics of the electron-nuclei system during the excitation time cannot be detected. In comparison to the Hanle-curve obtained under CW-laser excitation with the same excitation intensity the polarization degree of the photoluminescence in smaller external magnetic field is already zero for a PM excitation. The Hanle-curve measured under modulated polarization of excitation (blue curve in Figure 4-13) shows two strong additional maxima at about $|B_x| = 10\ \mathrm{mT}$. At small modulation frequencies f_{PM}, the Hanle-curve consists of a central peak and hardly visible sidebands. Its dependence on modulation frequency, f_{PM}, is illustrated in Figure 4-19.

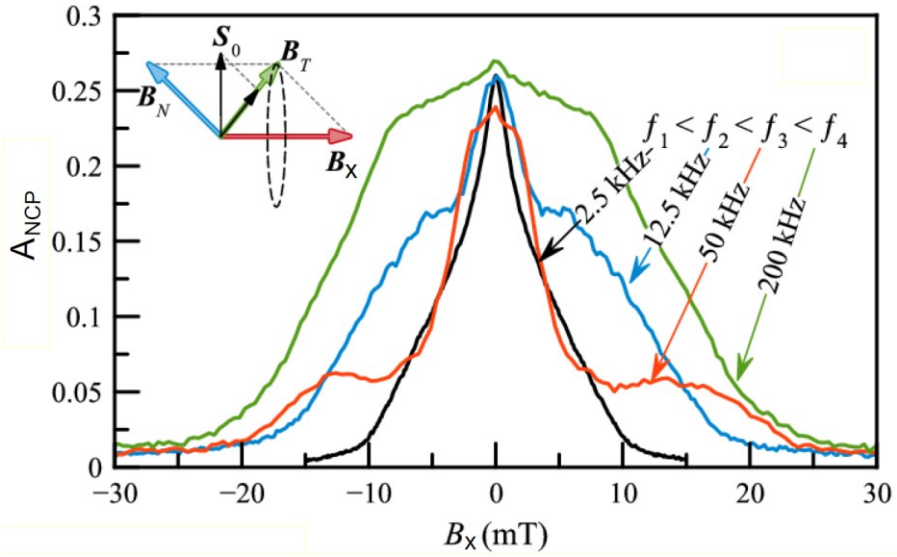

Figure 4-19 (Color online) (a) Hanle-curves measured at modulated polarization of excitation with f_{PM} = 2.5 kHz (black curve), 12.5 kHz (blue curve), 50 kHz (red curve), and 200 kHz (green curve). Inset shows a scheme illustrating the pumping of nuclear field. The curves were obtained with sample #980 under excitation at 1.49 eV, detected at 1.42 eV at temperature $T = 1.8\ \mathrm{K}$ [167].

At small f_{PM}, the Hanle-curve consists of a central peak and hardly visible sidebands (black curve in Figure 4-19. As the modulation frequency rises, the sidebands become more pronounced while their amplitude decreases so that they disappear again at $f_{PM} > 100\ \mathrm{kHz}$. Simultaneously the central peak becomes wider and new shoulders appear (color lines in Figure 4-19).

4.4.1 Conclusions

The effect of modulated optical excitation on electron-nuclear spin systems has been studied earlier for bulk semiconductors [123, 169] and quantum wells [170, 171]. In these works, the effect was observed as dispersion-like peculiarities superimposed on a smooth Hanle-curve. The authors treated the effect as the nuclear magnetic resonance (NMR). In contrast to conventional NMR measurements these are "all optical" measurements, in which the effective alternative magnetic field, which is normally induced by a pair of radiofrequency

coils, is induced optically. For this purpose the sample is excited with alternating circular polarized light, so that the initialized spin direction of the excited electron is either polarized in +z or -z direction depending on the helicity of the optical polarization. The direction of the Knight-field is bound to the spin direction of the electron. Therefore the alternating Knight-field replaces the function of an alternating magnetic field applied by a pair of RF-coils and equalizes populations of nuclear spin sublevels at exactly resonant conditions. This is the case when the modulation frequency f_{PM} equals the Larmor precession of the nuclei. No pumping of nuclear spin system occurs when the modulation frequency is far from the resonance.

The effect observed in the experiments performed for this thesis is rather different. There are clear resonances beyond the e-peak rather than dispersion-like peculiarities. A noticeable difference to the previously mentioned structures like quantum wells or bulk material is the considerably larger hyperfine interaction in QDs under study, which results in more effective optical pumping and noticeable polarization of nuclear spins. This effect can simply be understood considering the dynamics of an electron spin and nuclear spins with I = 1/2 (see inset in Figure 4-19). The polarized electron polarizes nuclear spins via hyperfine interactions. Simultaneously, the electron feels the nuclear polarization as an effective magnetic field, the Overhauser field $\boldsymbol{B}_{\mathrm{N}}$, and rapidly precesses about the total field, $\boldsymbol{B}_{\mathrm{tot}}^{\mathrm{e}} = \boldsymbol{B}_{\mathrm{x}} + \boldsymbol{B}_{\mathrm{N}}$, so that only the spin projection on this field is saved. Hyperfine interactions with such electrons can pump both the $B_{\mathrm{N,z}}$ and $B_{\mathrm{N,x}}$ components of the nuclear field. The $B_{\mathrm{N,z}}$ component can only be pumped when the frequency of modulation of optical polarization coincides with the Larmor frequency ω_{L} of the nuclear spin precession. In this case, the $B_{\mathrm{N,z}}$ component is pumped along the +z direction during one half period of optical excitation, as long as the electron spin is pointing into the same direction. A pumping along -z direction occurs during the other half period of modulation, when the polarization of excitation changes and the electron spin is pointing into the other direction. A building up of $B_{\mathrm{N,z}}$ leads to a stabilization of the electron spin along the z-direction which in turn leads to an increase of A_{NCP}.

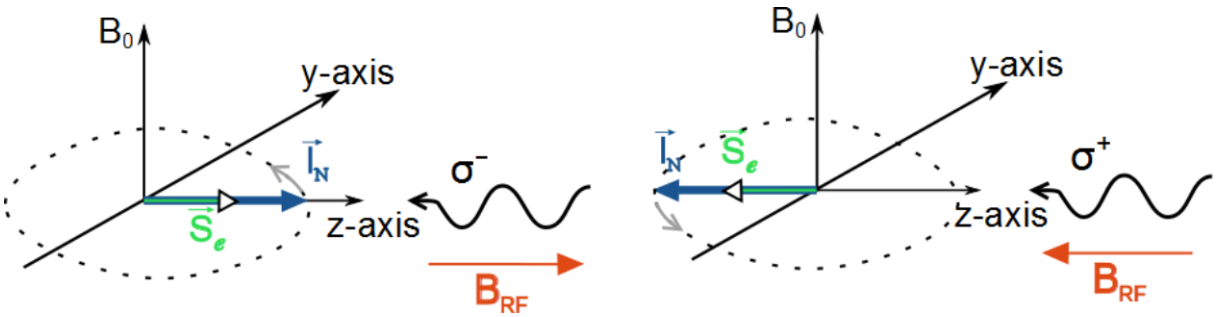

Figure 4-20 Schematic illustration for resonant pumping of nuclear spin. The initialized spin direction of the electron $\boldsymbol{S_0}$ is codirected to the nuclear spin $\boldsymbol{I}_{\mathrm{N}}$ and to the externally applied RF-field due to the chosen polarization ($\sigma^+;\sigma^-$) of the excitation light. The Larmor frequency of the nuclear spin is equal to the polarization modulation frequency of the optical excitation.

The direction of the $B_{\mathrm{N,x}}$ component is independent of the initial orientation of the electron spin and only determined by the signs of the electron and nuclear g-factors. It is directed against the external magnetic field in the studied QDs. The efficiency of pumping of this component depends on the x-projection of the electron spin on the total field $\boldsymbol{B}_{\mathrm{tot}}^{\mathrm{e}}$ and increases when $B_{\mathrm{N,z}}$ becomes large enough, which is possible in resonant conditions. This experiment shows that the polarization dynamics in QDs is totally different from that observed earlier for bulk materials and QWs. There is real resonant pumping of the nuclear spin system, which results in strong increase (not decrease, like in ref. [170, 171]) of nuclear polarization at strictly resonant conditions. The effect described is called "resonant pumping of the nuclear spin" and can be amplified by an additional RF-field excitation synchronized with the PM as described in the following chapter. A more detailed analysis of this effect is also given in the following chapter.

4.4.2 Amplified resonant pumping of nuclear spin

The synchronized modulation of a sinusoidal RF-field $U_{\mathrm{RF}} = U_0 \cdot \sin(\omega_{\mathrm{PM}} t + \Delta\varphi)$ with polarization modulation, is studied in the range of $f_{\mathrm{PM+RF}} = 2.5$ kHz to 1 MHz.

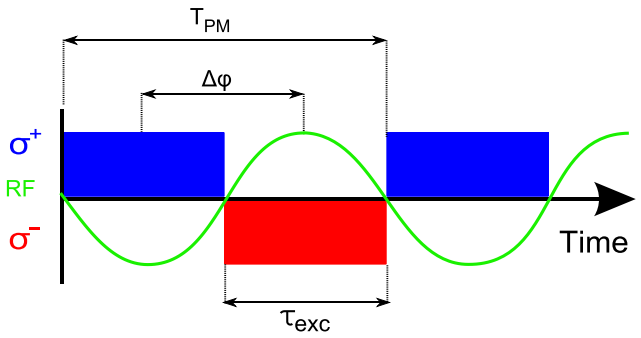

Figure 4-21 Excitation protocol for measurement with polarization modulation combined with RF excitation (PM+RF). Blue and red rectangles indicate $\sigma^+$and σ^- polarized light excitation with equal intensity and equal duration. Green sinusoidal curve represents the RF excitation with equal modulation period T_{PM} like the modulation of polarization but shifted with a certain phase $\Delta\varphi$.

The limiting factor for the modulation frequency is the used pulse generator of the electro-optical modulator. The behavior of the Hanle-curve is studied in this frequency range of modulation for different phases $\Delta\varphi$ between the polarization modulation and the RF excitation. The intensity of excitation and the intensity of the RF-field is adjusted to every modulation frequency in a small range to obtain the most distinct Hanle-curve. As shown in Figure 4-22, a very high excitation intensity P_{exc} or a very strong RF-field lead to a bloating of the Hanle-curve. In contrast, a very weak excitation intensity P_{exc} leads to a low polarization degree of the Hanle-curve which makes the analysis impossible. The influence of a very weak RF-field on the Hanle-curve does also not suffice for clear analysis.

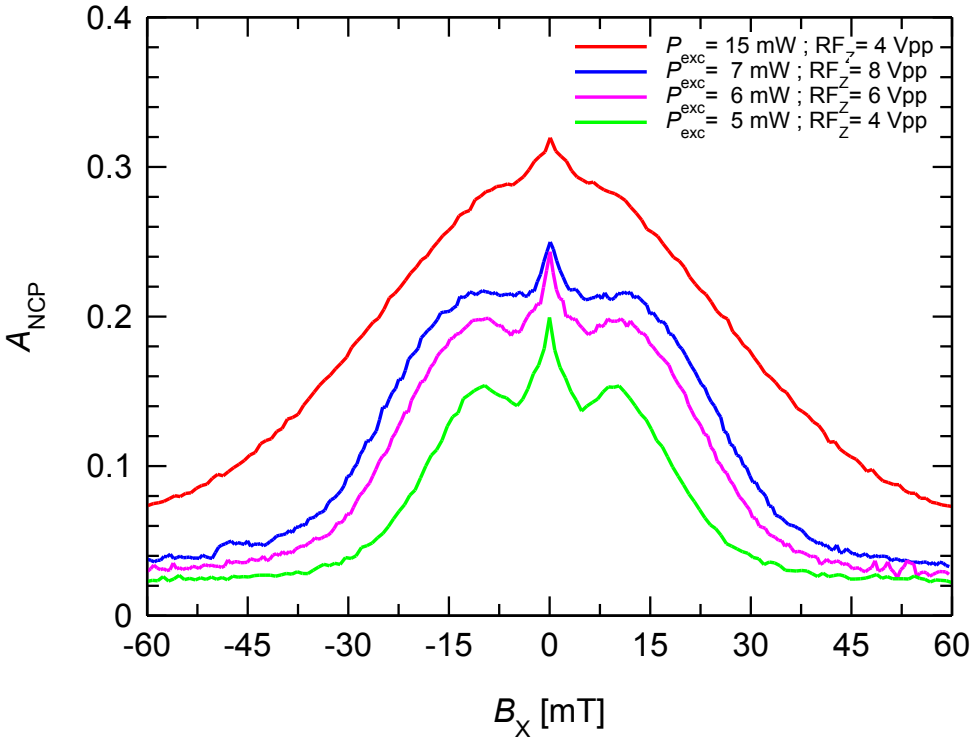

Figure 4-22 All Hanle-curves measured with 50 kHz of PM+RF modulation with the same phase Δφ. The different excitation powers and RF amplitudes are shown for each curve. The curves were obtained with sample #900 under excitation at 1.47 eV, detected at 1.34 eV at temperature $T = 1.8$ K.

The two studied samples show a similar behavior on the excitation protocol, where sample #980 gives a more pronounced response to the modulation. Figure 4-23 and Figure 4-24 show the dependence of the shape of the Hanle-curve on the phase between for two modulation frequencies.

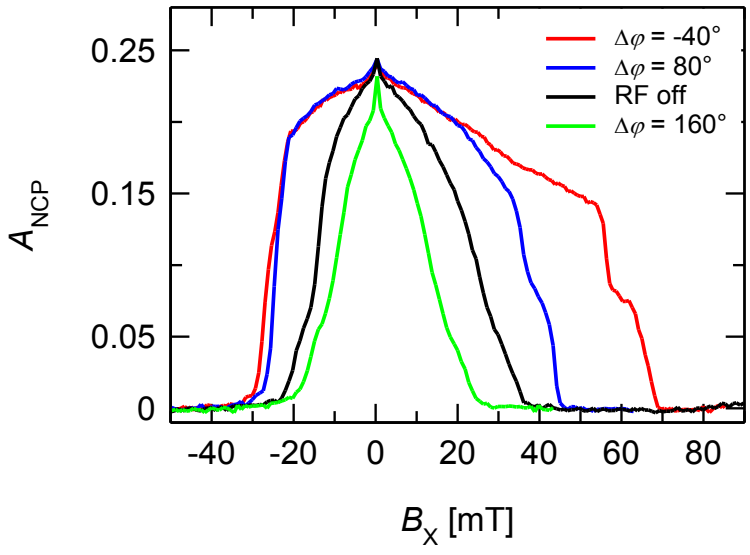

Figure 4-23 All Hanle-curves measured with 600 kHz of PM+RF modulation with the same power of excitation and the same RF amplitude but different phase Δφ. The different phase Δφ is shown for each curve. The curves were obtained with sample #980 under excitation at 1.49 eV, detected at 1.42 eV at temperature $T = 1.8$ K.

Depending on the phase $\Delta\varphi$, the resulting Hanle-curve is either wider or more narrow than a Hanle-curve obtained under polarization modulation without RF-field excitation. The case of a widening of the Hanle-curve with a hysteresis behavior is observed for sample #980 for the whole frequency range of modulation (ref. to Figure 4-24).

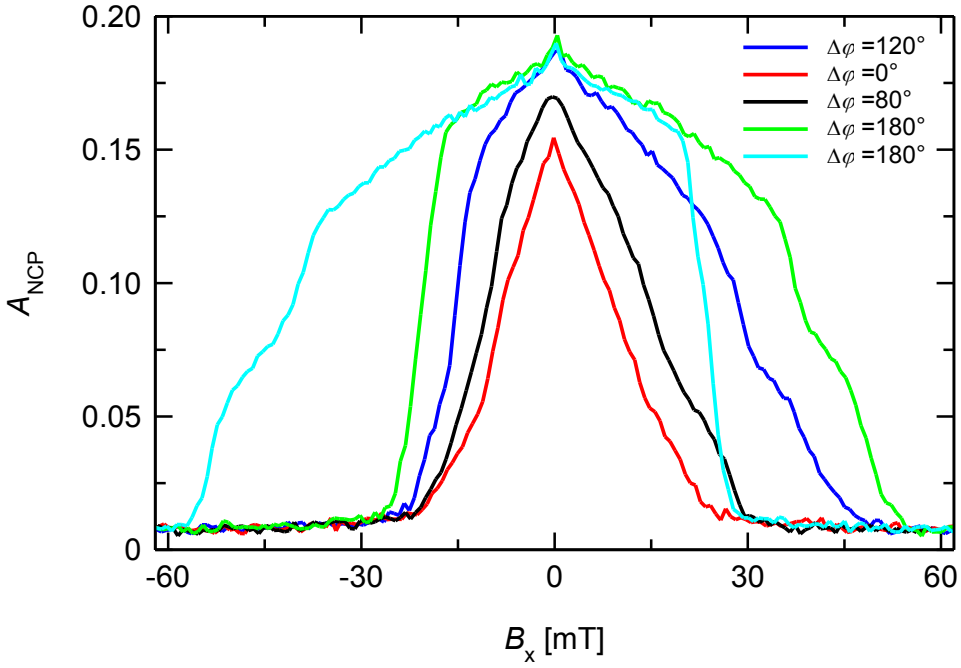

Figure 4-24 All Hanle-curves measured with 1 MHz of PM+RF modulation with the same power of excitation and the same RF amplitude but different phase $\Delta\varphi$. The different phase $\Delta\varphi$ is shown for each curve. For each curve except the cyan curve the Sweeping direction of B_x is directed from negative to positive values. The cyan curve shows the hysteresis like behavior and is swept from positive to negative values of B_x. The curves were obtained with sample #980 under excitation at 1.49 eV, detected at 1.42 eV at temperature $T = 1.8$ K.

Sample #900 also shows a widening and narrowing of the Hanle-curve in the dependence on the phase $\Delta\varphi$ but the hysteresis behavior is less pronounced. For a $f_{\mathrm{PM+RF}} = 333$ kHz the asymmetric shape is hardly visible, so that the hysteresis behavior can only be observed for $f_{\mathrm{PM+RF}} < 333$ kHz. For higher modulation frequencies only a symmetric widening and narrowing is observable.

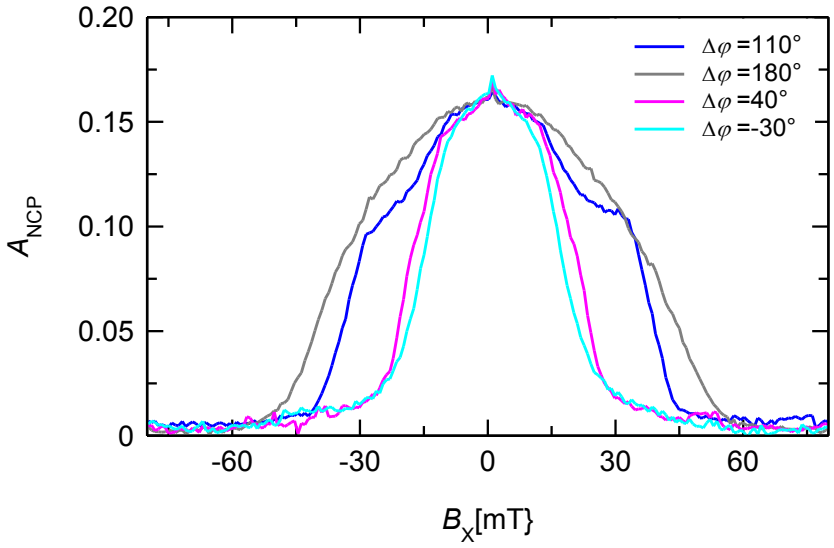

Figure 4-25 All Hanle-curves measured with 333 kHz of PM+RF modulation with the same power of excitation and the same RF amplitude but different phase $\Delta\boldsymbol{\varphi}$. The different phase $\Delta\boldsymbol{\varphi}$ is shown for each curve. The curves were obtained with sample #900 under excitation at 1.47 eV, detected at 1.34 eV at temperature $T = 1.8$ K.

If the polarization modulation has a different frequency than the RF-field modulation no phase can be defined between the two modulations and the Hanle-curve shows no influence in this case (ref. to Figure 4-26).

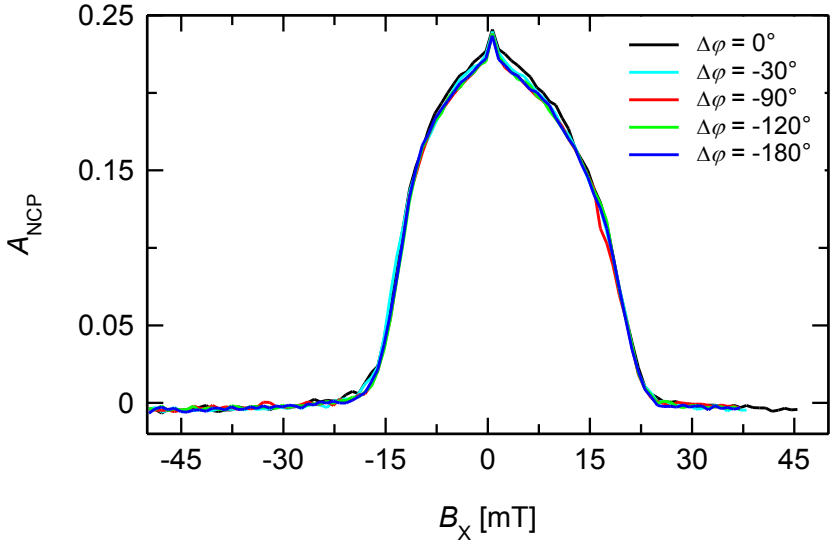

Figure 4-26 All Hanle-curves measured with 300 kHz of PM modulation and 400 kHz of RF modulation with the same power of excitation and the same RF amplitude but different phase $\Delta\boldsymbol{\varphi}$. The different phase $\Delta\boldsymbol{\varphi}$ is shown for each curve. The curves were obtained with sample #900 under excitation at 1.47 eV, detected at 1.34 eV at temperature $T = 1.8$ K.

4.4.3 Conclusions

A joint effect of RF+PM modulation has also been observed in 1976 for bulk AlGaAs crystals as a change of the Hanle-curve in small magnetic fields [162].

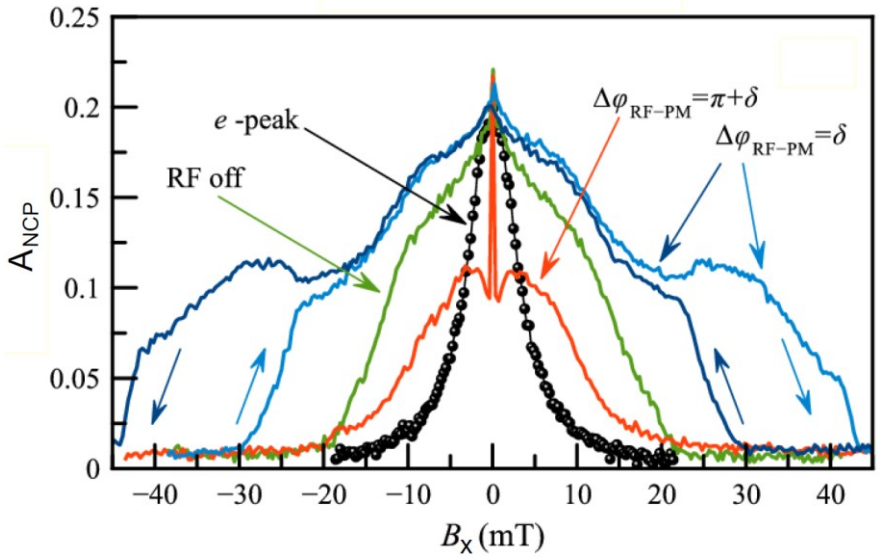

Figure 4-27 Effect of RF_z-field on Hanle-curve measured at f_{PM+RF} = 250 kHz. The dark and light blue curves are measured at application of cophased RF_z-field (Δφ=20°) with amplitude $B_{RF} = 0.5$ mT. Arrows show direction of the NCP change when the magnetic field is scanned from negative to positive values and in reverse direction. The red curve is measured at the antiphased RF_z-field (Δφ = -160°). The green curve is measured with no RF-field. The black curve is the electronic Hanle-curve. The curves were obtained with sample #980 under excitation at 1.49 eV, detected at 1.42 eV at temperature $T = 1.8$ K [167].

It has been interpreted as an effect related to nuclear polarization. The following interpretation of the role of the RF-field is based on the model of hyperfine interactions as described in [119]. In the term of the hyperfine interaction (ref. to eq.(2.20)) there is the scalar product of the nuclear spin and the electron spin. Therefore, in case of a perpendicular orientation of the nuclear spin and the electron spin, no hyperfine interaction occurs. In the Voigt geometry (as in all measurements performed), the magnetic field is perpendicular to the optical axis, so that the excited electron is oriented along the optical axis. The external field is the quantization axis for the nuclei, so that the only component of the nuclear spin that cannot be averaged to zero is directed along the external field. In such a situation a hyperfine interaction cannot occur, due to the perpendicular orientation of both spin vectors. However, a magnetic field (like the RF-field) that is directed along the optical axis and acts on the nuclei, tilts the total magnetic field for the nuclei out of the perpendicular orientation to the optical axis, which gives rise to the hyperfine interaction. The role of the RF-field depends on the phase $\Delta\varphi$ between the PM- and RF-modulation. In a situation where the Hanle-curve obtained under PM+RF-modulation is wider than a Hanle-curve obtained under pure PM, the RF-field amplifies the Knight-field (ref. to blue curve in Figure 4-27). Then, the total field $\boldsymbol{B}_{tot}^{N}$ for the nuclei is given by $\boldsymbol{B}_{tot}^{N} = \boldsymbol{B}_x + \boldsymbol{B}_e + \boldsymbol{B}_{RF}$. Due

to the constant phase $\Delta\varphi$, $\boldsymbol{B}_{\mathrm{e}}$ and $\boldsymbol{B}_{RF}$ are summarized to a an effective magnetic field $\boldsymbol{B}_{\mathrm{mod}}$ that is alternating in direction but not in amplitude for a fixed $f_{\mathrm{PM+RF}}$ and fixed $\Delta\varphi$. In a situation, where the Hanle-curve obtained under PM+RF-modulation is narrower than a Hanle-curve obtained under pure PM, the RF-field compensates the Knight-field (ref. to red curve in Figure 4-27).

In order to prove experimentally that the $\mathrm{RF_z}$ field is crucial for the effects observed, two more measurements are performed. In the first measurement the $\mathrm{RF_z}$ field is replaced by a constant magnetic field along the z-axis. In the second measurement the $\mathrm{RF_z}$ field is replaced by an RF-field along the x-axis. In both cases it is not possible to obtain similar effects as could be obtained applying the $\mathrm{RF_z}$ field. The resonances observed at large absolute values of $\mathrm{B_x}$, which were considerably magnified by the $\mathrm{RF_z}$ field cannot be explained by transitions $|+1/2\rangle \leftrightarrow |-1/2\rangle$ in nuclei of elements of the QDs under study. Quantum dots under study contain several types of nuclei (including isotopes), namely, $^{69}\mathrm{Ga}$, $^{71}\mathrm{Ga}$, $^{75}\mathrm{As}$, $^{113}\mathrm{In}$, $^{115}\mathrm{In}$, so that the variety of nuclear spin transitions which can contribute to the observed Hanle-curves is large enough. This variety is increased further in these QDs due to large quadrupole splitting of nuclear spin states which influences the energy distance of the Zeeman levels. The strain is directed along the growth axis (z-axis) that is perpendicular to B_{x}. It determines the quadrupole splitting for all the types of nuclei including their isotopes (ref. to sec. 2.1.2). Calculations show that the Zeeman splitting of states $|\pm 1/2\rangle$ is increased in this case by factor "2" in small magnetic fields and the Zeeman splitting of states $|\pm 3/2\rangle$ is strongly nonlinear [ref. to Figure 4-28] [153].

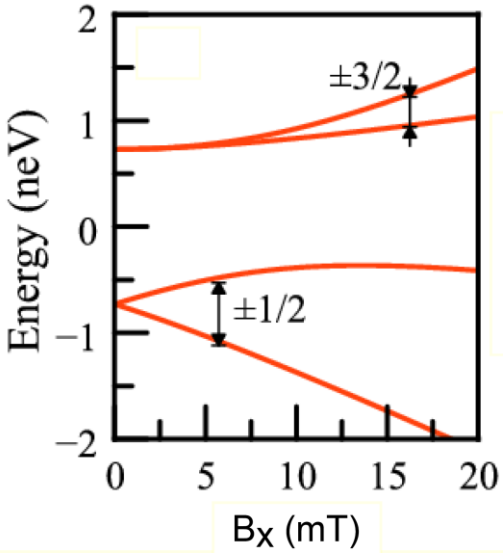

Figure 4-28 Calculated Zeeman splitting of quadrupole-affected nuclear spin states of $^{71}\mathrm{Ga}$ assuming that the quadrupole splitting is due to strain aligned along z axis, e_{zz} = 0.01 [153].

Transitions $|+1/2\rangle \leftrightarrow |-1/2\rangle$ give rise to resonances, whose magnetic field position can be calculated using relation: $\hbar\omega_{\mathrm{PM}} = 2\gamma_{\mathrm{N}}B$, where γ_{N} is the gyromagnetic ratio for nucleus N. Transitions $|+3/2\rangle \leftrightarrow |-3/2\rangle$ can also give resonances due to an admixture of $|\pm 1/2\rangle$ states in the magnetic field. The field position of the resonances however strongly depends

on quadrupole splitting. The resonances may be responsible for the wide part of Hanle-curve, since the larger magnetic field is required to split states $|\pm 3/2\rangle$. This consideration has been used for analysis of resonances observed in Hanle-curves. An example of the analysis is given in Figure 4-29. Although the amplitude of resonances cannot be uniquely determined, the fitting clearly shows that the ^{71}Ga resonance is most intensive. This conclusion is in agreement with the observation obtained previously using another technique [153].

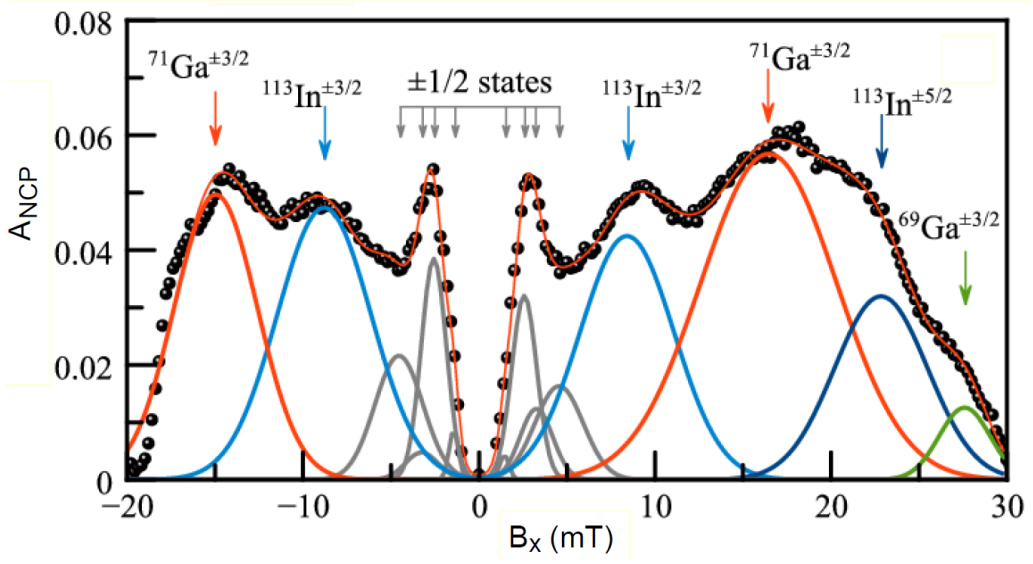

Figure 4-29 Analysis of Hanle-curve obtained by $f_{\mathrm{PM+RF}} = 100\mathrm{kHz}$. The black dotted line is the experimental data. The colored and gray Gaussian functions are the obtained fits. Detailed information about the analysis is given in the main text. The curves were obtained with sample #980 under excitation at 1.49 eV, detected at 1.42 eV at temperature $T = 1.8$ K [167].

Similar results are obtained for other frequencies of polarization modulation. Figure 4-29 shows the analysis of the Hanle-curve measured at application of the RF-field. The dip of the Hanle-curve at $B_x = 0$ is a result of a subtraction of two Hanle-curves, namely the RF+PL modulated Hanle-curve subtracted from the "electron peak". The "electron peak" is a Hanle-curve without any influence of a nuclear polarization, as explained in detail in sec. 4.3.2. The Hanle-curve that results from such a subtraction only shows effects that arise from nuclear polarization.

The central part of the Hanle-curve obtained is modeled by resonances$|+1/2\rangle \leftrightarrow |-1/2\rangle$, the wide part is modeled by resonances $|+3/2\rangle \leftrightarrow |-3/2\rangle$ for In and Ga nuclei, as well by resonances $|+5/2\rangle \leftrightarrow |-5/2\rangle$ for In nuclei. The resonance positions were considered as fitting parameters. This analysis is performed for all the experimental data obtained. To calculate the strain in the sample it is assumed that the electric field gradient is only strain induced, $V_{zz} = S_{11}\varepsilon_{zz}$ and determined by the strain ε_{zz}. S_{11} is the principal component of the so-called S tensor which can be extracted from nuclear acoustic resonances [60]. Using a cylindrically symmetric QD model [78] and the transversal isotropic approximation [172] in continuum elasticity theory, the value of the strain is estimated to be $\varepsilon_{zz} = 0.01$, which is in

good agreement with that estimated in ref. [153]. The resonance for ^{71}Ga can be identified most reliably and its magnetic field dependence (ref. to Figure 4-30) is well described by the theoretical assumptions. The least accordance to the model is given by the resonances of ^{75}Ga as shown in Figure 4-30. The problem arises from the fact that the strain is not the only reason that leads to an electric field gradient (ref. to sec. 2.1.3). Another reason for an electric field gradient is the exchange of nuclei due to the annealing process. The unit cell of GaAs shows that As has four Ga-nuclei as next neighboring nuclei. It is not possible to predict, which and how many of the four Ga-nuclei are replaced by In-nuclei during the annealing process, because the exchange is a random process. The influence of the exchanged nuclei leads to tilting of the electric field gradient relative to the external magnetic field B_x for the As-nuclei, which in turn influences the quadrupole splitting.

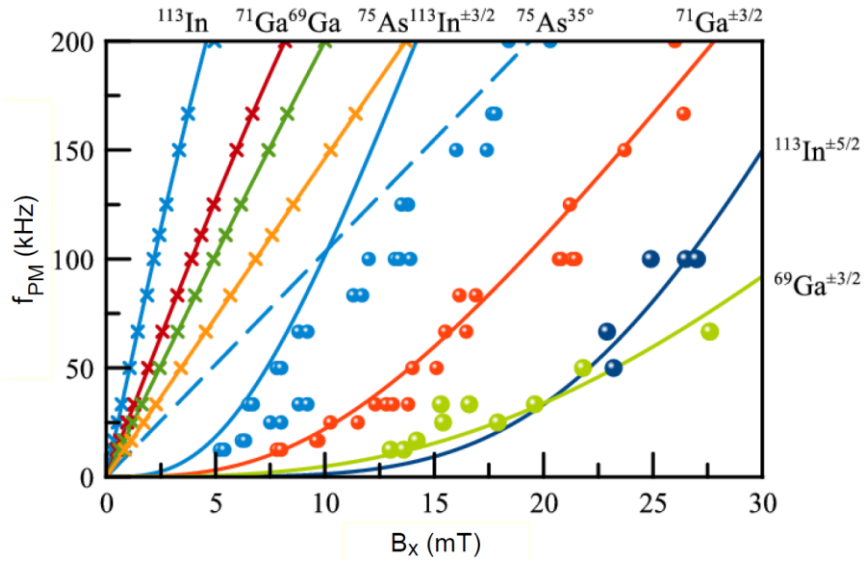

Figure 4-30 (Color online) (a) The positions of resonances $|+1/2\rangle \leftrightarrow |-1/2\rangle$ (crosses), $|+3/2\rangle \leftrightarrow |-3/2\rangle$ and $|+5/2\rangle \leftrightarrow |-5/2\rangle$ (circles) extracted from experiments. Solid lines show theoretical calculations for e_{zz} = 0.01. Dashed line is the calculated dependence for resonance $|+1/2\rangle \leftrightarrow |-1/2\rangle$ in As nuclei with one In and three Ga neighbors. The curves were obtained with sample #980 under excitation at 1.49 eV, detected at 1.42 eV at temperature $T = 1.8$ K [167].

4.5 Nuclear spin pumping under pulsed laser excitation

In contrast to all previously mentioned results, the results presented in this section are not yet published. The collected knowledge about the interaction of electron and nuclei in quantum dots during this thesis can be used to analyze the observed effects, but there are still open questions that remain. In the first part of this section Hanle-curves obtained by a CW-laser excitation and a pulsed-laser excitation will be compared (ref. to secs. 4.5.1 and 4.5.2). The second part (sec. 4.6) presents data obtained with an extended version of the excitation protocol that is used for amplified resonant pumping. The extension is a RF-coil directed along the y-axis and the possibility to show the evolution of A_{NCP} during the excitation. All measurements with pulsed laser excitation are obtained with sample #900.

4.5.1 Comparison of pulsed- and CW-laser excitation without modulation

In order to compare the two different laser types it is important to have equal framework conditions for both excitations. The external magnetic field B_x is swept in the same range with the same steps and a sweeping time t_s=10 sec/point. The sample is put into superfluid helium and the temperature of the sample is controlled by using a needle valve. By detecting the PL with a lens that is focused on one spot on the sample it is possible to always excite the same spot on the sample. One problem that appears is finding the criterion for the comparison of the excitation energy. The pulsed laser excites the sample with a short pulse (in the femtosecond range) with a high energy density. In between the excitation pulses the sample is not excited for 12.5 ns. The CW-laser excites the sample continuously with a lower energy density. One possibility for comparison of the two different laser types is to use for each laser the same time averaged excitation power. However, this comparison proves not to be suitable in our case, since excitation with the same time averaged excitation power leads to a different shape for the PL spectrum of the quantum dots. Therefore the ratio of the emission intensity from the ground-state and the excited state is different for the two lasers. A more similar condition would be a situation where the relation of the emission intensity of the ground-state and the excited states does not change due to a change of the laser. At first, the excitation power of a pulsed laser of 0.5 mW is compared with the excitation power of a CW-laser of 10 mW. In this case, the relation of the emission intensity of the ground-state and the excited states does not change due to a change of the laser (ref. to Figure 4-31)

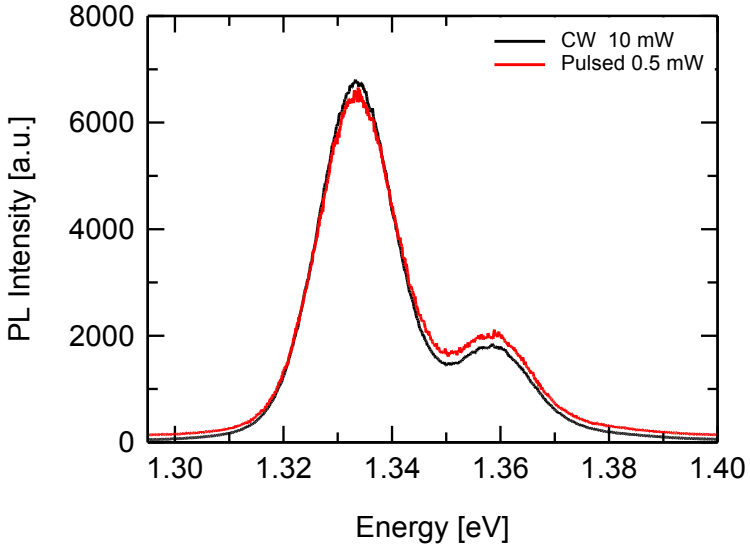

Figure 4-31 PL spectrum of sample #900 obtained be CW-laser and pulsed-laser excitation (excited at 1.47 eV) at temperature $T = 1.8$ K. Represents a weak excitation intensity with luminescence of the ground- and first excited-state of the quantum dot exciton.

Secondly, the excitation power of a pulsed laser of 10 mW is compared with the excitation power of a CW-laser of 100 mW. In this case, however, the P-shell emission of the pulsed laser excitation is more intense than the S-shell emission. It is impossible to achieve such a situation using a CW-laser excitation even under 200 mW excitation, which is the highest stable excitation power that can be applied using the CW-laser. A drop to a CW-laser excitation of 100 mW leads to nearly no change in the relation of the emission intensity of the PL. Therefore a comparison of a 10 mW pulsed laser with a 100 mW CW-laser excitation is performed.

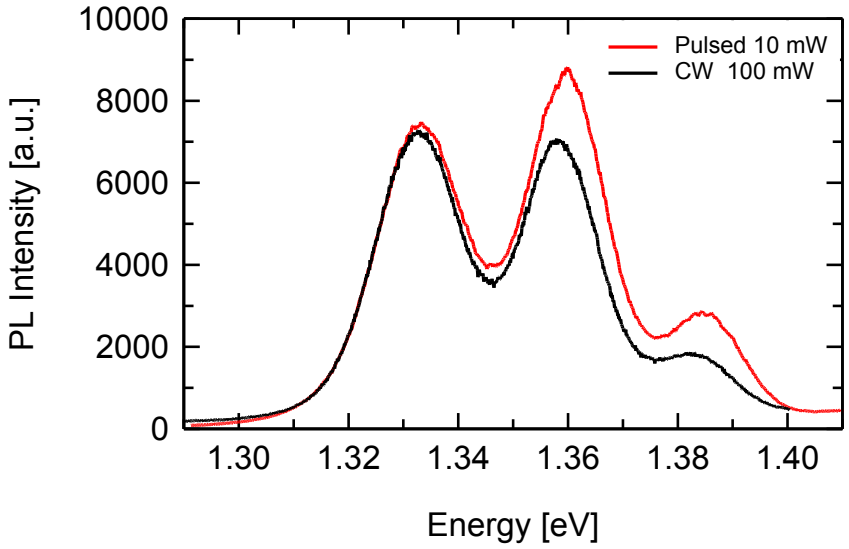

Figure 4-32 PL spectrum of sample #900 obtained be CW-laser and pulsed-laser excitation (excited at 1.47 eV) at temperature $T = 1.8\ \mathrm{K}$. Represents a strong excitation intensity with luminescence of the ground-, first and second excited-state of the quantum dot exciton.

Another problem for comparison that appears is the different spectral width of the two laser beams. The pulsed laser has a spectral width of ~ 13 nm, the CW-laser has a spectral width of ~ 1 nm. For the following experiments the width of the pulsed laser is narrowed by a grating (2000 gr/mm) and a set of razors which cuts out the unused laser light, resulting in an equal spectral width of the pulsed laser and the CW-laser.

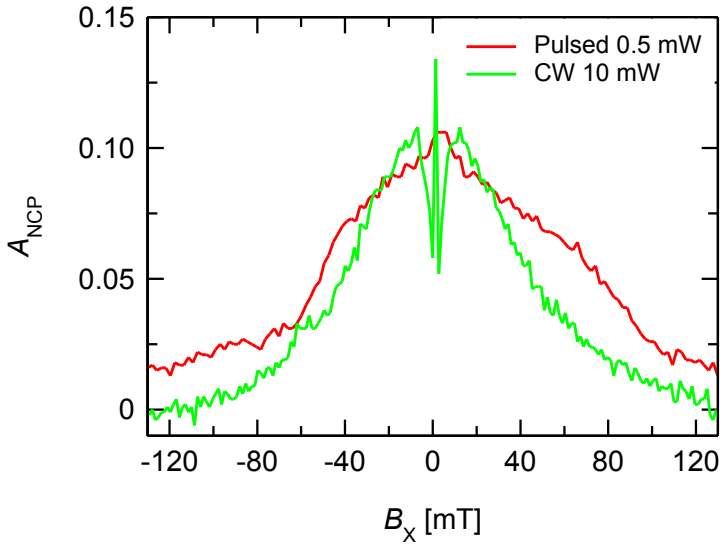

Figure 4-33 Hanle-curves obtained by CW-laser (green curve) and by pulsed-laser excitation with a constant circular polarization. The different excitation powers (values are averaged over time) are given for each curve. The curves were obtained with sample #900 under excitation at 1.47 eV, detected at 1.34 eV at temperature $T = 1.8$ K.

Two important differences can be observed in the shape of the Hanle-curve. The first observed difference is that in comparison to the excitation with a CW-laser the Hanle-curve obtained by pulsed laser excitation has no W-shape (ref. Figure 4-33 and Figure 4-34). The second observed difference is that the Hanle-curve obtained under pulsed laser excitation is asymmetric concerning the zero position of B_x in contrast to a CW-laser excitation (ref. Figure 4-33 and Figure 4-34).

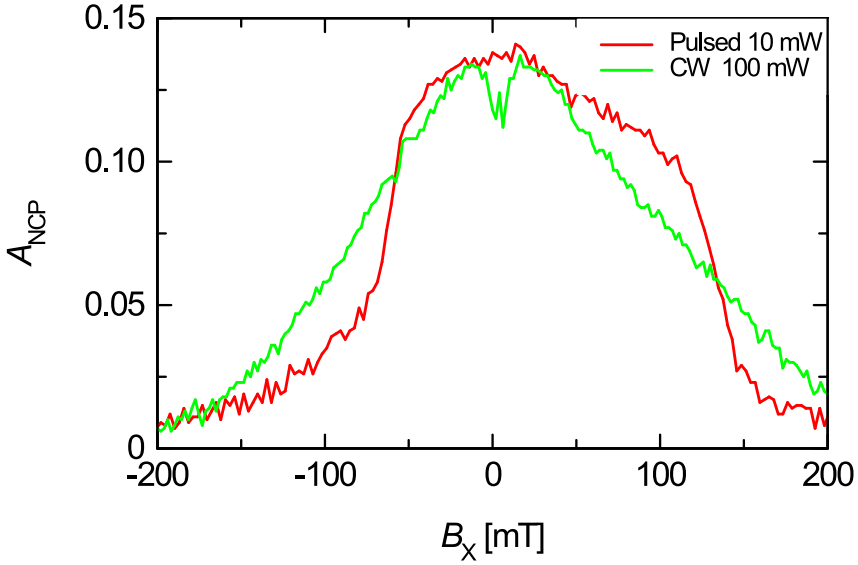

Figure 4-34 Hanle-curves obtained by CW-laser (green curve) and by pulsed-laser excitation with a constant circular polarization. The different excitation powers (values are averaged over time) are given for each curve. The curves were obtained with sample #900 under excitation at 1.47 eV, detected at 1.34 eV at temperature $T = 1.8$ K.

4.5.2 Conclusions

The W-structure is a mark of a nuclear polarization that appears along the optical axis due to the Knight-field (ref. to sec. 4.2.4.). The missing of the W-structure could indicate a missing of such a nuclear polarization. In previous [153] and current studies (ref. to sec. 4.4) spin $|\pm 1/2\rangle$ nuclei are responsible for a nuclear polarization that occurs in small fields of $B_{\mathrm{x}} \leq \sim 20\ \mathrm{mT}$. These spin states show a faster buildup and decay time (ref. to sec. 4.3.2, Figure 4-15, 4.1.2 and 4.1.3) than spin states $I_z \geq |\pm 3/2\rangle$. Another point that should be taken into account is that in ref. [40], a single electron could increase the decay time of nuclear polarization by several orders of magnitude. The last point that is to mention is the fast carrier relaxation to the ground-state in quantum dots on the order of tens of picoseconds [173, 174] and the fast recombination of about 1 ns [175]. That leads to the statement that a carrier photoexcited into the wetting layer would recombine within $\sim$1 ns. This information can be adapted to the studied system of n-doped quantum dots that are excited with a pulsed laser with circularly polarized light.

On average every quantum dot of the self-organized ensemble is occupied by one electron. In combination with a pulsed-laser excitation (which excites the sample every 12.5 ns with pulse duration of $\sim$125 fs) the quantum dot is occupied with one electron for $\sim$11 ns. The situation is different compared to a CW-laser excitation. In this context it would be useful to make a more detailed estimation about the time of excitation events that take place for a moderate CW-laser excitation than in sec. 4.3.2, where it is estimated to be $\sim 3\ \mathrm{ns}$. So if a single electron really can increase the decay time of nuclear polarization it could cancel nuclear polarization of spin states $|\pm 1/2\rangle$ (in the worst case) when during an excitation the quantum dots are mainly occupied only by the resident electron. It is still remarkable that an excitation event that takes place every $\sim$11 ns creates a different nuclear polarization than a excitation event that takes place every $\sim 3\ \mathrm{ns}$. The nanosecond timescale indicates that the depolarization mechanism is not a dipole-dipole interaction of nuclear spin (typical timescale $\sim 10^{-4}$ s) but a hyperfine interaction (typical timescale $\sim 10^{-11}$ s). Due to the scalar product $I \cdot S$ in the hyperfine term this interaction is absent when the electron spin *S*=0. This is the case when the quantum dot is occupied by the resident electron and the photoexcited electron in the ground-state of the quantum dot. Such a situation can be interpreted as a perturbation of the hyperfine interaction, which is periodic in the case of a pulsed laser excitation (every 12.5 ns) and random in the case of a CW-laser excitation. A further study of such fast depolarization mechanism for the nuclear spin system would be interesting.

The asymmetry of the Hanle-curve obtained by a pulsed-laser could be a sign of a tilted sample (relative to B_{x}) [123] or a sign of a nuclear polarization of nuclear spin states $I_z \geq |\pm 3/2\rangle$, that are stabilized by quadrupole interactions (ref. to sec. 4.4.3). A tilted sample would give also an asymmetric shape with a CW-laser excitation, which is not the case. So, the only explanation left is a polarization of nuclear spin states $I_z \geq |\pm 3/2\rangle$. But in

contrast to a smooth decay of A_{NCP} for a CW-laser excitation (where also nuclear spin states $I_z \geq |\pm 3/2\rangle$ are polarized) the change of A_{NCP} shows a jump up behavior for a pulsed-laser excitation. A similar abrupt behavior of the Hanle-curve without a W-structure was observed by Krebs [146], but these measurements are performed on single p-doped self-assembled InAs/GaAs quantum dots by observing µ-spectroscopy of individual quantum dots excited quasiresonantly by a CW-TiSa laser. Such a system is comparable to single n-doped quantum dots excited with a pulsed laser under the aspect that during the main time of excitation a single electron occupies the quantum dot. The feature observed in [146] was identified by a transverse component of nuclear polarization (relative to B_{x}). In our case the nuclear spin states $I_z \geq |\pm 3/2\rangle$ also create a transverse component of nuclear polarization, but further studies are required to support this statement.

4.6 Modulated excitation with pulsed laser

For the following experiments a pulsed laser was used for excitation instead of a CW-laser. In the experiments presented first, polarization modulated excitation was synchronized with RF excitation. Afterwards, experiments with pure polarization modulated excitation will be shown and compared with PM+RF modulation experiments for some regions of the Hanle-curve. Averaged over time the excitation density is 10 mW for every experiment. The RF-coils used along the y- and z-axis in these experiments are split coils with thirty turns on each side with a total diameter of $\sim 1\ \mathrm{cm}$ (ref. to Figure 0-5). In analogy to sec. 4.4.2 the settings for the modulation are the same, unless otherwise mentioned. The aim of the following section is to show the development of A_{NCP} at a fixed modulation frequency of $f_{\mathrm{mod}} = 1\ \mathrm{kHz}$. The modulation frequency of $f_{\mathrm{mod}} = 1\ \mathrm{kHz}$ is pointed out exemplarily for an effect that is present in the range of $f_{\mathrm{mod}} = 0.5\ \mathrm{kHz}$ to approximately $f_{\mathrm{mod}} = 40\ \mathrm{kHz}$. The excitation time for one polarization is $\tau_{\mathrm{exc}} = 500\ \mu s$.

4.6.1 Polarization modulated excitation synchronized with RF excitation (PM+RF)

In addition to the polarization modulation a sinusoidal RF-field $U_{\mathrm{RF}} = U_0 \cdot \sin(\omega_{\mathrm{PM}} t + \Delta\varphi)$ synchronized with the polarization modulation and directed along the z-axis with $\mathrm{RF_z}$ being parallel to the optical-axis and perpendicular to B_{x}, or along the y-axis with $\mathrm{RF_y}$ being perpendicular to the optical-axis and perpendicular to B_{x} is applied. For both RF-fields the phase $\Delta\varphi = 0°$ and both configurations are studied with sample #900. Due to the use of the PicoHarp and a new software it is possible to detect the development of the Hanle-curve during the modulation. The change of A_{NCP} during the modulation period is shown in Figure 4-35 for different B_{x}.

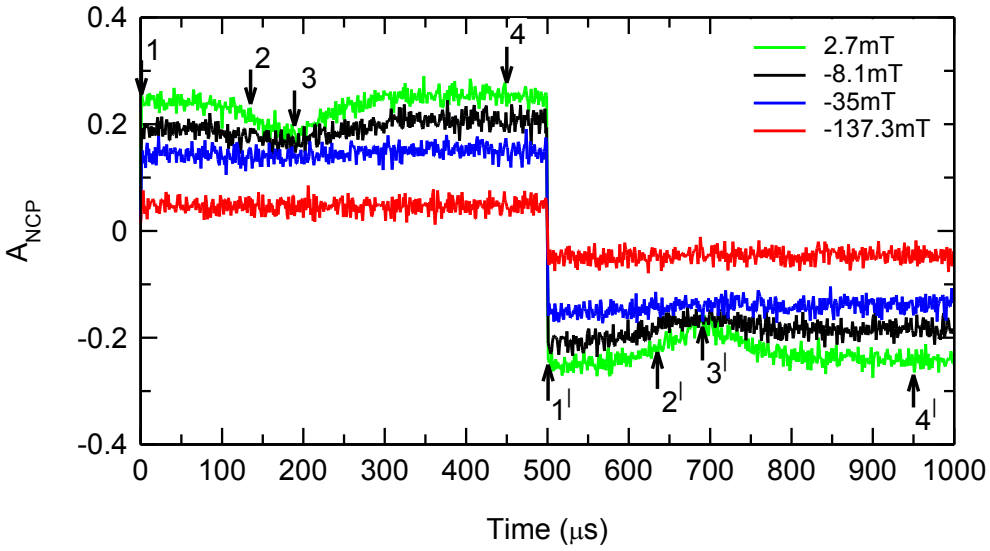

Figure 4-35 Development of A_{NCP} for different magnetic fields (indicated at each curve) obtained by $\mathrm{PM} + \mathrm{RF_y}$. The arrows point at characteristic positions during the excitation (No.1 = 1 µs, No.2 = 135 µs, No.3 = 190 µs, No.4 = 450 µs, No.1' = 503 µs, No.2' = 637 µs, No.3' = 692 µs, No.4' = 950 µs). The curves were obtained with sample #900 under excitation at 1.47 eV, detected at 1.34 eV at temperature $T = 1.8$ K.

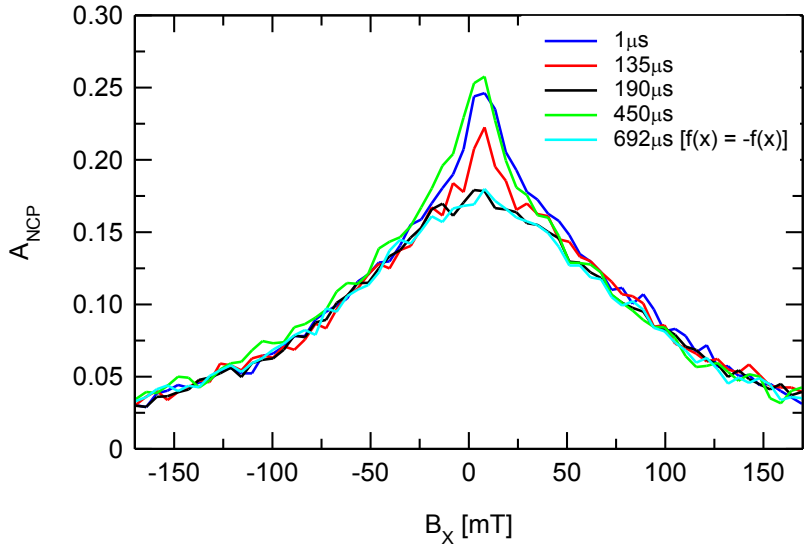

Figure 4-36 Hanle-curve measurements obtained by $\mathrm{PM} + \mathrm{RF_y}$ for the positions No.1, No.2, No.3, No.4 and No.3' of the modulated laser beam (ref. to Figure 4-35). The A_{NCP} values of the cyan color curve are multiplied by -1 for a better comparison to the other curves. The curves were obtained with sample #900 under excitation at 1.47 eV, detected at 1.34 eV at temperature $T = 1.8$ K.

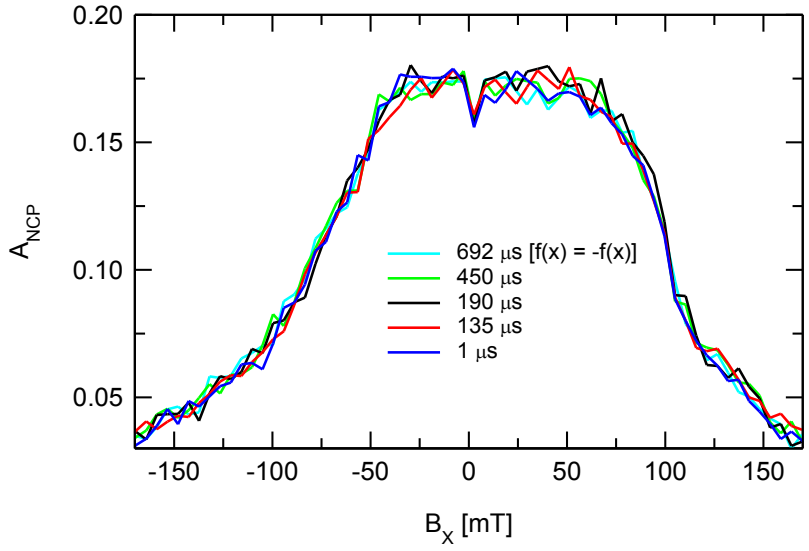

Figure 4-37 Hanle-curve measurements obtained by $\mathrm{PM} + \mathrm{RF_z}$ for the positions No.1, No.2, No.3, No.4 and No.3' of the modulated laser beam (ref. to Figure 4-35). The A_{NCP} values of the cyan color curve are multiplied by -1 for a better comparison to the other curves. The curves were obtained with sample #900 under excitation at 1.47 eV, detected at 1.34 eV at temperature $T = 1.8$ K.

The time resolution in the following experiments is 1 µs. However the presented curves always show a signal integrated over 10 µs due to the noise in the signal. Figure 4-38 compares the signal for the first µs of the modulation and the first ten µs of modulation. The shape of the curves is identical except that the curve that has been obtained without averaging the signal shows more noise. An averaging over 10 µs is sufficient to lower the experimental noise and is still short enough to analyze the dynamics of the system.

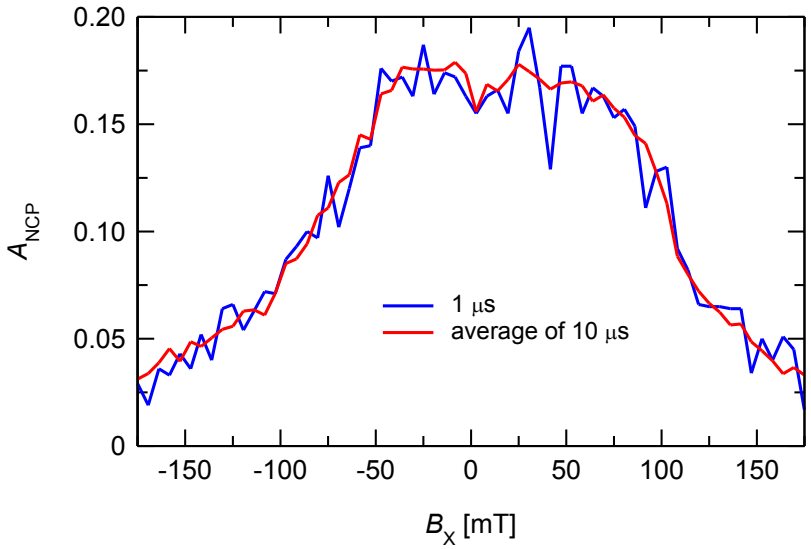

Figure 4-38 Comparison of the same experimental data but different averaging in time. The curves were obtained with sample #900 under excitation at 1.47 eV, detected at 1.34 eV at temperature $T = 1.8$ K.

For $\mathrm{PM} + \mathrm{RF_y}$ modulation the behaviour of A_{NCP} in the range of -5.6 mT to 10.5 mT differs from its behavior in the other range of B_{x}. In the following text, such regions will be called "regions of interest".

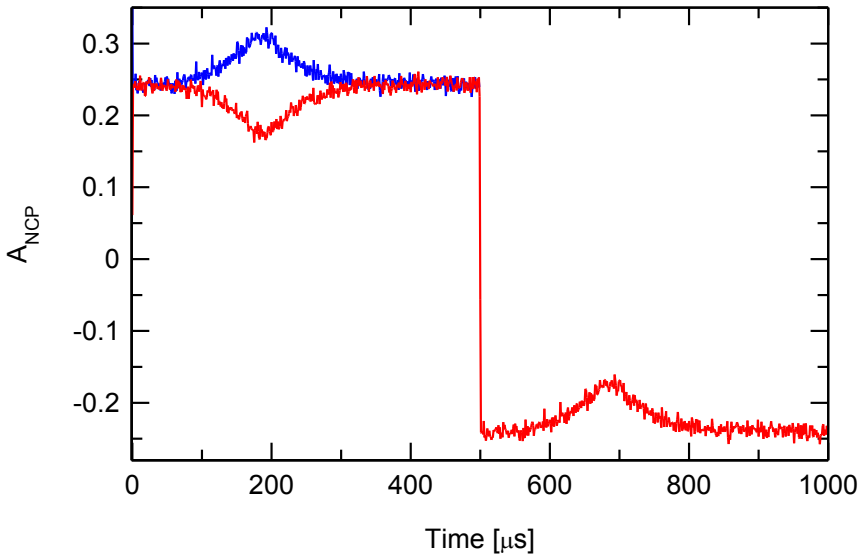

Figure 4-39 The red curve gives the development of A_{NCP} at $B_{\mathrm{x}} = 2.7\ \mathrm{mT}$ obtained by $\mathrm{PM} + \mathrm{RF_y}$ modulation. For a better comparison of the dip position (one in each polarization of excitation) the red curve has been shifted backwards by 500 µs and to the positive values of A_{NCP} (blue curve). The curves were obtained with sample #900 under excitation at 1.47 eV, detected at 1.34 eV at temperature $T = 1.8\ \mathrm{K}$.

Figure 4-39 shows drops of A_{NCP} during the modulation which reaches the minimum position at about ~189 µs and ~684 µs in the region of interest. There is one drop in each polarization of excitation and the distance in time of these drops is approximately 500 µs. The position of the drops is the same within each polarization. The whole region of B_{x} at $\mathrm{PM} + \mathrm{RF_z}$ modulation (averaged over 10 µs) shows no change in A_{NCP} during the modulation period (ref. to Figure 4-37), because of the bad signal to noise ratio. As shown in Figure 4-40 an averaging over 100 µs leads to a increase of the signal to noise ratio so that the observation of a variation of A_{NCP} during the modulation period becomes possible.

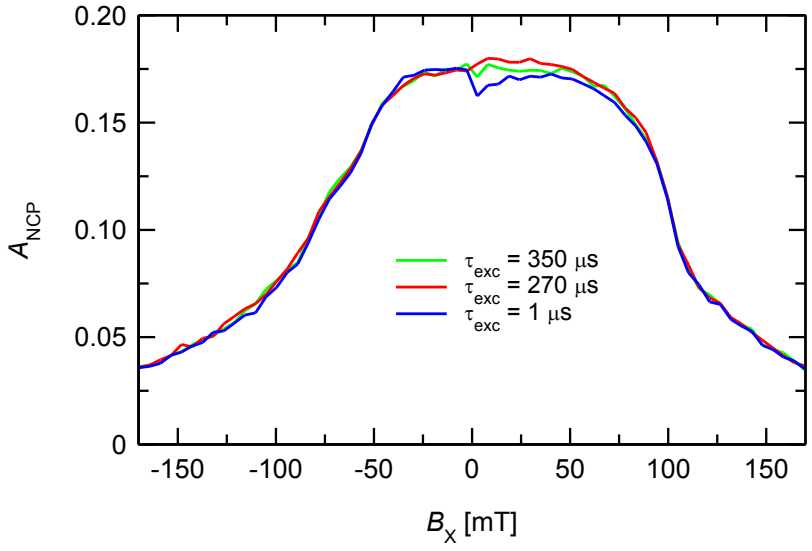

Figure 4-40 Hanle-curve measurements obtained by $\mathrm{PM} + \mathrm{RF_z}$ for different times of the excitation (indicated at each curve). In contrast to Figure 4-37 the presented curves are averaged over 100 µs. The curves were obtained with sample #900 under excitation at 1.47 eV, detected at 1.34 eV at temperature $T = 1.8$ K.

Within the region of interest, which in this case reaches from B_x~0 mT to B_x~70 mT, a development of A_{NCP} is detectable. The changing of A_{NCP} in time is most present in the region of B_x~0 mT to B_x~11 mT. This is approximately the same region of interest like for $\mathrm{PM} + \mathrm{RF_y}$ modulation. It seems obvious to compare the similar regions of interest for $\mathrm{PM} + \mathrm{RF_z}$, $\mathrm{PM} + \mathrm{RF_y}$ and PM modulation to see the development of A_{NCP} during the time of modulation (ref. to Figure 4-41).

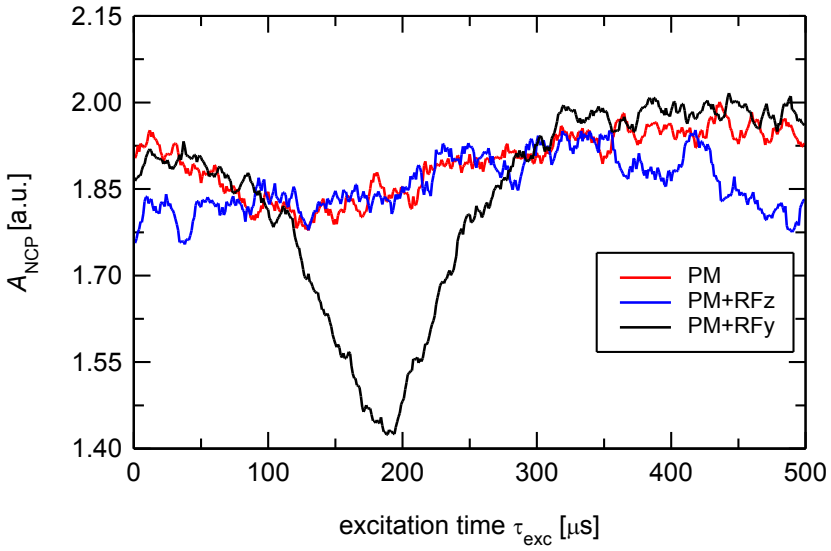

Figure 4-41 Time dependence of A_{NCP} for "the region of interest", that contains of $B_{\mathrm{x}} = -5.6$ mT to 10.5 mT. This region is detected for three different modulations, namely the pure polarization modulation (PM), the polarization modulation with $\mathrm{RF_y}$ excitation ($\mathrm{PM} + \mathrm{RF_y}$) and polarization modulation with $\mathrm{RF_z}$ excitation ($\mathrm{PM} + \mathrm{RF_z}$). The curves were obtained with sample #900 under excitation at 1.47 eV, detected at 1.34 eV at temperature $T = 1.8$ K.

To have a proof that the development of A_{NCP} for the different excitation protocols is not only an effect of averaging of the Hanle-curve but a "true" effect that is only present in "the region of interest" the same process of analyzing the data is obtained for a different region of the Hanle-curve. The new region is given by $B_{\mathrm{x}} = 140\ \mathrm{mT}$ to $123.9\ \mathrm{mT}$, which has the same width as "the region of interest".

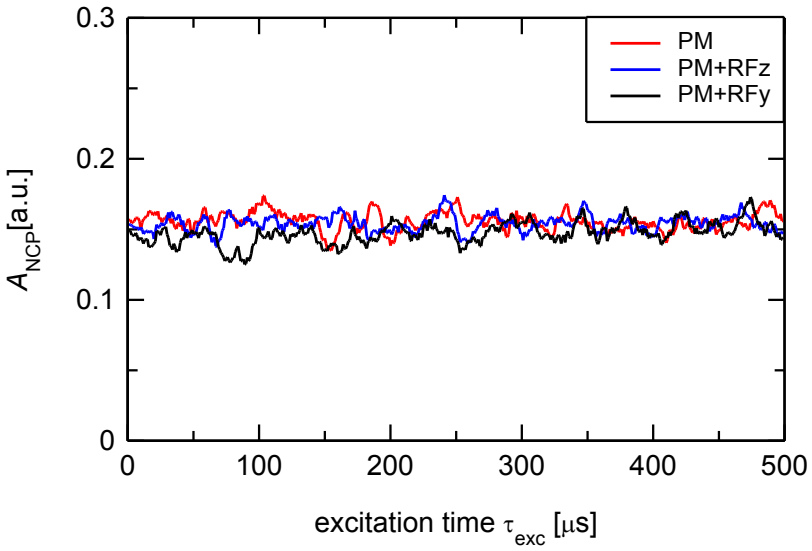

Figure 4-42 Time dependence of A_{NCP} for the region of $B_{\mathrm{x}} = 140\ \mathrm{mT}$ to $123.9\ \mathrm{mT}$. This region is detected for three different modulations, namely the pure polarization modulation (PM), the polarization modulation with $\mathrm{RF_y}$ excitation ($\mathrm{PM + RF_y}$) and polarization modulation with $\mathrm{RF_z}$ excitation ($\mathrm{PM + RF_z}$). The curves were obtained with sample #900 under excitation at 1.47 eV, detected at 1.34 eV at temperature $T = 1.8\ \mathrm{K}$.

Figure 4-42 shows no dependence of A_{NCP} during the different modulation protocols even though the analysis is the same as for the "region of interest".

4.6.2 Conclusions

The change of A_{NCP} for $\mathrm{PM + RF_y}$ modulation appears in a region of about $-25\ \mathrm{mT} \leq B_{\mathrm{x}} \leq 25\ \mathrm{mT}$. The modulation protocol is the same as used for "amplified resonant pumping" (ref. to sec. 4.4.2) except that the RF-coil is directed along the y-axis and the excitation laser is a pulsed laser. For the principle of an amplified resonant pumping of nuclear spins it should make no difference whether the RF-coils are directed along the y-axis or the z-axis, because both of these axes are perpendicular to the applied field B_{x}. Experiments however show that there is a difference. The DNP, obtained with the pulsed laser excitation, differs from the results obtained by CW-laser excitation even if the excitation protocol for both excitation types is the same (compare secs. 4.4.2. and 4.6.1). The lack of a consistent theory of the electron-nuclei interaction in strained QD's that is perturbed by photoexcited electrons is a general problem that is not solved up to date. But a promising model ("graded box" model)

that is usable for both types of excitation (CW- and pulsed-excitation) is given in [176]. The graded box model describes a QD system that consists of ∼100 nuclei and one resident electron in the ground-state of the QD. This amount of nuclei is sufficient to reproduce the interaction of the resident electron with the nuclei-spin bath including the interaction of the nuclear fluctuation field $\boldsymbol{B}_{\mathrm{NF}}$. The results of the graded box model in [176] are useful to reproduce the DNP of a real QD consisting of $\sim 10^5$ nuclei and one resident electron. Up to now only the results of $\mathrm{PM} + \mathrm{RF_y}$ under pulsed laser excitation can be reproduced by the graded box model in [176]. For a $\mathrm{PM} + \mathrm{RF_y}$ modulation under pulsed laser excitation the graded box model assumes a nuclear polarization along the optical axis (z-axis) that alternates with a frequency equal to the modulation frequency f_{mod} from negative to positive values of $B_{\mathrm{N,z}}$ as the only present nuclear polarization. The resulting magnetic field of this nuclear polarization stabilizes the electron spin along the optical axis which leads to an increase of A_{NCP}. This stabilization effect is only present if the magnitude of $B_{\mathrm{N,z}}$ exceeds the magnitude of the nuclear fluctuation field $\boldsymbol{B}_{\mathrm{NF}}$. The case of an exceeding magnitude of $\boldsymbol{B}_{\mathrm{NF}}$ in comparison to the magnitude of $B_{\mathrm{N,z}}$ is indicated by a lowering of A_{NCP}, because in this case the precession of the electron spin is mainly along a different direction than the z-axis, which leads to a decrease of the z-component of the electron spin. Figure 4-35 shows that at $\sim 190\ \mu s$ and $\sim 692\ \mu s$ of one modulation period a minimum value of $B_{\mathrm{N,z}}$ appears. In sec. 4.1.2 the magnitude of the nuclear fluctuation field $\boldsymbol{B}_{\mathrm{NF}}$ is estimated to be $\sim 25\ \mathrm{mT}$. The magnitude of $B_{\mathrm{N,z}}$ needs to be larger than this value to be the dominant magnetic field for the electron and support a stabilization of the electron spin along the z-axis. The good agreement of experimental results and the graded box model give the reason for the assumption that the graded box model can be further developed to reproduce the dynamic of $\mathrm{PM} + \mathrm{RF_z}$ and PM under pulsed laser excitation.

The nuclear spin states that are responsible for nuclear polarization along the z-axis under $\mathrm{PM} + \mathrm{RF_y}$ modulation can be identified as follows: If the modulation frequency is equal to the Larmor precession of the polarized nuclei, like it is for the effect of resonant pumping of the nuclear spin (ref. to sec. 4.4.3), this would give a Larmor precession of 1 kHz in a magnetic field of $-25\ \mathrm{mT} \leq B_{\mathrm{x}} \leq 25\ \mathrm{mT}$. Such small Larmor frequencies can only be obtained for strong quadrupole influenced nuclear spin states $I \geq 3/2$ (ref. to Figure 4-43).

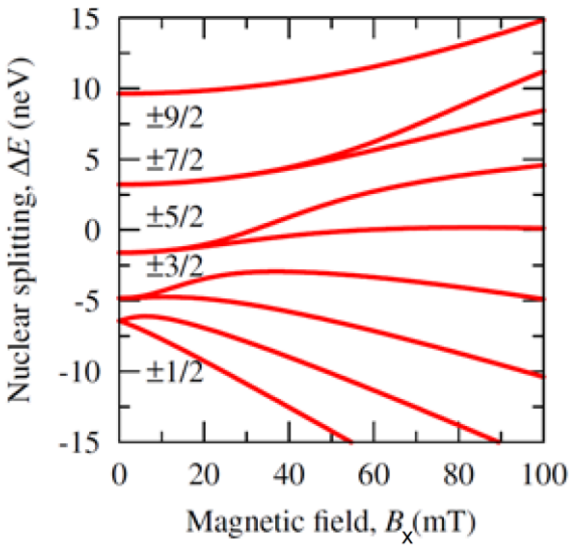

Figure 4-43 Calculation of Zeeman splitting influenced by quadrupole interaction. The calculation is based on a quantum dot model where the strain is directed only along the growing direction $\boldsymbol{q_{zz} = S_{11}\epsilon_{zz}}$ with $\boldsymbol{\epsilon_{zz} = 0.01}$ [167].

A closer identification of the nuclear spin states that are responsible for nuclear polarization along the z-axis is not possible. Further theoretical studies on the experimental data are required.

5 Summary

Nuclei and electrons trapped in quantum dots create a strongly interacting spin system due to the strong localization of electrons in quantum dots. Due to strain in self-assembled (In,Ga, As)GaAs quantum dots quadrupole interactions appear which have a significant influence on the nuclear spin system. Therefore it is no longer possible to describe the nuclear spin system as one system with certain characteristics like a buildup time and decay time. Instead, in the case of strain the nuclear spin system can be separated into two subsystems, one with a spin states $|\pm 1/2\rangle$ which is weakly influenced by quadrupole interactions and the other with a spin states $I_z \geq |\pm 3/2\rangle$ which is strongly influenced by quadrupole interactions. Each subsystem possesses different dynamics: while the buildup and decay time of spin $|\pm 1/2\rangle$ states are almost equal (approximately 5 ms) to each other, the buildup and decay time of spin states $I_z \geq |\pm 3/2\rangle$ differ widely and have opposite dependence on magnetic field strength. Furthermore, the magnitude of this subsystem with spin states $I_z \geq |\pm 3/2\rangle$ increases significantly with applied field strength. Therefore one can subdivide the Hanle-curve in two parts depending on the magnitude of B_x. For large external magnetic fields ($\sim B_\mathrm{x} \geq 20\ \mathrm{mT}$), the Hanle-curve is dominated by the dynamics of spin states $I_z \geq |\pm 3/2\rangle$, for small values $\sim B_\mathrm{x} \leq 20\ \mathrm{mT}$ the influence of spin states $|\pm 1/2\rangle$ is dominant. In small B_x fields, the effect of the nuclear fluctuation field $\boldsymbol{B}_\mathrm{NF}$ is observable as well. $\boldsymbol{B}_\mathrm{NF}$ is a typical feature of nanostructures which on the one hand possess an amount of nuclei that is small enough so that the random orientation of unpolarized nuclei is not averaged to zero. On the other hand the amount of unpolarized nuclei is large enough to create a magnetic field that changes randomly in direction.

The analysis of experimental data has confirmed the prediction of ref. [33] about the significant influence of $\boldsymbol{B}_\mathrm{NF}$ on the electron spin due to the strong localization of the electron in quantum dots. The magnitude of the Knight-field in the studied quantum dots is $\sim 1\ \mathrm{mT}$ and enables an Overhauser-field $\boldsymbol{B}_\mathrm{N}$ due to nuclear polarization at $B_\mathrm{x} = 0\ \mathrm{mT}$ along the optical-axis (z-axis) with a magnitude of $\boldsymbol{B}_\mathrm{N} = 200\ \mathrm{mT}$. As long as an angular momentum is initialized continuously in the system by circularly polarized light, it is impossible to suppress the orientation of the nuclear spin system neither by a continuous excitation with a broadband RF-field nor by a fast changing excitation of $\sigma^+ \text{ and } \sigma^-$ polarized light.

The most surprising result is the fast decay time of nuclear polarization. An interruption of the excitation beam on a nanosecond scale leads to a noticeable decay of nuclear polarization. As a result Hanle-curves can be obtained with short excitation pulses without a noticeable nuclear polarization. This fast decay mechanism is present for a system where the nuclear spins interact with a single electron. In relation to this phenomenon strong differences for the nuclear polarization are detected when either pulsed- or CW-lasers are used for excitation due to the short excitation time in relation to the repetition rate of the pulsed-laser. In the literature one can hardly find a trace about such fast decay mechanism so further study is necessary. A new effect of resonant pumping of nuclear states in quantum dots is observed, where a pure polarization modulation influences mainly the spin

$I_z = |\pm 1/2\rangle$ states. An additional RF-field along the optical axis considerably enhances the polarization of $I_z \geq |\pm 3/2\rangle$ states, which leads to a hysteresis- like behavior of the Hanle-curve. The resonant pumping of nuclear states can also be interpreted as a coherent precession of nuclear spins which have a Larmor precession frequency equal to the modulation frequency.

Bibliography

[1] "www.Nobelprize.org," [Online]. Available: http://www.nobelprize.org/nobel_prizes/physics/laureates/1902/.

[2] P. Zeeman, *The Effect of Magnetisation on the Nature of Light Emitted by a Substance*, Nature, 55 347 (1897).

[3] N. Bohr, *The Spectra of Helium and Hydrogen*, Nature, 92 231-232 (1913).

[4] A. Sommerfeld, *Zur Quantentheorie der Spektrallinien*, Annalen der Physik, pp. 1-94, **356** 17 (1916).

[5] A. Sommerfeld, *Annalen der Physik,* pp. 125-167, **356** 17 (1916).

[6] W. Gerlach and O. Stern, *Der experimentelle Nachweis der Richtungsquantelung im Magnetfeld*, Z. Phys., **9** 349 (1922).

[7] W. Pauli, *Über den Zusammenhang des Abschlusses der Elektronengruppen im Atom mit der Komplexstruktur der Spektren*, Zeitschrift für Physik, pp. 765-783, **31** 1 (1925).

[8] I. I. Rabi, S. Millman and P. Kusch, *The Molecular Beam Resonance Method for Measuring Nuclear Magnetic Moments. The Magnetic Moments of 3Li6, 3Li7 and 9F19*, Phys. Rev. , **55** 526-535 (1939).

[9] I. I. Rabi, "Nobelprize.org," (1944). [Online]. Available: http://www.nobelprize.org/nobel_prizes/physics/laureates/1944/rabi-lecture.html.

[10] F. Bloch and E. M. Purcell, "Nobelprize.org," (1952). [Online]. Available: http://www.nobelprize.org/nobel_prizes/physics/laureates/1952/.

[11] R. Ernst, "Nobelprize.org," (1991). [Online]. Available: http://www.nobelprize.org/nobel_prizes/chemistry/laureates/1991/perspectives.html .

[12] P. C. Lauterbur and P. Mansfield, "Nobelprize.org," (2003). [Online]. Available: http://www.nobelprize.org/nobel_prizes/medicine/laureates/2003/.

[13] A. Kastler, "Nobelprize.org," (1966). [Online]. Available:

http://www.nobelprize.org/nobel_prizes/physics/laureates/1966/kastler-lecture.html.

[14] M. Abraham, M. A. H. McCausland and F. N. H. Robinson, *Dynamic Nuclear Polarization*, Phys. Rev. Lett.*,* **2** 449-451 (1959).

[15] E. A. Chekhovich, K. V. Kavokin, J. Puebla, A. B. Krysa, M. Hopkinson, A. D. Andreev, A. M. Sanchez, R. Beanland, M. S. Skolnick and A. I. Tartakovskii, *Inverse NMR spectra of strained quantum dots*, Nature Nanotechnology, **7** 646-650 (2012).

[16] M. N. Makhonin, E. A. Chekovich, P. Senellart, A. Lamaître, M. S. Skolnick and A. I. Tartakovskii, *Optically tunable nuclear magnetic resonance in a single quantum dot*, Phys. Rev. B, **82** 161309 (2010).

[17] J. E. Lilienfeld, *Method and apparatus for controlling electric currents*. USA Patent US1745175 (A), (1930).

[18] J. Bardeen and W. H. Brattain, *The Transistor, A Semi-Conductor Triode*, Phys. Rev. *,* **74** 230-231 (1948).

[19] J. Bardeen, W. H. Brattain and W. B. Shockley, "Nobelprize.org," (1956). [Online]. Available: http://www.nobelprize.org/nobel_prizes/physics/laureates/1956/.

[20] "Free Info Society," [Online]. Available: http://www.freeinfosociety.com/electronics/schemview.php?id=1924.

[21] L. G. Gref, The Rise and Fall of American Technology, New York: Algora Publishing, (2009).

[22] P. Rechenberg and G. Pomberger, Informatik-Handbuch, Wien: Carl Hanser Verlag, 2002.

[23] "www.ni.com," National Instruments, (2012). [Online]. Available: http://www.ni.com/white-paper/8564/en/.

[24] O. Wechsler, *Original 45nm Intel Core Microarchitecture*, Intel Technology Journal*,* Vol.**12**, Issue 3.

[25] M. Fuechsle, J. A. Miwa, S. Mahapatra, H. Ryu, S. Lee, O. Warschkow, L. C. L. Hollenberg, G. Klimeck and M. Y. Simmons, *A single-atom transistor*, Nature Nanotechnology*,* **7** 242-246 (2012).

[26] T. Schimmel, F. Xie and C. Obermair, *Gate-kontrollierter atomarer Schalter*. Deutsches Patent- und Markenamt Patent DE102005041648A1, (2006).

[27] L. De Broglie, Nobel Lectures, Physics 1922-1941, Amsterdam: Elsevier Publishing Company, (1965).

[28] A. Fert, "www.Nobelprize.org," (2007). [Online]. Available: http://www.nobelprize.org/nobel_prizes/physics/laureates/2007/fert-lecture.html.

[29] "www.Nobelprize.org," (2007). [Online]. Available: http://www.nobelprize.org/nobel_prizes/physics/laureates/2007/press-ty.html.

[30] D. D. Awschalom and M. E. Flatté, *Challenges for semiconductor spintronics*, Nature, 3 153-159 (2007).

[31] A. Raab, R. T. Lechner and G. Springholz, *Growth temperature and coverage dependence of vertical and lateral ordering in self-assembled PbSe quantum-dot superlattices,* Phys. Rev. B, **67** 165321 (2003).

[32] K. A. Sablon, *Ellipsoidal InAs Qauntum Dots,* Nanoscale Research Letters, **4** 1256-1256 (2009).

[33] R. Hanson, L. P. Kouwenhoven, J. R. Petta, S. Tarucha and L. M. K. Vandersypen, *Spins in few-electron quantum dots*, Rev. Mod. Phys., **79** 1217-1265 (2007).

[34] D. Loss and D. P. DiVincenzo, *Quantum computation with quantum dots*, Phys. Rev. A, **57** 120-126 (1998).

[35] D. D. Awschalom, D. Loss and N. Samarth, Semiconductor Spintronics and Quantum Computation, Berlin: Springer-Verlag Berlin Heidelberg, (2002).

[36] A. V. Khaetskii, D. Loss and L. Glazman, *Electron Spin Decoherence in Quantum Dots due to Interaction with Nuclei,* Phys. Rev. Lett.*,* **88** 186802 (2002).

[37] I. A. Merkulov, A. L. Efros and M. Rosen, *Electron spin relaxation by nuclei in semiconductor quantum dots,* Phys. Rev. *B,* **65** 205309 (2002).

[38] A. Imamoglu, E. Knill, L. Tian and P. Zoller, *Optical Pumping of Quantum-Dot Nuclear Spins,* Phys. Rev. Lett., **91** 017402 (2003).

[39] A. Greilich, A. Shabaev, D. R. Yakovlev, A. L. Efros, I. A. Yugova, D. Reuter, A. D. Wieck and M. Bayer, *Nuclei-Induced Frequency Focusing of Electron Spin Coherence,* Science, **317** 1896 (2007).

[40] P. Maletinsky, A. Badolato and A. Imamoglu, *Dynamics of Quantum Dot Nuclear Spin Polarization Controlled by a Single Electron,* Phys. Rev. Lett., **99** 056804 (2007).

[41] G. Binasch, P. Grünberg, F. Saurenbach and W. Zinn, *Enhanced magnetoresistance in layered magnetic structures with antiferromagnetic interlayer exchange,* Phys. Rev. B*,* **39** 4828-4803 (1989).

[42] M. N. Baibich, J. M. Broto, A. Fert, F. Nguyen Van Dau and F. Petroff, *Giant Magnetoresistance of (001)Fe/(001)Cr Magnetic Superlattices,* Phys. Rev. Lett*.,* **61** 2472-2475 (1988).

[43] S. A. Wolf, D. D. Awschalom, R. A. Buhrman, J. M. Daughton, S. von Molnar, M. L. Roukes, A. Y. Chtchelkanova and D. M. Treger, *Spintronics: A Spin-Based Electronics Vision for the Future*, Science, pp. 1488-1495, **294** 5546 (2001).

[44] G. A. Prinz, *Magnetoelectronics, Science,* pp. 1660-1663, **282** 5394 (1998).

[45] "www.ibm.com," [Online]. Available: http://www-03.ibm.com/ibm/history/ibm100/us/en/icons/spintronics/.

[46] "www.everspin.com," Everspin Technologies, Inc., [Online]. Available: http://www.everspin.com/.

[47] S. S. P. Parkin, X. Jiang, C. Kaiser, A. Panchula, K. Roche and M. Samant, *Magnetically Engineered Spintronic Sensors and Memory*, IEEE Xplore, **91** 661 (2003).

[48] M. K. Ho, C. H. Tsang, R. E. Fontana and S. S. Parkin, *Study of magnetic tunnel junction read sensors,* IEEE Trans. Magn*.,* **37** 1691 (2001).

[49] M. Löhndorf, T. Duenas, M. Tewes, E. Quandt, M. Rühring and J. Wecker, *Highly sensitive strain sensors based on magnetic tunneling junctions,* Appl. Phys. Lett*.,* **81** 313 (2002).

[50] S. Manipatruni, D. E. Nikonov and I. A. Young, *Modeling and Design of Spintronic Integrated Circuits*, IEEE Xplore*,* **59** 2801 (2012).

[51] S. Ikeda, J. Hayakawa, Y. Ashizawa, Y. M. Lee, K. Miura, H. Hasegawa, M. Tsunoda, F. Matsukura and H. Ohno, *Tunnel magnetoresistance of 604% at 300K by suppression of Ta diffusion in CoFeB/MgO/CoFeB pseudo-spin-valves annealed at high temperature,* Appl. Phys. Lett*.,* **93** 082508 (2008).

[52] L. Zhuang, L. Guo and Y. S. Chou, *Silicon single-electron quantum-dot transistor switch operating at room temperature*, Appl. Phys. Lett*.,* **72** 1205 (1998).

[53] K. Konishi, T. Nozaki, H. Kubota, A. Fukushima, S. Yuasa, M. Shiraishi and Y. Suzuki, *Current-Field Driven "Spin Transistor*", Appl. Phys. Express, **2** 063004 (2009).

[54] "www.toshiba.co.jp," Toshiba, (2009). [Online]. Available: http://www.toshiba.co.jp/about/press/2009_12/pr0801.htm.

[55] D. R. Vij, *Handbook of Applied Solid State Spectroscopy*, Berlin: Springer, (2010).

[56] I. Oliveira, R. J. Sarthour, T. Bonagamba, E. Azevedo and J. C. Freitas, *NMR Quantum Information*, Elsevier S&T, (2011).

[57] R. S. Macomber, *A Complete Introduction to Modern NMR Spectroscopy*, New York: John Wiley and Sons, (1997).

[58] J. M. Blatt and V. F. Weisskopf, *Theoretical Nuclear Physics*, Dover Pubn Inc, (1991).

[59] W. Voigt, *Lehrbuch der Kristallphysik*, Teubner, (1910).

[60] R. K. Sundfors, *Experimental gradient-elastic tensor and chemical bonding in III-V semiconductors*, Phys. Rev. B, **10** 4244 (1974).

[61] R. G. Shulman, B. J. Wyluda and P. W. Anderson, *Nuclear Magnetic Resonance in Semiconductors. II. Quadrupole Broadening of Nuclear Magnetic Resonance Lines by Elastic Axial Deformation*, Phys. Rev., **107** 953-958 (1957).

[62] S. Saeidian, I. Lesanowsky and P. Schmelcher, *Atomic hyperfine resonances in a magnetic quadrupole field*, Phys. Rev. A*,* **76** 023424 (2007).

[63] E. A. Chekhovich, A. B. Krysa, M. S. Skolnick and A. I. Tartakovskii, *Direct Measurement of the Hole-Nuclear Spin Interaction in Single InP/GaInP Quantum Dots Using Photoluminescence Spectroscopy*, Phys. Rev. Lett*.,* **106** 027402 (2011).

[64] W. Kutzelnigg, *Origin and meaning of the Fermi contact interaction*, Theoretica chimica acta*,* **73** 173-200 (1988).

[65] U. Fasol and E. Dormann, *Overhauser shift of the electron spin resonance line of Si:P at the metal-insulator transition: 31P contribution*, Phys. Rev. B*,* **66** 075207 (2002).

[66] A. W. Overhauser, *Polarization of Nuclei in Metals,* Phys. Rev*.,* **92** 411-415 (1953).

[67] D. Gammon, S. W. Brown, E. S. Snow, T. A. Kennedy, D. S. Katzer and D. Park, *Nuclear Spectroscopy in Single Quantum Dots: Nanoscopic Raman Scattering and Nuclear Magnetic Resonance*, Science, **277** 85 (1997).

[68] A. S. Bracker, E. A. Stinaff, D. Gammon, M. E. Ware, J. G. Tischler, A. Shabaev, A. L. Efros, D. Park, D. Gershoni, V. L. Korenev and I. A. Merkulov, *Optical Pumping of the Electronic and Nuclear Spin of Single Charge-Tunable Quantum Dots*, Phys. Rev. Lett*.,*

94 047402 (2005).

[69] B. Eble, O. Krebs, A. Lemaître, K. Kowalik, A. Kudelski, P. Voisin, B. Urbaszek, X. Marie and T. Amand, *Dynamic nuclear polarization of a single charge-tunable InAs/GaAs quantum dot*, *Phys. Rev. B,* **74** 081306 (2006).

[70] C. W. Lai, P. Maletinsky, A. Badolato and A. Imamoglu, *Knight-Field-Enabled Nuclear Spin Polarization in Single Quantum Dots*, *Phys. Rev. Lett.,* **96** 167403 (2006).

[71] A. I. Tartakovskii, T. Wright, A. Russell, V. I. Fal'ko, A. B. Van'kov, J. Skiba-Szymanska, I. Drouzas, R. S. Kolodka, R. S. Kolodka, M. S. Skolnick, P. W. Fry, A. Tahraoui, H. Y. Liu and M. Hopkinson, *Nuclear Spin Switch in Semiconductor Quantum Dots*, *Phys. Rev. Lett.,* **98** 026806 (2007).

[72] M. N. Makhonin, E. A. Chekhovich, P. Senellart, A. Lemaître, M. S. Skolnick and A. I. Tartakovskii, *Optically tunable nuclear magnetic resonance in a single quantum dot*, *Phys. Rev. B,* **82** 161309 (2010).

[73] J. Fischer, B. Trauzettel and D. Loss, *Hyperfine interaction and electron-spin decoherence in graphene and carbon nanotube quantum dots*, *Phys. Rev. B,* **80** 155401 (2009).

[74] V. L. Korenev, *Nuclear Spin Nanomagnet in an Optically Excited Quantum Dot*, *Phys. Rev. Lett.,* **99** 256405 (2007).

[75] G. Burkhard, D. Loss and D. P. DiVincenzo, *Coupled quantum dots as quantum gates*, Phys. Rev. B*,* **59** 2070-2078 (1999).

[76] A. Tartakovskii, *Quantum Dots Optics, Electron Transport and Future Applications*, Cambridge University Press, (2012).

[77] M. I. Dyakonov, *Spin Physics in Semiconductors*, Berlin: Springer Verlag, (2008).

[78] M. Y. Petrov, I. V. Ignatiev, S. V. Poltavtsev, A. Greilich, A. Bauschulte, D. R. Yakovlev and M. Bayer, *Effect of thermal annealing on the hyperfine interaction in InAs/GaAs quantum dots*, Phys. Rev. *B,* **78** 045315 (2008).

[79] U. Woggon, K. Hild, F. Gindele and W. Langbein, *Huge binding energy of localized biexcitons in CdS/ZnS quantum structures*, Phys. Rev. *B,* **61** 12632-12635 (2000).

[80] A. Abragam and W. G. Proctor, *Spin Temperature*, Phys. Rev.*,* **109** 1441-1458 (1958).

[81] M. Goldman, *Overview of Spin Temperature, Thermal Mixing and Dynamic Nuclear Polarization*, Applied Magnetic Resonance*,* **34** 219-226 (2008).

[82] A. Abragam, *The Principles of Nuclear Magnetism*, Oxford: Clarendon Press, (1961).

[83] P. Michler, *Single Semiconductor Quantum Dots*, Berlin: Springer-Verlag, (2009).

[84] P. Paget, G. Lampel and B. Sapoval, *Low field electron-nuclear spin coupling in gallium arsenide under optical pumping conditions*, Phys. Rev. B, **15** 5780-5796 (1977).

[85] R. I. Dzhioev and V. L. Korenev, *Stabilization of the Electron-Nuclear Spin Orientation in Quantum Dots by the Nuclear Quadrupole Interaction*, Phys. Rev. Lett*.,* **99** 037401 (2007).

[86] C. P. Slichter, *Principles of Magnetic Resonance*, Berlin: Springer-Verlag, (1990).

[87] D. M. Grant and R. K. Harris, *Encyclopedia of Nuclear Magnetic Resonance Vol. 6*, Chichester, England: Wiley & Sons, (1996).

[88] V. K. Kalevich, V. D. Kulkov and V. G. Fleischer, Izv. Akad. Nauk SSSR Ser. Fiz. *,* **46** 492 (1982).

[89] D. Paget, *Optical detection of NMR in high-purity GaAs: Direct study of the relaxation of nuclei close to shallow donors*, Phys. Rev. B*,* **25** 4444-4451 (1982).

[90] N. T. Bagraev and L. S. Vlasenko, Z. Eksp. Teor. Fiz*.,* **83** 2186 (1982).

[91] V. K. Kalevich, V. D. Kulkov and V. G. Fleischer, Z. Eksp. Fiz*.,* **35** 17 (1982).

[92] M. Sugawara, R. Willardson and E. Weber, *Self-Assembled InGaAs/GaAs Quantum Dots*, San Diego: Academic Press, (1999).

[93] I. H. Lee, V. Rao, M. R. Martin and J. P. Leburton, *Shell filling of artificial atoms within density-functional theory*, Phys. Rev. B*,* **57** 9035-9042 (1998).

[94] G. A. Narvaez and P. Hawrylak, *Effects of electron-electron interactions on excitonic absorption in charged self-assembled quantum dots*, Phys. Rev. B*,* **61** 13753-13762 (2000).

[95] S. Bednarek, B. Szafran and J. Adamowski, *Theoretical description of electronic properties of vertical gated quantum dots*, Phys. Rev. B*,* **64** 195303 (2001).

[96] S. Tarucha, D. G. Austing, T. Honda, R. J. Van der Hage and L. P. Kouwenhoven, *Shell Filling and Spin Effects in a Few Electron Quantum Dot*, Phys. Rev. Lett*.,* **77** 3613-3616 (1996).

[97] M. A. Kastner, *Artificial Atoms*, Physics Today*,* **46**(1) 24 (1993).

[98] T. Chakraborty, *Quantum Dots: A Survey of the Properties of Artificial Atoms*, Elsevier Science, (1999).

[99] F. Cavaliere, U. De Giovannini, R. Cenni, M. Sassetti and B. Kramer, *Magnetic field dependence of quantum dot ground states*, *Physica E: Low-dimensional Systems and* Nanostructures*,* 40 1427-1429 (2008).

[100] S. A. McCarthy, J. B. Wang and P. C. Abbott, *Electronic structure calculation for N-electron quantum dots*, Computer Physics Communications, **141** 175-204 (2001).

[101] L. R. C. Fonseca, J. L. Jimenez, J. P. Leburton and R. M. Martin, *Self-consistent calculation of the electronic structure and electron-electron interaction in self-assembled InAs-GaAs quantum dot structures*, Phys. Rev. B*,* **57** 4017 (1998).

[102] M. Fricke, A. Lorke, J. P. Kotthaus, G. Medeiros and P. M. Petroff, *Shell structure and electron-electron interaction in self-assembled InAs quantum dots*, Europhysics Letters*,* **36** 197 (1996).

[103] J. Shumway, L. R. C. Fonseca, J. P. Leburton, R. M. Martin and D. M. Ceperley, *Electronic structure of self-assembled quantum dots: comparison between density functional theory and diffusion quantum Monte Carlo*, *Physica E: Low-dimensional* Systems and Nanostructures*,* **8** 260-268 (2000).

[104] Bo-yong Jia, Zhong-yuan Yu, Yu-min Liu, Hong-da Tian, *Calculation of valence band structures of InAs/GaAs quantum ring and quantum dot: using numerical Fourier transform method,* The Journal of China Universities of Posts and Telecommunications*,* **17** 106-110 (2010).

[105] D. G. Austing, S. Sasaki, S. Tarucha, S. M. Reimann, M. Koskinen and M. Manninen, *Ellipsoidal deformation of vertical quantum dots*, Phys. Rev. B, **60** 11514-11523 (1999).

[106] M. Bayer, G. Ortner, O. Stern, A. Kuther, A. A. Gorbunov, A. Forchel, P. Hawrylak, S. Fafrad, K. Hinzer, T. L. Reinecke, S. N. Walck, J. P. Reithmaier, F. Klopf and F. Schäfer, *Fine structure of neutral and charged excitons in self-assembled In(Ga)As/(Al)GaAs quantum dots*, Phys. Rev. B *,* **65** 195315 (2002).

[107] I. A. Akimov, A. Hundt, T. Flissikowski and F. Henneberger, *Fine structure of the trion triplet state in a single self-assembled semiconductor quantum dot*, Appl. Phys. Lett*.,* **81** 4730 (2002).

[108] I. A. Akimov, K. V. Kavokin, A. Hundt and F. Henneberger, *Electron-hole exchange interaction in a negatively charged quantum dot*, Phys. Rev. B*,* **71** 075326 (2005).

[109] S. Cortez, O. Krebs, S. Laurent, M. Senes, X. Marie, P. Voisin, R. Ferreira, G. Bastard, J.-

M. Gérard and T. Amand, *Optically Driven Spin Memory in n-Doped InAs-GaAs Quantum Dots*, Phys. Rev. Lett., **89** 207401 (2002).

[110] S. Laurent, M. Senes, O. Krebs, V. K. Kalevich, B. Urbaszek, X. Marie, T. Amand and P. Voisin, *Negative circular polarization as a general property of n-doped self-assembled InAs/GaAs quantum dots under nonresonant optical excitation*, Phys. Rev. B, **73** 235302 (2006).

[111] D. Press, T. D. Ladd, B. Zhang and Y. Yamamoto, *Complete quantum control of a single quantum dot spin using ultrafast optical pulses*, Nature, **456** 218-221 (2008).

[112] A. N. Vamivakas, C. Y. Lu, C. Matthiesen, S. Fält, A. Badolato and M. Atatüre, *Observation of spin-dependent quantum jumps via quantum dot resonance fluorescence*, Nature, **467** 297-300 (2010).

[113] S. T. Yilmaz, P. Fallahi and A. Imamoğlu, *Quantum-Dot-Spin Single-Photon Interface*, Phys. Rev. Lett., **105** 033601 (2010).

[114] X. Xu, B. Sun, P. R. Berman, D. G. Steel, A. S. Bracker, D. Gammon and L. J. Sham, *Coherent population trapping of an electron spin in a single negatively charged quantum dot*, Nature Physics, **4** 692-695 (2008).

[115] M. Syperek, D. R. Yakovlev, I. A. Yugova, J. Misiewicz, I. V. Sedova, S. V. Sorokin, A. A. Toropov, S. V. Ivanov and M. Bayer, *Long-lived electron spin coherence in CdSe/Zn(S,Se) self-assembled quantum dots*, Phys. Rev. B, **84** 085304 (2011).

[116] A. Shabaev, E. A. Stinaff, A. S. Bracker, D. Gammon, A. L. Efros, V. L. Korenev and I. Merkulov, *Optical pumping and negative luminescence polarization in charged GaAs quantum dots*, Phys. Rev. B, **79** 035322 (2009).

[117] K. Gündoğdu, K. C. Hall, E. J. Koerperick, C. E. Pryor, M. E. Flatté, T. F. Boggess, O. B. Shchekin and D. G. Deppe, *Electron and hole spin dynamics in semiconductor quantum dots*, Appl. Phys. Lett., **86** 113111 (2005).

[118] R. I. Dzhioev, B. P. Zakharchenya, V. L. Korenev, P. E. Pak, D. A. Vinokurov, O. V. Kovalenkov and I. S. Tarasov, Fiz. Tverd. Tela (St. Petersburg), **40** 1745 (1998).

[119] M. E. Ware, E. A. Stinaff, D. Gammon, M. F. Doty, A. S. Bracker, D. Gershoni, V. L. Korenev, Ş. C. Bădescu, Y. Lyanda-Geller and T. L. Reinecke, *Polarized Fine Structure in the Photoluminescence Excitation Spectrum of a Negatively Charged Quantum Dot*, Phys. Rev. Lett., **95** 177403 (2005).

[120] I. V. Ignatiev, S. Y. Verbin, I. Y. Gerlovin, R. V. Cherbunin and Y. Masumoto, *Negative circular polarization of InP QD luminescence: Mechanism of formation and main*

regularities, Opticas and Spectroscopy, **106** 375-387 (2009).

[121] T. Auer, *The electron-nuclear spin system in (In,Ga)As quantum dots*, Göttingen: Sierke Verlag, (2008).

[122] W. Hanle, *Über Magnetische Beeinflussung der Polarisation der Resonanzfluoreszenz*, Z. Phys., 30 93-105 (1924).

[123] F. Maier and B. P. Zakharchenya, *Optical Orientation*, Amsterdam: North-Holland, 1989.

[124] A. K. Nowak, E. Gallardo, H. P. Van der Meulen, J. M. Calleja, J. M. Ripalda, L. González and Y. González, *Band-gap renormalization in InP/GaxIn1−xP quantum dots*, Phys. Rev. B, **83** 245447 (2011).

[125] Y. Ogawa, T. Toizumi, F. Minami and A. V. Baranov, *Nanometer-scale mapping of the strain and Ge content of Ge/Si quantum dots using enhanced Raman scattering by the tip of an atomic force microscope*, Phys Rev. B, **83** 081302(R) (2011).

[126] S. I. Rybchenko, R. Gupta, K. T. Lai, I. E. Itskevich, S. K. Haywood, V. Tasco, N. Deguffroy, A. N. Baranov and E. Tournié, *Conduction-band crossover induced by misfit strain in InSb/GaSb self-assembled quantum dots*, Phys. Rev. B, **76** 193309 (2007).

[127] T. Nowozin, A. Marent, L. Bonato, A. Schliwa, D. Bimberg, E. P. Smakman, J. K. Garleff, P. M. Koenraad, R. J. Young and M. Hayne, *Linking structural and electronic properties of high-purity self-assembled GaSb/GaAs quantum dots*, Phys. Rev. B, **86** 035305 (2012).

[128] R. Kaji, S. Adachi, T. Shindo and S. Muto, *Quasiresonant exciton spin orientation and alignment in a single quantum dot under zero and nonzero magnetic fields*, Phys. Rev. B, **80** 235334 (2009).

[129] Y. G. Kusrayev, B. R. Namozov, I. V. Sedova and S. V. Ivanov, *Optically induced spin polarization and g-factor anisotropy of holes in CdSe/ZnSe quantum dots*, Phys. Rev. B, **76** 153307 (2007).

[130] A. Zangwill, Epitaxy : *Physics at Surfaces*, New York: Cambridge University Press, (1988).

[131] H. Sitter and M. A. Herman, *Molecular Beam Epitaxy*, Berlin: Springer-Verlag, (1989).

[132] A. Pimpinelli and J. Villain, *Physics of Crystal Growth*, Cambridge University Press, (1998).

[133] D. Bimberg, M. Grundmann and N. N. Ledentsov, *Quantum Dot Heterostructures*, New York: Wiley & Sons, (1998).

[134] A. Zrenner, L. V. Butov, M. Hagn, G. Abstreiter, G. Böhm and G. Weimann, *Quantum dots formed by interface fluctuations in AlAs/GaAs coupled quantum well structures*, Phys. Rev. Lett., **72** 3382-3385 (1994).

[135] I. Stranski and L. Krastanow, *Abhandlungen der Mathematisch-Naturwissenschaftlichen Klasse IIb*, Akademie der Wissenschaften Wien, **146** 797-810 (1938).

[136] J. Tersoff and F. K. LeGoues, *Competing relaxation mechanisms in strained layers*, Phys. Rev. Lett., **72** 3570-3573 (1994).

[137] H. Marcia and G. H. Gilmer, *Thin film growth mods, wetting and cluster nucleation*, Surface Science, **194** 333-346 (1988).

[138] O. Schilling, A. Forchel and M. Lebedev, *Deep etched InGaAs/InP quantum dots with strong lateral confinement effects*, Superlattice and Microstructures, **16** 261-264 (1994).

[139] T. Someya, H. Akiyama and H. Sakaki, *Laterally Squeezed Excitonic Wave Function in Quantum Wires*, Phys. Rev. Lett, **74** 3664-3667 (1995).

[140] J. G. Belk, J. L. Sudijono, X. M. Zhang, J. H. Neave, T. S. Jones and B. A. Joyce, *Surface Contrast in Two Dimensionally Nucleated Misfit Dislocations in InAs /GaAs(110) Heteroepitaxy*, Phys. Rev. Lett., **78** 475-478 (1997).

[141] B. A. Joyce, T. S. Jones and J. G. Belk, *Reflection high-energy electron diffraction/scanning tunneling microscopy study of InAs growth on the three low index orientations of GaAs: Two-dimensional versus three-dimensional growth and strain relaxation*, Journal of Vacuum Science & Technology *B,* **16** 2373-2380 (1998).

[142] T. Someya, H. Akiyama and H. Sakaki, *Shape analysis of wave functions in T-shaped quantum wires by means of magneto-photoluminescence spectroscopy*, Solid State Communications, **108** 923-927 (1998).

[143] W. Wegscheider, G. Schedelbeck, G. Abstreiter, M. Rother and M. Bichler, *Atomically Precise GaAs/AlGaAs Quantum Dots Fabricated by Twofold Cleaved Edge Overgrowth*, Phys. Rev. Lett, **79** 1917-1920 (1997).

[144] G. Schedelbeck, W. Wegscheider, M. Bichler and G. Abstreiter, *Coupled Quantum Dots Fabricated by Cleaved Edge Overgrowth: From Artificial Atoms to Molecules*, Science, **278** 1792-1795 (1997).

[145] L. Goldstein, F. Glas, J. Y. Marzin, M. N. Charasse and G. Le Roux, *Growth by molecular beam epitaxy and characterization of InAs/GaAs strained-layer superlattices*, Appl. Phys. Lett., **47** 1099 (1985).

[146] O. Krebs, P. Maletinsky, T. Amand, B. Urbaszek, A. Lemaître, P. Voisin, X. Marie and A. Imamoglu, *Anomalous Hanle Effect due to Optically Created Transverse Overhauser Field in Single InAs/GaAs Quantum Dots*, Phys. Rev. Lett., **104** 056603 (2010).

[147] R. Cherbunin, S. Y. Verbin, T. Auer, D. R. Yakovlev, D. Reuter, A. D. Wieck, I. Y. Gerlovin, I. V. Ignatiev, D. V. Vishnevsky and M. Bayer, *Dynamics of the nuclear spin polarization by optically oriented electrons in a (In,Ga)As/GaAs quantum dot ensemble*, Phys. Rev. B, **80** 035326 (2009).

[148] M. Y. Petrov, G. G. Kozlov, I. V. Ignatiev, R. V. Cherbunin, D. R. Yakovlev and M. Bayer, *Coupled electron-nuclear spin dynamics in quantum dots: A graded box model approach*, Phys. Rev. B, **80** 125318 (2009).

[149] R. V. Cherbunin, S. Y. Verbin, K. Flisinski, I. Y. Gerlovin, I. V. Ignatiev, D. V. Vishnevsky, D. Reuter, A. D. Wieck, D. R. Yakovlev and M. Bayer, *Time-resolved Hanle effect in (In,Ga)As/GaAs quantum dots*, J. Phys.: Conf. Ser., **245** 012055 (2010).

[150] M. I. Dyakonov, *Spin Physics in Semiconductors*, Berlin, Springer-Verlag, (2008), pp. Chap.11, p.309.

[151] X.-F. Shi, *Nuclear spin polarization in a single quantum dot pumped by two laser beams*, Phys. Rev. B, **87** 195318 (2013).

[152] E. S. Artemova and I. A. Merkulov, Sov. Phys. Solid State, **27** 694 (1985).

[153] K. Flisinski, I. Y. Gerlovin, I. V. Ignatiev, M. Y. Petrov, S. Y. Verbin, D. R. Yakovlev, D. Reuter, A. D. Wieck and M. Bayer, *Optically detected magnetic resonance at the quadrupole-split nuclear states in (In,Ga)As/GaAs quantum dots*, Phys. Rev. B, **82** 081308(R) (2010).

[154] M. I. Dyakonov and V. I. Perel, Sov. Phys. JETP, **41** 759 (1975).

[155] M. S. Kuznetsova, K. Flisinski, I. Ya. Gerlovin, I. V. Ignatiev, K. V. Kavokin, S. Yu. Verbin, D. R. Yakovlev, D. Reuter, A. D. Wieck, and M. Bayer, *Hanle effect in (In,Ga)As quantum dots: Role of nuclear spin fluctuations,* Phys. Rev. B **87**, 235320 (2013).

[156] N. Bloembergen, E. M. Purcell and R. M. Pound, Relaxation Effects in Nuclear Magnetic Resonance Absorption, Phys. Rev., **73** 679-712 (1948).

[157] A. G. Redfield, *Nuclear Magnetic Resonance Saturation and Rotary Saturation in Solids*,

Phys. Rev., **98** 1787-1809 (1955).

[158] C. P. Slichter and W. C. Holton, *Adiabatic Demagnetization in a Rotating Reference System*, Phys. Rev., **122** 1701-1708 (1961).

[159] M. Goldman and A. Landesman, *Dynamic Polarization by Thermal Mixing between Two Spin Systems*, Phys. Rev., **132** 610-620 (1963).

[160] A. G. Redfield, *Nuclear Spin Thermodynamics in the Rotating Frame*, Science, **164** 1015-1023 (1969).

[161] A. Z. Genack and A. G. Redfield, *Theory of nuclear spin diffusion in a spatially varying magnetic field,* Phys. Rev. B, **12** 78-87 (1975).

[162] V. G. Fleisher, R. I. Dzhioev and B. P. Zakharchenya, *Optical cooling of a nuclear spin system of a conductor*, Pis'ma Zh. Eksp. Teor. Fiz., **23** 22-26 (1976).

[163] I. A. Merkulov and M. N. Tkachuk, *Resonant cooling of the spin system of a superconductor lattice nuclei,* Zh. Eksp. Teor. Fiz., **83** 620-627 (1982).

[164] R. Oulton, A. Greilich, S. Y. Verbin, R. V. Cherbunin, T. Auer, D. R. Yakovlev, M. Bayer, I. A. Merkulov, V. Stavarache, D. Reuter and A. D. Wieck, S*ubsecond Spin Relaxation Times in Quantum Dots at Zero Applied Magnetic Field Due to a Strong Electron-Nuclear Interaction*, Phys. Rev. Lett., **98** 107401 (2007).

[165] B. Pal and Y. Masumoto, *Spin relaxation in charge-tunable InP quantum dots*, Phys. Rev. B, **80** 125334 (2009).

[166] G. G. Kozlov, Zh. Eksp. Teor. Fiz. , **132** 918 (2007).

[167] R. V. Cherbunin, K. Flisinski, I. Y. Gerlovin, I. V. Ignatiev, M. S. Kuznetsova, M. Y. Petrov, D. R. Yakovlev, D. Reuter, A. D. Wieck and M. Bayer, *Resonant nuclear spin pumping in (In,Ga)As quantum dots*, Phys. Rev. B, **84** 041304(R) (2011).

[168] S. Y. Verbin, I. Y. Gerlovin, I. V. Ignatiev, M. S. Kuznetsova, R. V. Cherbunin, K. Flisinski, D. R. Yakovlev and M. Bayer, *Dynamics of nuclear polarization in InGaAs quantum dots in a transverse magnetic field,* JETP, **114** 681-690 (2012).

[169] V. K. Kalevich, V. D. Kulkov and V. G. Fleischer, Sov. Phys. Solid State, **22** 1208 (1980).

[170] G. Salis, D. T. Fuchs, J. M. Kikkawa, D. D. Awschalom, Y. Ohno and H. Ohno, *Optical Manipulation of Nuclear Spin by a Two-Dimensional Electron Gas*, Phys. Rev. Lett., **86** 2677-2680 (2001).

[171] M. Eickhoff, B. Lenzmann, G. Flinn and D. Suter, *Coupling mechanisms for optically induced NMR in GaAs quantum wells*, Phys. Rev. B*,* **65** 125301 (2002).

[172] J. Even, F. Doré, C. Cornet, L. Pedesseau, A. Schliwa and D. Bimberg, *Semianalytical evaluation of linear and nonlinear piezoelectric potentials for quantum nanostructures with axial symmetry*, Appl. Phys. Lett*.,* **91** 122112 (2007).

[173] V. Davydov, I. V. Ignatiev, I. E. Kozin, S. V. Nair, J. S. Lee, H. W. Ren, S. Sugou and Y. Masumoto, *Carrier Relaxation Dynamics in Self-Assembled Quantum Dots Studied by Artificial Control of Nonradiative Losses*, phys. stat. sol*.,* **224** 493-496 (2001).

[174] G. A. Narvaez, G. Bester and A. Zunger, *Carrier relaxation mechanisms in self-assembled (In,Ga)As/GaAs quantum dots: Efficient P→S Auger relaxation of electrons*, Phys. Rev. *B,* **74** 075403 (2007).

[175] K. Mukai, N. Ohtsuka, H. Shoji and M. Sugawara, *Phonon bottleneck in self-formed InxGa1−xAs/GaAs quantum dots by electroluminescence and time-resolved photoluminescence*, Phys. Rev. B*,* **54** 5243-5246 (1996).

[176] M. Yu. Petrov,1, G. G. Kozlov, I. V. Ignatiev, R. V. Cherbunin, D. R. Yakovlev and M. Bayer, *Coupled electron-nuclear spin dynamics in quantum dots: A graded box model approach*, Phys. Rev. B*,* **80**, 125318 (2009)

Appendix

The following figures shows Scanning Transmission Electron Microscopy (STEM) images of one sample of the series #11955 annealed at 820°C. At the end of this section is a picture of the self-made RF-coil, that was used to obtain the experimental results with the pulsed laser and $\mathrm{PM} + \mathrm{RF_y}$ and $\mathrm{PM} + \mathrm{RF_z}$modulation.

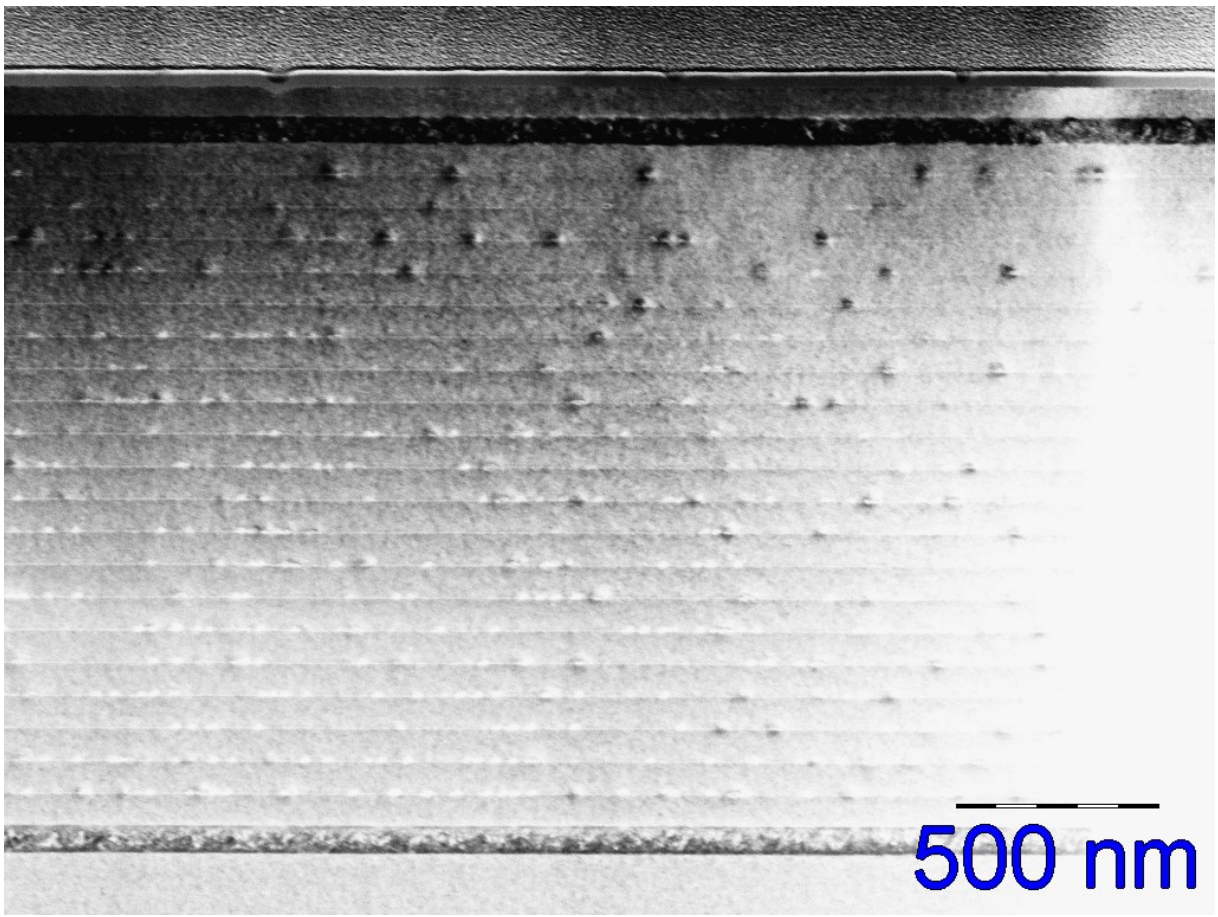

Figure 0-1 Side view of the sample obtained by using Scanning Transmission Electron Microscopy (STEM). A 100 nm thick piece of sample is prepared (2/3 of the sample is still usable). Aperture spot size is 20 nm and the pixel size is 2.9 nm. A larger part of unscattered beam is collected by the ring-type detector in order to reverse the contrast of the image.

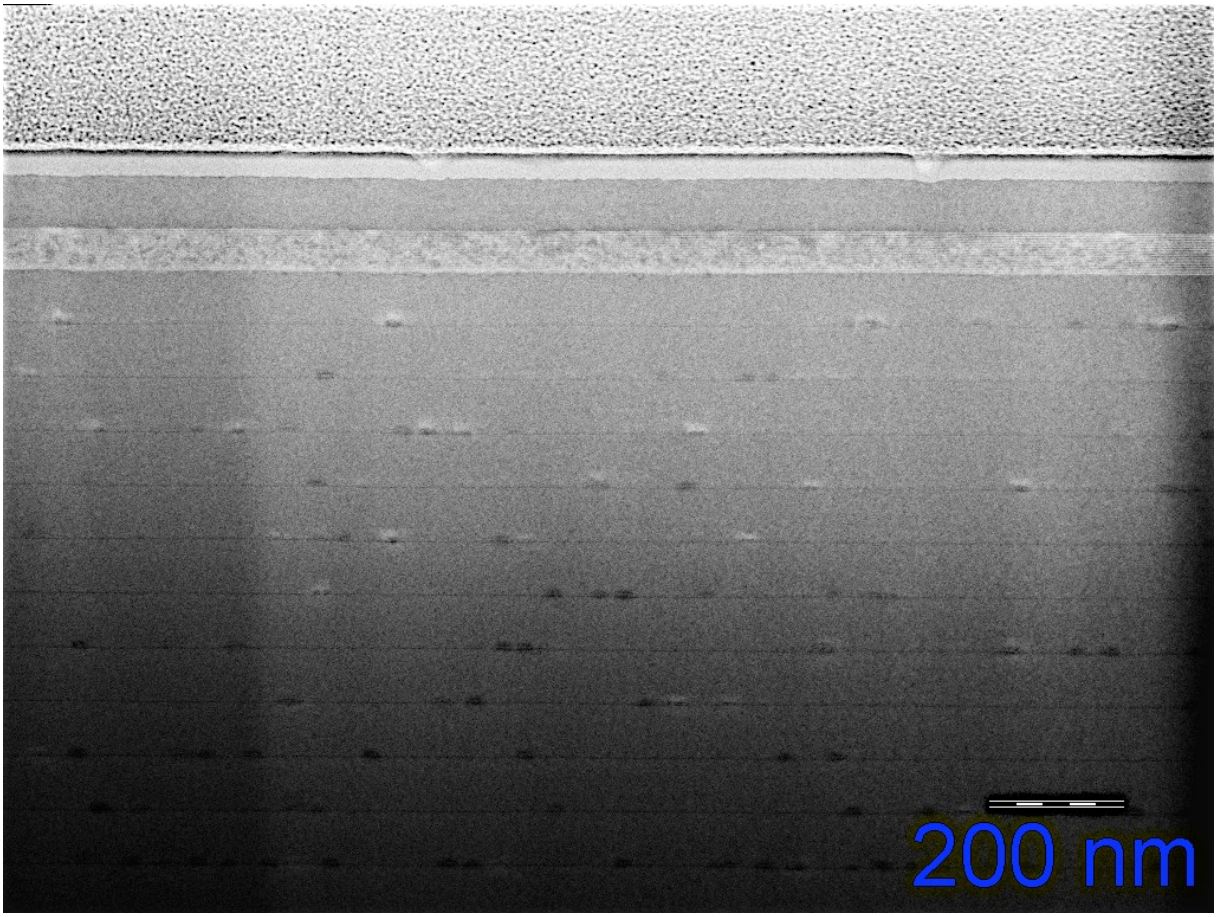

Figure 0-2 Side view of the sample obtained by using Scanning Transmission Electron Microscopy (STEM). A 100nm thick piece of sample is prepared (2/3 of the sample is still usable). Aperture spot size is 1.6nm and the pixel size is 1.7nm.

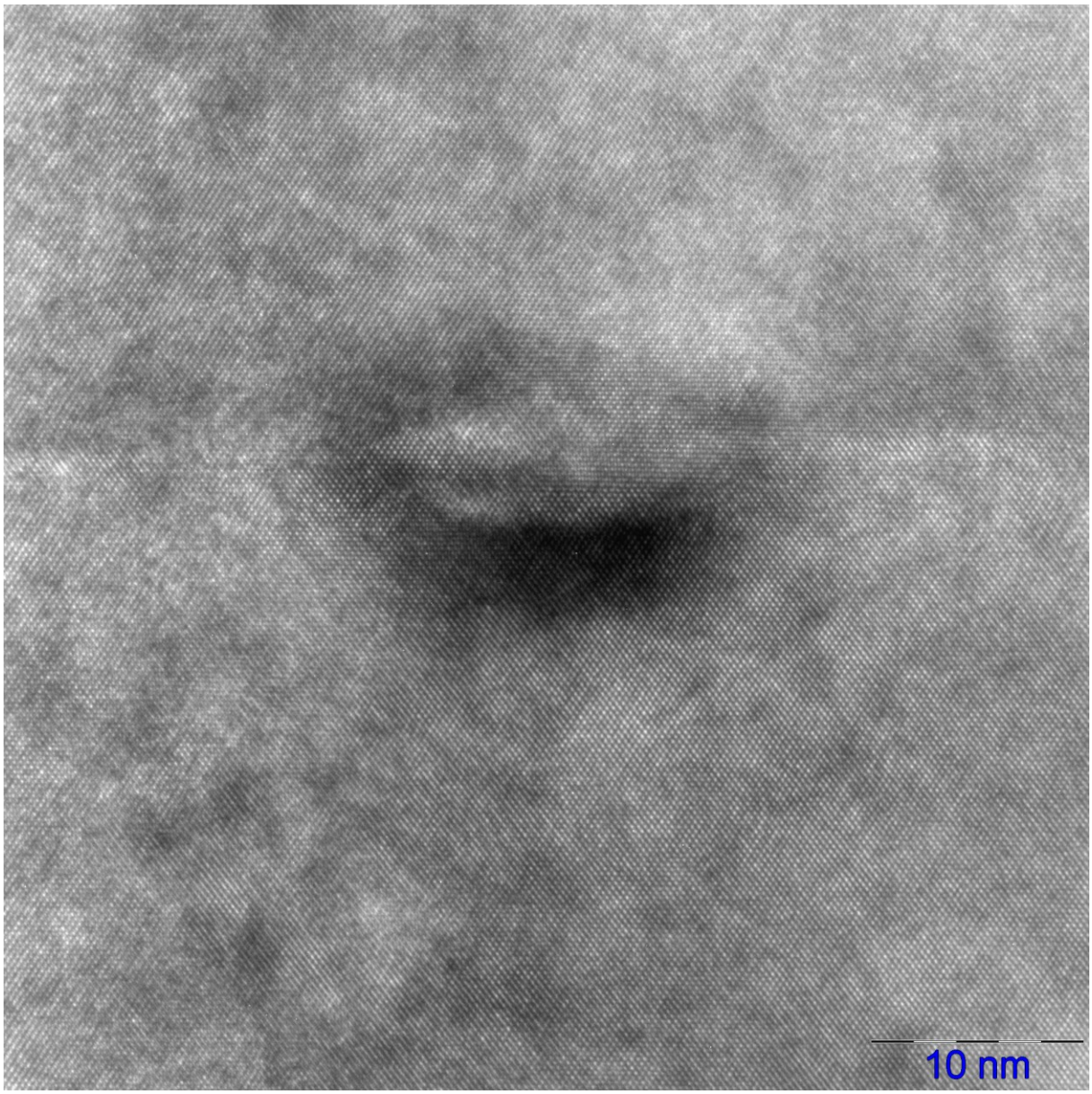

Figure 0-3 High-Resolution Transmission Electron Microscopy. Reflex [110]. In this reflex, the contrast mainly shows the distribution of the strain in the crystal lattice. In comparison to Figure 0-4 the strain is more symmetric. The growth direction is aligned to bottom. The darker area corresponds to larger strain.

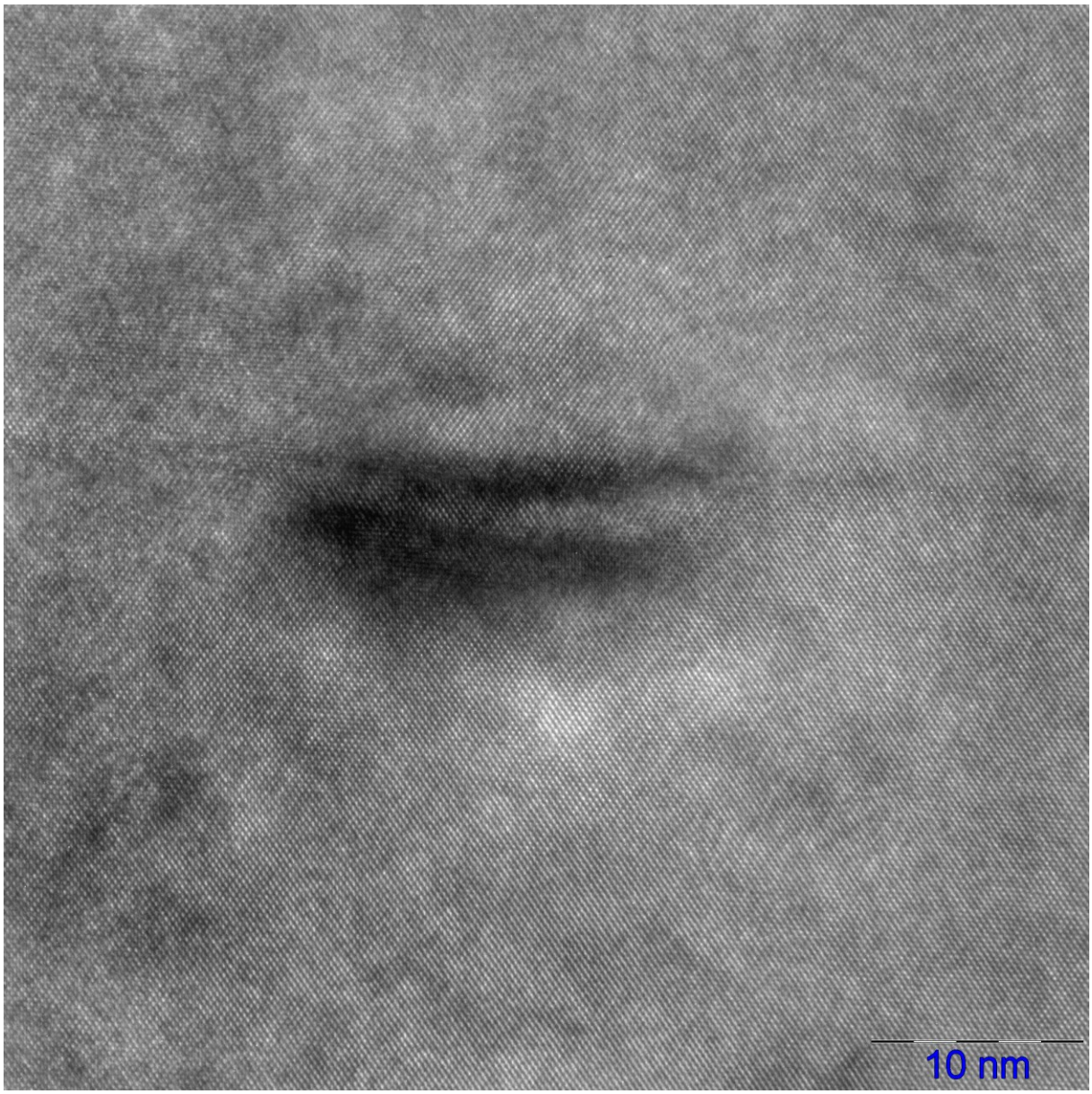

Figure 0-4 High-Resolution Transmission Electron Microscopy. Reflex [110]. In this reflex, the contrast mainly shows the distribution of the strain in the crystal lattice. In comparison to Figure 0-3 the strain is more tilted. The growth direction is aligned to bottom. The darker area corresponds to larger strain. Analysis of images of many QDs shows that typically the dots are symmetric (Figure 0-3) or strongly asymmetric (Figure 0-4).

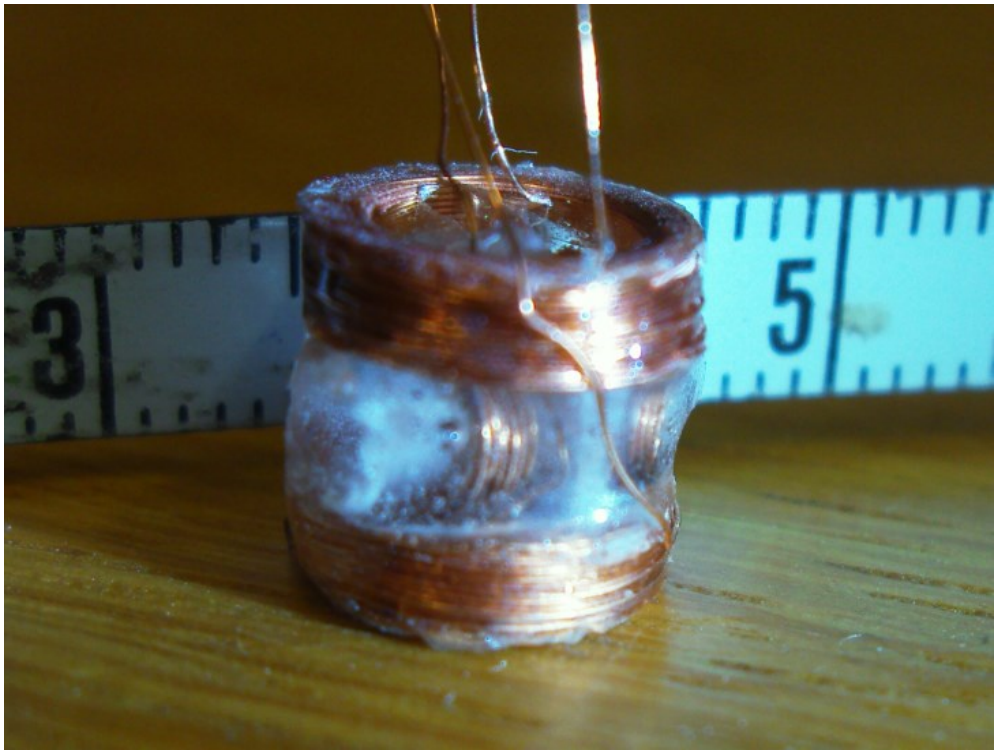

Figure 0-5 The RF-coils for z- and y-direction. The scale is given by the ruler in the background.

Publications

(1) M. S. Kuznetsova**, K. Flisinski**, I. Ya. Gerlovin, I. V. Ignatiev, K. V. Kavokin, S. Yu. Verbin, D. R. Yakovlev, D. Reuter, A. D. Wieck, and M. Bayer, *Hanle effect in (In,Ga)As quantum dots: Role of nuclear spin fluctuations,* Phys. Rev. B **87**, 235320 (2013).

(2) S. Y. Verbin, I. Y. Gerlovin, I. V. Ignatiev, M. S. Kuznetsova, R. V. Cherbunin**, K. Flisinski**, D. R. Yakovlev and M. Bayer, *Dynamics of nuclear polarization in InGaAs quantum dots in a transverse magnetic field*, JETP, **114** 681-690 (2012).

(3) R. V. Cherbunin, **K. Flisinski**, I. Ya. Gerlovin, I. V. Ignatiev, M. S. Kuznetsova, M. Yu. Petrov, D. R. Yakovlev, D. Reuter, A. D. Wieck, and M. Bayer, *Resonant nuclear spin pumping in (In,Ga)As quantum dots,* Phys. Rev. B **84**, 041304 (2011).

(4) S. Kuznetsova, **K. Flisinski**, I. Ya. Gerlovin, M. Yu. Petrov, I. V. Ignatiev, D. R. Yakovlev, D. Reuter, A. D. Wieck, and M. Bayer, *Nuclear magnetic resonances in (In,Ga)As/GaAs quantum dots studied by resonant optical pumping technique*, Phys. Rev. B **89**, 125304 (2014).

Abbreviations

α	Angle between $\boldsymbol{B}_{\mathrm{sum}}$ and the z-axis
[a.u.]	arbitrary units
A	mass number
A_{NCP}	amplitude of negative circular polarization photoluminescence
A_{HF}	hyperfine prefactor
A_{S}	hyperfine prefactor for S-type wave function particle
A_{P}	hyperfine prefactor for p-type wave function particle
β	reciprocal temperature of the nuclear spin system
$\boldsymbol{B}_{\mathrm{L}}$	local magnetic field due to neighboring nuclei
b_{N}	the effective field of totally polarized nuclei affecting the electron spin
$\boldsymbol{B}_{\mathrm{N}}$	Overhauser field
$\boldsymbol{B}_{\mathrm{NF}}$	nuclear fluctuation field
$\boldsymbol{B}_0$	constant external magnetic field (without specification in direction)
$B_{1/2}$	half width at half maximum of the Hanle curve
$\boldsymbol{B}_{\mathrm{e}}$	the Knight field
B_{x}	external magnetic field along x-axis
B_{y}	external magnetic field along y-axis
B_{z}	external magnetic field along z-axis
$B_{\mathrm{N,x}}$	x component of the nuclear field
$B_{\mathrm{N,z}}$	z component of the nuclear field
$\boldsymbol{B}_{\mathrm{N}}^{\mathrm{max}}$	maximum Overhauserfield
$\boldsymbol{B}_{\mathrm{tot}}^{\mathrm{N}}$	total magnetic field acting on the nuclear spin system
$\boldsymbol{B}_{\mathrm{tot}}^{\mathrm{e}}$	the total magnetic field acting on the electron
$\boldsymbol{B}_{\mathrm{sum}}$	sum of the Overhauser $\boldsymbol{B}_{\mathrm{N}}$, the nuclear fluctuation field $\boldsymbol{B}_{\mathrm{NF}}$ and the externally applied magnetic field $\boldsymbol{B}_{\mathrm{ext}}$

$B_{\mathrm{DNP}\perp}$	transverse component of nuclear polarization
$B_{\mathrm{DNP}\perp,\mathrm{L}}$	limit magnitude of the transverse component of nuclear polarization
$B_{\mathrm{NF}\parallel,\mathrm{L}}$	limit magnitude of the parallel component of nuclear fluctuation field
$\delta\boldsymbol{B}_{\mathrm{N}}$	frozen fluctuation field
$\Delta\alpha$	phase shift of $\mathrm{PM}+\mathrm{RF}_{\mathrm{y}}$ modulation and drops of A_{NCP}
Δ_{s-p}	hot trion energy splitting of ground-state and excited state
η	reciprocal temperature of the nuclear spin system
ϵ	strain tensor
e. g.	for example
E_m	distance in energy of the Zeeman levels
f_{PM}	polarization modulation frequency
γ_e	gyromagnetic ratio of the electron
γ_{N}	gyromagnetic ratio for nucleus N
γ_m	material energy
γ_s	substrate energy
γ_{ms}	material/substrate interface energy
$\mathrm{g_e}$	Landé-Faktor electron
g^*	Effective Landé-Faktor
$\hbar$	Planck constant
$\widehat{H}$	Hamiltonian of the sum of hyperfine, quadrupole and Zeeman interaction
$\widehat{H}_{\mathrm{HF}}$	Hamiltonian of the hyperfine interaction
$\widehat{H}_{\mathrm{Q}}$	Hamiltonian of the quadrupole interaction
$\widehat{H}_{\mathrm{Z}}$	Hamiltonian of the Zeeman interactio
$\hat{I}$	nuclear spin operator
$\hat{I}_{\mathrm{X}}$	x-component of the nuclear spin operator

$\hat{I}_{\mathrm{Y}}$	y-component of the nuclear spin operator
$\hat{I}_{\mathrm{Z}}$	z-component of the nuclear spin operator
k_{B}	Boltzmann constant
K_{S}	proportional coefficient
l	quantum number l
μ_{B}	Bohr magneton
m	quantum number m
M_0	thermal equilibrium magnetization
M_{Σ}	total spin of the recombining electron-hole pair
n	quantum number n
$\mathrm{n_p}$	# of quantum dots with parallel resident electron spin orientation to the photoexcited electron
$\mathrm{n_o}$	# of quantum dots with opposite resident electron spin orientation to the photoexcited electron
NCP	negative circular polarization
$N_{-1/2}$	population of nuclear spin -1/2 states
$N_{+1/2}$	population of nuclear spin -1/2 states
$\phi(\boldsymbol{r})$	electrostatic potential
ψ	normalized wave function of a stationary state of the nucleus
ω_N	frequency of nuclear spin precession induced by the applied field
ω_{L}	Larmor frequency
P_{exc}	excitation power
q	probability of hole spin relaxation
q_{ij}	electric field gradient tensor
Q	quadrupole moment
QD	quantum dot
Q_{ij}	quadrupole moment tensor

$\rho_{\mathrm{N}}(\boldsymbol{r})$	nuclear charge density distribution
$\mathbf{r}_{\mathrm{k}}$	co-ordinates of the protons
σ^{+}	right circular polarized light
σ^{-}	right circular polarized light
S_{11}	one element of the S tensor
$\boldsymbol{S}_e$	electron spin
$\boldsymbol{S}_h$	hole spin
$\boldsymbol{S}_0$	Initial electron spin orientation
$\boldsymbol{S}_{\mathrm{Z}}$	z-component of electron spin
$\langle \boldsymbol{S}_{\mathrm{Z}} \rangle$	time averaged z-component of electron spin
$\boldsymbol{S}_{\mathrm{z}}(t)$	time dependent z-component of electron spin
τ_{s}	spin relaxation time
τ_{r}	recombination lifetime
τ_{cee}	time of consecutive excitation events
$\lvert\tau_{\parallel}\rvert$	characteristic rise time for $\mathrm{B}_{\mathrm{DNP}\parallel}$
t_{s}	sweeping time of B_{x}
t_{exc}	excitation time
t_{d}	dark time
T	temperature
T_{e}	the electron spin lifetime
T^{-}	negative charged trion
T_1	spin-lattice relaxation time
T_2	transverse relaxation time
T_3^*	Effective transverse spin lifetime
T_{pre}	Duration of the Larmor precession
W	interaction energy of the nucleus
ζ	electron density on a nuclear site

Z	atomic number

Acknowledgments

First of all I would like to thank everybody who trusted in my skills and investigated his time in helping me to complete this thesis.

Especially I would like to thank Prof. Dr. Manfred Bayer and Prof. Dr. Dimitri R. Yakovlev for the opportunity to work in a very well equipped laboratory and to visit scientific conferences and schools. These conferences were an important platform to match the results of my research with other scientific groups.

Moreover I would like to thank Prof. Dr. Ivan V. Ignatiev and Prof. Dr. Sergey Yu. Verbin for the inspiring discussions. Their advices were always helpful for the development of my thesis.

Prof. Dr. Dietmar Fröhlich always made an effort for a tidy laboratory, which is a basis for laboratory work. His support in everyday problems of an experimentalist was very worthy.

The contact to Dr. Olivier Krebs led me to sharpen my ability for critical analysis and argumentation. It is always good to talk to someone who has a different opinion. I would like to thank him for the challenging discussions.

During one year of experimental work with Dr. Roman Cherbunin we developed new ideas and supported each other. Thank you for the fruitful cooperation.

Dr. Maria S. Kuznetsova helped me to survive long measurements. The cooperation was one of the finest divisions of labor that made efficient work possible.

Through the discussions with Dr. Mikhail Yu. Petrov I was able to gain deeper insight into the theoretical background of the nuclear spin topic. He was always open to discuss new ideas about the study we made. Besides I enjoyed our walks through St. Petersburg and the bike trip through Gelsenkirchen very much.

Dr. Jörn Krones always had an open ear for physical but also for non-physical topics at lunchtime. I wish you that in future you will still find some time to play the guitar and maybe we will have a jam session.

Only with the competent technical support of Klaus Wiegers a smooth progress of laboratory work was possible. Lars Wieschollek always helped me to solve technical problems fast. The discussions with him gave me an understanding of the characteristics and processing of different materials in order to construct devices.

Thanks to Michaela Wäscher for piloting me through all bureaucratic questions.

I would like to thank the Mechanical workshop who will always remember me as the “coil-man” for processing orders that were challenging for both sides.

Thanks to the electronic workshop for always giving competent advices. Even the development of new electronic devices was no problem.

Finally I would like to thank my parents who always believed in me and motivated me to deal with a problem even if it was unpleasant. Last but not least my thanks goes to my wife, who helped me to stay comprehensible in this thesis. The contact to her is earthing and vitalizing for me.

All in all I hope that this thesis can be the starting point of a stable environment for my family, where my son Samuel Libert (and all hopefully following children) can rise up in a peaceful way.